Sub-wavelength metrology using Coherent Fourier Scatterometry

Sub-wavelength metrology using Coherent Fourier Scatterometry

Proefschrift

ter verkrijging van de graad van doctor
aan de Technische Universiteit Delft,
op gezag van de Rector Magnificus prof. ir. K.C.A.M. Luyben,
voorzitter van het College voor Promoties,
in het openbaar te verdedigen op maandag 21 maart 2016 om 14:30 uur

door

Sarathi ROY

Master of Science in Applied Physics,
Technische Universiteit Delft, Delft, The Netherlands
geboren te Kolkata, India.

This dissertation has been approved by the

promotor: Prof. dr. H.P. Urbach
copromotor: Dr. S.F. Pereira

Composition of the doctoral committee:

Rector Magnificus,	voorzitter
Prof. dr. H.P. Urbach,	Technische Universiteit Delft, Netherlands
Dr. S.F. Pereira,	Technische Universiteit Delft, Netherlands

Independent members:

Prof. dr. M. Kujawinska,	Warsaw University of Technology, Poland
Prof. dr. W.M.J.M. Coene,	Technische Universiteit Delft
Dr. P. Petrik,	Hungarian Academy of Sciences, Hungary
Dr. A. Erdmann,	Fraunhofer IISB, Germany
Prof. dr. L.J. van Vliet ,	Technische Universiteit Delft, reserve member

This work was financially supported by the *Clean4Yield* project, funded through the European Union's Seventh Framework Program (FP7-NMP-2011) under Grant Agreement No. 281027.

Keywords: Scatterometry, Particle Detection, Critical Dimension Metrology

Printed by: Ipskamp Printing

Front & Back: Abstract representation of detection by asymmetry (Front) & Proposed multiple-head scatterometer (Back)

ISBN 978-94-6186-613-4
An electronic version of this dissertation is available at
http://repository.tudelft.nl/.

Curiouser and curiouser.

Lewis Carroll

Contents

Summary

Scattering is the process in which some form of radiation is deviated from its trajectory by a localized non-uniformity it encounters. These non-uniformities, called objects, can be of different material and geometry which determines among many things, mainly, the amount and direction of the scattered radiation. Scatterometry is the branch of science where an accurate estimation of certain properties of the object can be calculated upon measuring this scattered radiation and using some a-priori information about it. In this thesis we present results on designing, developing and testing a special type of optical scatterometric setup to perform metrology of two different kinds of objects: periodic ones (which, in theory, is infinitely extended) and very small isolated ones (which, in theory, can be considered as infinitesimally small). The obvious question that follows here is, how the same principle can work on two completely different types of objects?

To understand this, one should start from the basic principle of scatterometry. Although we have used a system which resembles very closely a standard optical microscope in its configuration, scatterometry is not a technique to enhance resolution limit like a normal microscope, but is rather a technique that utilizes the given set of a-priori information about the object and measurements of scattered radiation to reach a more accurate set of information. The special characteristics of a scatterometric system depends on the specific requirement at hand, for example, a fast system is optimized so that it utilizes the a-priori information given to it to minimize the convergence time, while having sufficient, but not the best, sensitivity. For a slow but accurate system, the main advantage is its low uncertainty. Irrespective of the ability to be configured for a specific task, it is the a-priori information in scatterometry that enables us to work on two objects belonging to the opposite ends of the geometric spectrum with almost identical optical configuration.

Before moving on into the details of the contents of the thesis, it is worthwhile to discuss in simple words the basic principle of Optical Fourier Scatterometry. Here, an object is shined by optical illumination and the scattered radiation in the far-field is detected. This signal is then compared with rigorous simulations to obtain information about the object which may include most basic case of just determining whether the object is present or not. For example, in the case of periodic objects intended to be used for critical dimension metrology, the goal is to retrieve the shape of the object as accurately as possible. On the other hand, for isolated objects, the primary aim is just to detect its presence or absence. The accuracy and the speed of convergence of a scatterometric system depends on the signal-to-noise ratio of this scattered radiation, and in this thesis we show a way to achieve an improved signal-to-noise ratio by using the coherence of the illuminating light and superposition of wave amplitudes in far-field.

In case of both types of objects, periodic or isolated, our desired accuracy remains in the sub-wavelength scale. More explicitly, for periodic objects, the shape parameters and their variations are all smaller than the wavelength of illuminating radiation, while, for isolated objects, the object itself is sub-wavelength.

We consider the problem with periodic object in the first three chapters of this thesis. In the first chapter we introduce the concept of optical Fourier scatterometry with coherent light, called the *coherent Fourier scatterometry*. In the next chapter we numerically prove the benefit of using coherent Fourier scatterometry compared to the state-of-the-art *incoherent Fourier scatterometry* by showing a sensitivity gain for all shape parameters, up to a factor of 8 for few of them, provided that sufficient scanning is done and the object period (pitch) is bigger than the illumination wavelength, while the shape parameters of the periodic object and their small variations are still sub-wavelength. This constraint about the grating pitch is shown to be removed in the third chapter with the introduction of a new version of *coherent Fourier scatterometry* by integrating it with interferometry, the *interferometric coherent Fourier scatterometry*. This technique, theoretically capable of taking the full benefit of coherence and thereby obtaining an improved sensitivity for a periodic object of any pitch, is shown to achieve a further improved sensitivity than coherent Fourier scatterometry by 2-5 times (thus almost an order more than incoherent Fourier scatterometry) for different parameters. Unfortunately, this improved sensitivity comes with the price of handling more data, and therefore, interferometric coherent Fourier scatterometry is more optimized for accuracy than speed. A faster version of interferometric coherent Fourier scatterometry, *sectioned interferometric coherent Fourier scatterometry*, is also introduced for application requiring fast convergence. Sectioned interferometric coherent Fourier scatterometry uses only a subset of the total data available in interferometric coherent Fourier scatterometry and can lead to sufficiently accurate results significantly faster than normal interferometric coherent Fourier scatterometry. We also add a short discussion about cross-correlation between shape parameters and how those can be minimized with 'zero-correlation-gratings'. This part of the thesis is entirely on theoretical and numerical analysis of the problem, without any experimental implementation.

From the fourth chapter we begin the discussion on the application of coherent Fourier scatterometry for detection of sub-wavelength isolated objects. The aim in this part of the thesis was to show that coherent Fourier scatterometry is also a valid alternative to the presently available particle detection systems on a substrate, with the additional advantages of low-power footprint and fast operation. To accomplish this, we needed to modify the coherent Fourier scatterometry system in several parts: the detection, the illumination and also the sample. The modifications done in the detection part of coherent Fourier scatterometry made it a system with differential detection. Then, the illuminating wave was modified to ensure optimum superposition between specular and scattered radiation in the far-field. Finally, the modification in the sample part was performed to obtain enhanced contrast. This series of improvements are described sequentially from chapter 4 to chapter 6. The results that we obtained from the implementation of a prototype coherent Fourier scatterometry setup in industrial environment and detecting particles on a mov-

ing polymer web is stated in chapter 7. The final chapter, chapter 8, contains a few outlooks, the possible extension of the technique and a conclusion to our long journey.

To end this summary, it is necessary to discuss shortly the possible impact of this work on the scientific community and in a broad sense, our society. Coherent Fourier scatterometry for periodic objects, essentially an one-dimensional grating, is aimed at the inverse problem of grating shape reconstruction. This problem is of interest in the field of quality control for lithography techniques because of its accuracy, non-invasiveness and fast convergence. We believe that the state-of-the-art incoherent systems, incoherent Fourier scatterometry, can be benefitted from the techniques described in this thesis for increasing their accuracy. This will lead to a better shape reconstruction under noisy environment. Coherent Fourier scatterometry for isolated objects is of primary interest for objects with a substrate which can be damaged by large exposure to energy, for example, polymer webs. However, the same principle can also be used to detect contamination on semiconductor substrates as well. This makes coherent Fourier scatterometry a detection system capable of working with various types of materials. Moreover, because of its simple detection technique, it can be implemented in situations where speed is of utmost importance, for example, to maintain a high throughput in a production line.

With these motivations, we hope the discussion on coherent Fourier scatterometry in the following chapter will be of interest to the reader and the scientific community, and also will be able to encourage further work for the benefit of society, by industrial implementation of the concepts and the scientific knowledge acquired from them.

Samenvatting

Verstrooiing is het proces waarbij enige vorm van straling van richting wordt veranderd door lokale afwijkingen van uniformiteit die deze tegenkomt. Deze niet-uniformiteiten, objecten genoemd, kunnen bestaan uit verschillende materialen en verschillende vormen hebben, hetgeen in hoofdzaak, naast vele andere dingen, bepalend is voor de hoeveelheid en de richting van de verstrooide straling. Scatterometrie is de tak van wetenschap waarbij bepaalde eigenschappen van het object nauwkeurig kunnen worden bepaald door deze verstrooide straling te meten en gebruik te maken van enige a-priori informatie over het object.

In dit proefschrift presenteren wij de resultaten van ontwerp, ontwikkeling en beproeving van een speciaal type optische scatterometry opstelling waarmee metingen kunnen worden verricht aan twee verschillende soorten objecten: periodieke (die zich in theorie oneindig ver uitstrekken) en zeer kleine geïsoleerde objecten (die in theorie als oneindig klein kunnen worden beschouwd). De voor de hand liggende vraag hier is hoe hetzelfde principe kan worden toegepast voor twee volledig verschillende types objecten?

Om dit te begrijpen moet worden uitgegaan van het basisprincipe van scatterometrie. Hoewel wij gebruik hebben gemaakt van een systeem waarvan de configuratie grote gelijkenissen vertoont met die van een standaard optische microscoop, is scatterometry geen techniek om het oplossend vermogen te verbeteren zoals bij een normale microscoop, maar is eerder een techniek die gebruik maakt van a-priori kennis in de vorm van de beschikbare dataset betreffende het object en van metingen van daaraan verstrooide straling, om te komen tot een nauwkeurigere set van gegevens waarmee het object kan worden beschreven. De speciale kenmerken van een scatterometry systeem zijn afhankelijk van de van toepassing zijnde specifieke eisen, bijvoorbeeld zal een snel systeem zodanig zijn geoptimaliseerd dat, gebruik makend van de a-priori informatie, de convergentietijd wordt geminimaliseerd, waarbij voldoende, maar niet de best mogelijke gevoeligheid wordt bereikt. Het belangrijkste voordeel voor een langzaam, maar nauwkeurig systeem, is de lage onzekerheid. Ongeacht de geschiktheid van een systeem om te worden ingericht voor een speciale taak is het de a-priori kennis bij scatterometrie die ons in staat stelt te werken met proefstukken aan de uitersten van het geometrische spectrum, en daarbij gebruik te maken van vrijwel dezelfde optische configuratie.

Voordat wordt ingegaan op de details van de inhoud van dit proefschrift, is het de moeite waard in eenvoudige bewoordingen de basisbeginselen van Optische Fourier Scatterometry te behandelen. In de praktijk wordt een object beschenen door optische verlichting en wordt de verstrooide straling in het verre veld gedecteerd. Het signaal wordt vergeleken met rigoureuze simulaties waarmee informatie omtrent het object wordt verkregen, in het uiterste geval slechts de vaststelling of het object al dan niet aanwezig is. In het geval bijvoorbeeld dat sprake is van een

periodiek object ten behoeve van 'critical dimension' metrologie, is het doel de vorm van het object zo nauwkeurig mogelijk te bepalen. Anderzijds is voor geïsoleerde objecten het belangrijkste doel slechts om vast te stellen of ze al dan niet aanwezig zijn. De nauwkeurigheid en de convergentiesnelheid van een scatterometry systeem hangen af van de signaal-ruisverhouding van de verstrooide straling, en in dit proefschrift laten wij zien hoe een verbetering van de signaal-ruisverhouding kan worden bereikt door gebruik te maken van de coherentie van de gebruikte verlichting en van de resulterende superpositie van golfamplitudes in het verre veld.

Voor beide object types, periodiek en geïsoleerd, blijft de door ons gewenste nauwkeurigheid binnen de sub-golflengte schaal. Meer specifiek, zijn voor periodieke objecten de vormparameters en hun variaties alle kleiner dan de golflengte van de straling van de verlichtingsbron, terwijl voor geïsoleerde objecten het object zelf kleiner is dan die golflengte.

In de eerste drie hoofdstukken van dit proefschrift wordt het probleem van het periodieke object beschouwd. In het eerste hoofdstuk introduceren wij het concept van optische Fourier scatterometry met coherent licht, *coherent Fourier scatterometry* genaamd. In het volgende hoofdstuk wordt numeriek bewijs geleverd van het voordeel van toepassing van coherent Fourier scatterometry boven state-of-the-art *incoherent Fourier scatterometry* door aan te tonen dat sprake is van gevoeligheidswinst voor alle parameters, tot een factor 8 voor enkele daarvan, onder voorwaarde dat in er in voldoende mate wordt gescand en dat de periode van het object (roosterafstand) groter is dan de golflengte van de verlichting, terwijl de vormparameters van het periodieke object en de variaties daarvan kleiner dan de golflengte blijven. Het derde hoofdstuk laat zien dat deze beperking op de roosterafstand wordt weggenomen door de introductie van een nieuwe versie van coherent Fourier scatterometry door deze te integreren met interferometrie, *interferometric coherent Fourier scatterometry*. Voor deze techniek, waarmee coherentie theoretisch volledig kan worden benut, waardoor een verbetering van de nauwkeurigheid kan worden bereikt voor periodieke objecten met elke mogelijke roosterafstand, kan zoals getoond een verdere verbetering van de gevoeligheid worden verkregen ten opzichte van coherent Fourier scatterometry met een factor 2 tot 5 (dat is dus bijna een orde hoger dan incoherent Fourier scatterometry) voor verschillende parameters. Helaas brengt deze verbetering van de gevoeligheid met zich mee dat meer data moeten worden verwerkt, zodat interferometric coherent Fourier scatterometry meer geoptimaliseerd is voor nauwkeurigheid dan voor snelheid. Er wordt ook een snellere versie van interferometric coherent Fourier scatterometry geïntroduceerd voor toepassingen waarvoor snelle convergentie vereist is, *sectioned interferometric coherent Fourier scatterometry*. Bij deze techniek wordt slechts van een deel van de in totaal bij interferometric coherent Fourier scatterometry beschikbare data gebruik gemaakt, hetgeen veel sneller dan voor normale interferometric coherent Fourier scatterometry kan leiden tot een voldoende nauwkeurig resultaat. Verder hebben wij een korte discussie toegevoegd handelend over kruis-correlatie tussen vormparameters en hoe deze kunnen worden geminimaliseerd met 'nul-correlatie-roosters'. Dit deel van het proefschrift is volledig theoretisch en gebaseerd op numerieke analyse van het probleem, zonder

praktische implementatie.

Vanaf het vierde hoofdstuk wordt ingegaan op de toepassing van coherent Fourier scatterometry voor detectie van geïsoleerde objecten kleiner dan de golflengte. Het beoogde doel in dit deel van het proefschrift was aan te tonen dat coherent Fourier scatterometry ook een geldig alternatief kan zijn voor huidige ter beschikking staande systemen voor de detectie van deeltjes, met het bijkomende voordeel van een gering energiegebruik en een hoge snelheid. Om dit te verwezenlijken was het noodzakelijk het coherent Fourier scatterometry systeem op verschillende punten aan te passen: detectie, verlichting en het proefstuk zelf. De wijzigingen die zijn doorgevoerd in het detectiedeel van het coherent Fourier scatterometry systeem maken het tot een differentieel detectiesysteem, waarmee de nauwkeurigheid en de snelheid van het systeem werden verhoogd. Verder werd de verlichting gemodificeerd teneinde een optimale superpositie van gereflecteerde en verstrooide straling in het verre veld te verzekeren. Tenslotte is het proefstuk aangepast om een verbetering van het contrast te verkrijgen. Deze serie van verbeteringen is achtereenvolgens beschreven in hoofdstuk 4 tot en met 6. De ervaringen die zijn opgedaan tijdens de implementatie van een coherent Fourier scatterometry prototype in een industriële omgeving en de detectie van deeltjes in een bewegende polymeer folie zijn vermeld in hoofdstuk 7. Het laatste hoofdstuk, hoofdstuk 8, bevat enkele vooruitzichten, de mogelijke uitbreidingen op de techniek, en een conclusie van onze lange reis.

Als slot van deze samenvatting is het noodzakelijk een korte beschouwing te weiden aan de mogelijke invloed die dit werk kan hebben op de wetenschappelijke gemeenschap, en in meer brede zin op onze samenleving. Coherent Fourier scatterometry voor periodieke objecten, in essentie eendimensionale rasters, is gericht op het inverse probleem van de reconstructie van de vorm van het raster. Dit probleem is van belang voor het gebied van kwaliteitsbeheersing voor lithografische technieken vanwege zijn nauwkeurigheid, zijn niet-invasieve karakter en zijn snelle convergentie. Wij zijn van mening dat state-of-the-art incoherente systemen, incoherent Fourier scatterometry, kunnen profiteren van technieken die in dit proefschrift worden beschreven waardoor hun nauwkeurigheid kan worden verhoogd. Dit zal leiden tot een betere reconstructie van de vorm in een rumoerige omgeving. Coherent Fourier scatterometry voor geïsoleerde objecten is primair van belang voor objecten met een substraat dat kan worden beschadigd door lange blootstelling aan energie, bijvoorbeeld polymeer folies. Hetzelfde principe echter kan ook worden gebruikt om verontreiniging op halfgeleidersubstraten te detecteren. Dit maakt van coherent Fourier scatterometry een detectiesysteem dat in staat is te werken met verschillende typen materialen. Bovendien kan de methode vanwege haar eenvoudige detectietechniek worden geïmplementeerd in situaties waar snelheid van het grootste belang is, bijvoorbeeld wanneer een hoge doorloopsnelheid in een productielijn moet worden gehandhaafd.

Uitgaande van deze overwegingen hopen wij dat de discussie over coherent Fourier scatterometry in het volgende hoofdstuk van belang zal zijn voor de lezer en de wetenschappelijke gemeenschap, en daarnaast een aanmoediging zal vormen voor verder werk ten voordele van de gemeenschap, door industriële implementatie

van de concepten en de daarbij vergaarde wetenschappelijke kennis.

List of Abbreviations

CD	Critical Dimension
CFS	Coherent Fourier Scatterometry
SNR	Signal to Noise Ratio
CGS	Coherent Goniometric Scatterometry
IFS	Incoherent Fourier Scatterometry
ICFS	Interferometric Coherent Fourier Scatterometry
RCWA	Rigorous Coupled Wave Analysis
NA	numerical aperture
FEM	Finite Element Method
swa	side wall angle
$midcd$	middle critical dimension
csg	coherent sensitivity gain
ICGS	Interferometric Coherent Goniometric Scatterometry
$csgi$	coherent sensitivity gain with interferometry
rms	Root Mean Squared
PSL	PolyStyrene Latex
OLED	Organic Light Emitting Diode
PEDOT	poly-3,4-ethylenedioxythiophene
PSS	poly-styrenesulfonate
ITO	Indium Titanium Oxide
LEP	Light Emitting Polymer
AFM	Atomic Force Microscope
LP	Linear Polarized
QD	Quadrant Detector
LR	Left-Right Signal of quadrant detector
TB	Top-Bottom Signal of quadrant detector
ZL	Zero Line
iSCAT	Interferometric Scattering Microscopy
SLM	Spatial Light Modulator
WGP	Wire Grid Polarizer
EP	percentage enhancement
InSb	Indium Antimonide
GaAs	Gallium Arsenide
ADC	Analog to Digital Converter
FPGA	Field Programmable Gate Array

1

Coherent Fourier Scatterometry

Rather than becoming something that chronicled the progress of the industry,
Moore's Law became something that drove it.

Gordon Moore

1

From the inception of semiconductor transistors [1] in 1947, the electronics industry has progressed rapidly towards small feature sizes, from a few centimeter of the first point-contact transistors to down to 10 nm at present and very recently, 7 nm [2]. This shrinkage in size, following the well-known Moore's Law is due to increasing demand for more packing density to ensure faster, smaller, cheaper and yet efficient electronics for future. The main driving force behind this successful journey is continuous innovations in lithography techniques. This evidently shows why the present techniques, such as the extreme ultraviolet illuminations [3, 4], immersion based optical system [5, 6] and many others are rapidly replacing techniques which are only a few years old. However, it is important to note that taking a step towards successful commercial realization of a new technological node of smaller Critical Dimension (CD) involves solution to several additional issues other than the process of lithography itself.

In this thesis, we discuss the benefits of implementation of a scanning scatterometry technique, the Coherent Fourier Scatterometry (CFS), to address two of those additional issues. The first one is the fast and accurate CD metrology in volume production of semiconductor photolithography, this being one of the main obstacle for rapid process quality verification in commercial lithography techniques. The second one is the estimation of particle contamination in production environment of electronic components, which, in present days, is increasingly involving new materials such as organic polymers together with the conventional inorganic elements. Thus, we will be discussing the performance of CFS for both periodic and isolated objects. However, we would like to make it clear that CFS is not a resolution-enhancement technique, it is sensitivity-enhancement technique which focuses on improving the signal to noise ratio (SNR). For this reason, we consider only periodic or isolated samples, and not samples intended for showing optical resolution enhancement, such as two particle scatterers in close vicinity.

1.1. Introduction

Scatterometry is a very common term in fields of radar technologies, crystal diffraction analysis and nuclear physics. Optical scatterometry is being increasingly used in CD metrology [7, 8], where it has been used with incoherent light for several years and has stood out as one of the most successful solutions to this problem, providing a non-invasive in-situ measurement with extremely high accuracy [9–11]. In this technique measured far field intensity pattern generated by the interaction of an incident field and a sample with periodic permittivity variation is compared with numerically simulated results through rigorous analysis of Maxwell's equations. The final objective of this comparison, generally performed by specialized numerical optimization routine, is to retrieve the CD of the sample as precisely as possible. The periodic sample is often a diffraction grating which is easy to manufacture in larger numbers and for the scope of this thesis, an one-dimensional grating.

Following this common recipe, goniometric scatterometry is perhaps the most well known optical scatterometry configuration [12–15]. Goniometric scatterometry can use coherent illumination as well, and we may call it Coherent Goniometric Scatterometry (CGS). In CGS, generally only one plane wave is used at a time,

while in CFS, many of them can be incident in one shot. Further benefits of CFS to use the phase in the far field makes it more advantageous solution to this problem in certain cases. This will be discussed briefly in this chapter. And a theoretical comparison between the interferometric versions CGS and CFS is done in Chapter 3.

In contrast to CD metrology, use of optical scatterometry for the problem of the estimation of particle contamination on a flat substrate is not very popular to the scientific community as far as the knowledge of the author is concerned. The main reason is the popularity of the dark field detection techniques [16–18] in this problem which has the advantage of separation of the specular reflection and scattered radiation. The reason being that the scattered radiation, of interest for the detection of particle, is generally very weak compared to the specular reflection when small particles are concerned. Thus, the separation of specular and scattered light in dark field detection, obtained by design, definitely increases the SNR. However, the same basic design also implies that a large fraction of radiation incident on the sample is not delivered to the scattering particle but to other parts of sample. This generates heat in the substrate, often over a large area which cannot be dissipated quickly.

On the other hand, while a bright field technique cannot separate the specularly reflected and scattered radiation by design and requires some additional technique to do so, it has the advantage of delivering a larger fraction of the incident radiation to a small location of the sample, thereby avoiding the substrate heating issue. Belonging to this family, CFS, achieves this by scanning the sample. This makes CFS usable for not only inorganic but also to a large fraction of organic samples with low power damage threshold. Moreover, because of its simple and robust configuration, CFS is suitable for integration into the production line. We will make further clarification of this point by comparing the two techniques, bright and dark field, in section 4.1. To clarify the differences in the key parts of the experimental CFS setup for CD metrology and particle detection, we also present a table (table 1.1).

For both CD metrology and particle detection, the basic principle of Fourier Scatterometry remains the same. At the heart of the measurement setup is a microscope objective which focuses the incoming light onto a sample. The reflected-

Table 1.1: CFS setup for CD Metrology and Particle Detection : basic experimental differences

Type	CD Metrology	Particle Detection
Illumination Wavelength	632 nm	405 nm 632 nm (Chapter 6 only)
Numerical Aperture	0.4 or 0.9	0.9
Illumination Polarization	Linear (X or Y)	Linear (X), Radial
Detection Polarization	Linear (X or Y)	Linear (X or Y), Simultaneous Linear (X and Y)
Detector	Camera	Camera, Split (differential) Detector(s)

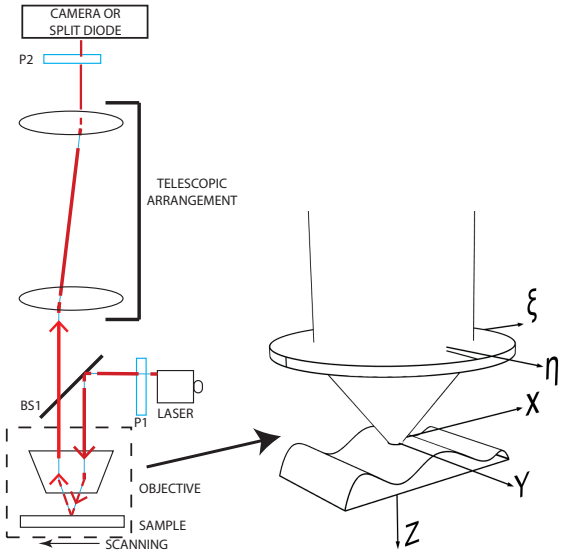

Figure 1.1: The main structure of Fourier Scatterometry is shown in the left side. The polarization arrangement in input (P1), the detection system, the polarization arrangement at output (P2) and the sample structure can be changed to adapt to the specific task at hand, however, the main arrangement (the objective-sample arrangement and beamsplitter BS1) stays the same. This simple configuration make CFS robust and easily integrable to a production line. In the right side, at the heart of Fourier Scatterometry, the objective which focuses the incoming field onto the sample and also collects the scattered light in a so called epi-illumination scheme, is shown together with the co-ordinate system.

scattered field from the substrate is measured in the far-field, which is essentially back focal plane or the exit pupil of the objective. This type of arrangement of the objective and the beamsplitter BS1 forms the so called epi-illumination scheme, making the experimental setup very stable. The incident field is focused at the top of a grating for CD metrology, or at the interface between the incident medium and the substrate for particle detection. Throughout this thesis, this focal plane is considered the $z = 0$ plane or the origin of a Cartesian $x - y - z$ system, with z-axis being the optical axis of the setup and positive along the direction of propagation of incident wave, which is always drawn vertically downwards. CFS is a scanning based technique ($x - y$ scan). To simulate that it was more convenient to assume that the spot was stationary and the sample was moved, this helps us to keep the z axis attached to the spot stationary. This scan is always done in the focal plane. The incident field in the exit pupil of the objective is parallel to the focal plane and so a set of transverse co-ordinates $\xi - \eta$ has been used to designate them. This allows us to express any incident field as functions of ξ and η. Being in far field, these are angular co-ordinates (essentially the normalized components of the wave vector) parallel to $x - y$. These axial arrangement is shown in Fig.1.1.

It is important to mention here the practical problems to use illumination wavelengths in the ultraviolet range or shorter for both CD metrology and particle detection. For CD metrology, ultra violet illumination can create unnecessary exposure of the photo-resist used in semiconductor device fabrication, while for particle detection on polymer substrates it can be absorbed heavily and generate large amount of heat to harm the substrate [19]. This problem is even more serious for polymer substrates with a barrier layer. A barrier layer [20] is a thin layer put on the polymer substrate to protect it from ingress of water and other harmful atmospheric elements, and, some of the popular choices of materials for that layer are highly absorbing for illumination with wavelengths shorter than 400 nm.

In the remaining part of this chapter, the reader is introduced to the numerical simulation tools used in this thesis and the basic concepts, theoretical and experimental, essential for the remainder of this thesis. The first two chapters after this introduction are devoted towards CFS for CD metrology and will be limited to theoretical discussions with numerical examples. The interested reader is encouraged to have a look into [21–24] for further information about experimental implementation of CFS in CD metrology, whereas, here, only theoretically the benefits of CFS compared to conventional Incoherent Fourier Scatterometry (IFS) will be discussed (chapter 2), together with a proposed improvement of CFS to Interferometric Coherent Fourier Scatterometry (ICFS), which has several advantages (chapter 3) compared to the conventional CFS. The next four chapters present the implementation of CFS as a new candidate in the field of particle detection on flat substrate. Several key improvements, which we came upon while working to upgrade CFS as a particle detector on a flat substrate are presented in chapters 4 to 6. The following chapter (chapter 7) presents the results after designing and installing a CFS prototype to detect particle contamination in an industrial environment. This chapter also presents some recent results of detecting highly subwavelength particles. A thesis cannot be completed without a possible outlook for possible improvements.

This is presented in the concluding chapter (8).

1.2. Brief Description of the RCWA algorithm used for CFS CD Metrlogy

Rigorous Coupled Wave Analysis, popularly abbreviated as RCWA, (often also known as Fourier Modal Method) [25, 26] is a powerful tool to numerically analyze effects of electromagnetic radiation for periodic structures. The method was first developed for rectangular structures [27], but was later extended to any grating profile. Several authors contributed toward this extension, however, here we describe the procedure explained in [25].

The basic RCWA algorithm is built upon periodic boundary condition and Flouquet's theorem for gratings. This theorem converts the infinite physical domain into repetition of infinite number of finite domains each spanning the size of the periodicity (Λ) of the grating. Then the method splits the original grating profile into several layers of binary structures of varying work cycle[1] but same pitch Λ, thereby, making an approximate staircase profile replacing the original one. The whole problem is then converted to a simpler problem of propagation of electromagnetic waves through finite number of flat layers, which can be solved using the transfer matrix approach utilizing the continuity of tangential fields. Typically, one starts to find the rigorous solution from the topmost layer, which is encountered by the incident field $\mathbf{E}^i$ first (Fig. 1.2). In each of the layers Maxwell's equations are solved for corresponding rectangular grating at that layer after Fourier expansion of periodic permittivity ε (transverse electric or s-polarization) or inverse of permittivity $1/\varepsilon$ (transverse magnetic or p-polarization). The numerical accuracy of the final solution depends on mainly two parameters. The first is how many terms in the Fourier expansion are retained while solving the Maxwell's equation. The second important point to consider is how accurately the staircase profile can represent the true physical profile. Certainly, increasing the number of layers leads to a better approximation, but numerical instability may occur due to very small thickness of each layer leading to insufficient damping of evanescent waves through these layers. These problems can be overcome in the way as shown in [25], by absorbing the exponential term responsible for that numerical overflow inside the transmittance variable.

The routine we are using is an implementation of the method presented in [28]. This is essentially an implementation of the method described above with some modifications applied to speed up the computational time. The focused spot of CFS (Fig. 1.1) can be expanded into several plane waves which are incident on the grating each with different angle of incidence. The plane waves for which the modulus of sine of the angle of incidence with the z-axis is smaller than the numerical aperture (NA) of the focusing lens will be the only ones that are physically incident. Similarly, the propagating reflected orders for which the modulus of sine of the angle with z-axis is smaller than the NA are also the only ones captured by

[1] We will replace work cycle by the more well defined middle critical dimension later.

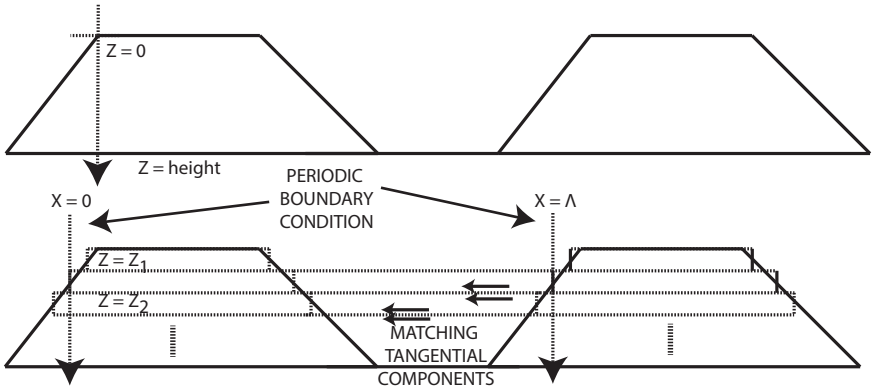

Figure 1.2: The schematics of the RCWA method. The original grating is divided into several layers, with each one containing a rectangular grating. Rigorous solution is then found in each layer and connected to the next layer using continuity of transverse components.

the objective, which are referred to as outgoing waves from here. Therefore, every such incident and outgoing plane waves (denoted in this thesis with superscript 'i' and 'o', respectively) must correspond to a point (ξ, η) space in the entrance pupil of the objective.

Let us assume that ξ^i, η^i in the pupil of the lens refers to a ray with specific wave vector, which when incident on the periodic structure, is reflected into several orders, contributing to a number of output points ξ^o_m, η^o_m in the same objective pupil. They are related by Flouquet's law. Assuming the structure is periodic along $\hat{\boldsymbol{x}} = \hat{\boldsymbol{\xi}}$ only (Fig. 1.1), we have the following relation between the input ($\boldsymbol{k}^i$) and output ($\boldsymbol{k}^o$) wave vectors

$$\boldsymbol{k}^o_\perp = \boldsymbol{k}^i_{m,\perp} + \frac{mk\lambda}{\Lambda}\hat{\boldsymbol{x}}; (-M \leq m \leq M), \tag{1.1}$$

where, $\boldsymbol{k}_\perp = k_x\hat{\boldsymbol{x}} + k_y\hat{\boldsymbol{y}}$ is the transverse component of wave vector $\boldsymbol{k} = (\boldsymbol{k}_\perp, k_z\hat{\boldsymbol{z}})$, and λ is the wavelength of light. This can be alternatively expressed in terms of pupil co-ordinate ξ, η as

$$\begin{aligned} \xi^o_m &= \xi^i + \frac{m\lambda}{\Lambda} \\ \eta^o &= \eta^i, \end{aligned} \tag{1.2}$$

where, we have expressed the x and y components of $\boldsymbol{k}^o_\perp$ in terms of ξ and η, respectively $(\xi, \eta) = 1/k(k_x, k_y)$. We will have to extensively use the (ξ, η) geometry in Chapter 3, and so we delay a detailed discussion till then. At this point, it is important to note that the integer m varies form $+M$ to $-M$, with M being the number of orders considered in the simulation when we retain $2M + 1$ terms in the Fourier expansion of periodic refractive index variation due to the presence of the grating. It is possible that for some value of m, the resulting

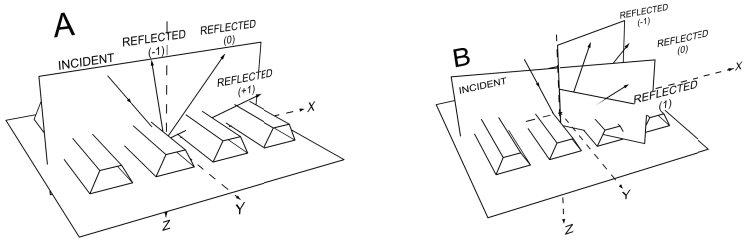

Figure 1.3: The planar (left:A) and conical incidence (right:B). For conical incidence, the s and p polarization components for an outgoing order is defined with respect to the plane the outgoing wave vector makes with the normal (z-axis). This is different than plane of incidence for nonzero orders.

ξ_m^o, η_m^o implies that the reflected-scattered wave is outside the numerical aperture of the objective ($\arcsin\sqrt{(\xi_m^o)^2 + (\eta_m^o)^2} > NA$), or may even be evanescent ($\arcsin\sqrt{(\xi_m^o)^2 + (\eta_m^o)^2} > 1$). It is still important to consider them up to certain extent so that the propagating waves inside the numerical apertures are correctly calculated[2].

To avoid confusion with s and p polarization after the objective we do not use them to indicate the polarization of the incident beam before the objective (or the outgoing beam after the objective), but use y-polarized and x-polarized instead, which directly relates the incident or outgoing beam polarization with the grating periodicity and the geometry of the problem. In a special case, the incident plane waves may have only x-component of propagation vector $\boldsymbol{k}$ ($\eta^i = 0$). This is called planar incidence, in which case the incident and all the reflected orders stay in the same plane, namely $x - z$. This is shown in left (A) of Fig. 1.3. In sectioned Interferometric Coherent Fourier Scatterometry, which will be explained in Chapter 2, this special case is discussed with an interesting example. The general case is the conical incidence, which occurs for incident rays with a nonzero y-component of propagation vector ($\eta^i \neq 0$). In this case, only the zeroth reflected order ($m = 0$) is in the same plane. All the other orders are distributed on a conical surface about the zeroth order. This is shown in right (B) of Fig. 1.3.

Following [28], the symmetry of the structure, when available, may be used to reduce the computational load. This occurs when the incident wavefront is approximately planar and the grating profile is symmetric about y-axis. In that case each quadrant in $\xi - \eta$ plane is equivalent, and so it is enough to compute for one quadrant and copy the result into the other three. In this way, instead of the whole frame with four quadrants, we compute only one quadrant and significant gain in computation time is obtained. But when we use asymmetric gratings, symmetry around y-axis is lost and we need to compute half the field. For non-symmetric illumination, the whole frame has to be computed.

Another important matter in CFS is scanning. In short, scanning is the *main* way

[2]The original RCWA converges slowly for p polarization [29], which is due to nonuniform satisfaction of boundary conditions for this polarization [30]. This problem was corrected in a slightly improved version [31], which we follow here.

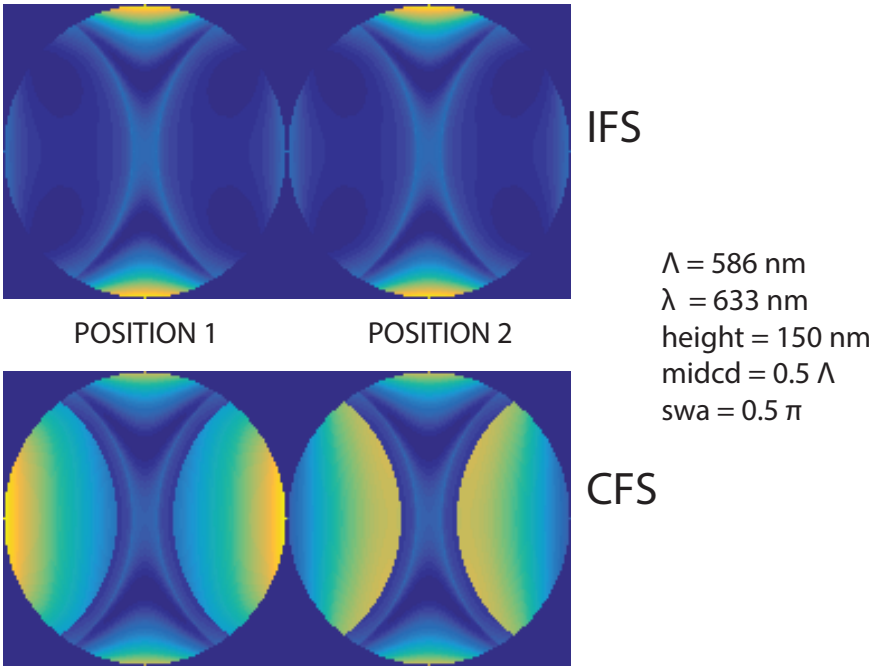

Figure 1.4: The main difference between IFS and CFS is the fact that for CFS, a scan along the grating changes the far field. For IFS, it does not. In this figure, far-fields for two arbitrary scanning positions are shown.

to ensure higher sensitivity in CFS than IFS. We define the scanning in CFS for CD metrology as : the focused spot stays stationary, containing the z-axis or the optical axis through its center and the grating is moved in the $x-y$ plane in the direction of grating vector $\hat{x}$ by an amount equal to the pitch Λ in steps, the number of which can be pre-calculated based on certain information. The key effect making CFS more sensitive compared to IFS is the implicit effect of the phase of the scattered wave in the far-field which manifests itself as a change in intensity distribution with this shift of the grating [32]. This does not occur for incoherent illumination. As a consequence, the point where the center of the spot (or the z-axis) intersects the grating profile is also important, since the exact far field distribution depends on it. This parameter, introduced as $bias$, is also a considered in the RCWA calculation.

1.3. Brief Description of FEM algorithm used for CFS Particle Detector

So far we have discussed the RCWA method which relies on the periodicity of the sample. RCWA for aperiodic structures, introduced by Lalanne and Silberstein [31] for normal incident and later extended by Pisarenco [33], is still not a very popular alternative to integral or differential methods to solve Maxwell's equation for a gen-

eral structure. Here we opt for a specialized Finite Element Method (FEM) tool [34] developed in the Philips Research in Eindhoven and the Optics Group of Delft University of Technology for computations involving isolated scattering particles. FEM is a very popular differential method which is used not only to numerically solve Maxwell's equation but also used very extensively in various boundary value problems of fluid dynamics, thermal, mechanical and structural working environment. We do not feel it is necessary to introduce FEM to the reader, however, to refresh the memory we can recall once the differential equations solved in the FEM implementation for time harmonic electromagnetic fields. For these fields ($\exp(-i\omega t)$) with electric and magnetic amplitudes $\boldsymbol{E}$ and $\boldsymbol{H}$, respectively, the Maxwell's equations take the form :

$$\begin{aligned} \nabla \cdot \varepsilon\varepsilon_0 \boldsymbol{E} &= \rho \\ \nabla \times \boldsymbol{E} &= i\omega\mu\mu_0 \boldsymbol{H}\rho \\ \nabla \cdot \varepsilon\varepsilon_0 \boldsymbol{H} &= 0 \\ \nabla \times \boldsymbol{H} &= \boldsymbol{J}_s + \sigma\boldsymbol{E} - i\omega\varepsilon\varepsilon_0 \boldsymbol{E}\rho, \end{aligned} \tag{1.3}$$

where ρ is the source charge density, $\boldsymbol{J}_s$ is the source current density, σ is the electric conductivity and μ is the permeability. Taking curl of the Faraday's law (2nd in Eq. set 1.5) and modified Ampere's law (4th in Eq. set 1.5), we can get the wave equations:

$$\begin{aligned} \nabla \times \mu^{-1}(\nabla \times \boldsymbol{E}) - k_0^2 \varepsilon \boldsymbol{E} &= i\omega\mu_0 \boldsymbol{J}_s \rho \\ \nabla \times \varepsilon^{-1}(\nabla \times \boldsymbol{H}) - k_0^2 \varepsilon \boldsymbol{H} &= \nabla \times \varepsilon^{-1}(\boldsymbol{J}_s + \sigma\boldsymbol{E})\rho. \end{aligned} \tag{1.4}$$

For non-magnetic materials, an electromagnetic problem is stated by defining certain permittivity distribution. It is the general practice in an electromagnetic FEM procedure to solve the couple of equations in Eq.1.4, subject to the boundary conditions of continuity of tangential components of the field and the discontinuity of normal complements at an interface of a permittivity discontinuity, lets say, medium 1 and medium 2. These connecting equations are given by,

$$\begin{aligned} \hat{n} \cdot (\varepsilon_2 \boldsymbol{E}_2 - \varepsilon_1 \boldsymbol{E}_1) &= \rho_{surf} \\ \hat{n} \cdot (\boldsymbol{H}_2 - \boldsymbol{H}_1) &= 0 \\ \hat{n} \times (\boldsymbol{E}_2 - \boldsymbol{E}_1) &= 0 \\ \hat{n} \times (\mu_2 \boldsymbol{H}_2 - \mu_1 \boldsymbol{H}_1) &= \boldsymbol{J}_{surf}, \end{aligned} \tag{1.5}$$

where by convention, $\hat{n}$ is the outward normal at the interface from medium 1 to 2 and surface charge and current densities are given by ρ_{surf} and $\boldsymbol{J}_{surf}$. The indices 1 and 2 denotes field quantities in medium 1 and 2. In FEM, the computational

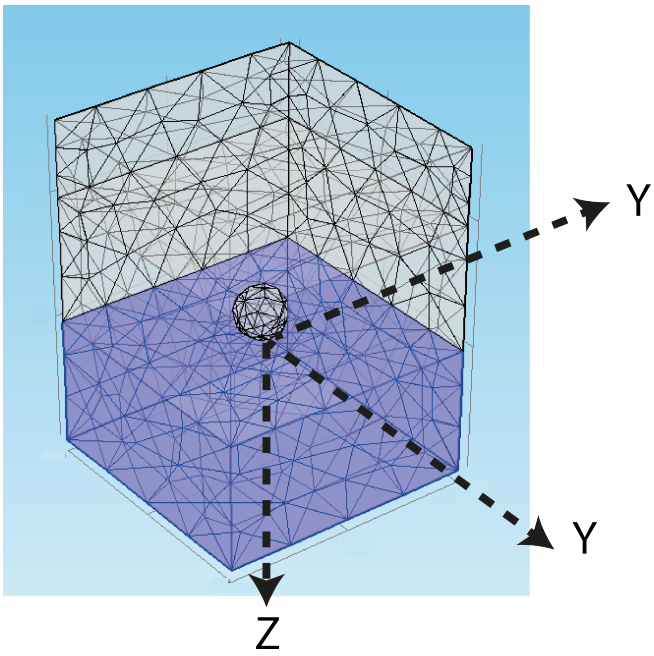

Figure 1.5: The particle on an 'interface' model with free tetrahedral FEM mesh. The model has a two material interface and an sphere sitting on the interface, simulating the particle. The sphere can be shifted in $x-y$ plane to simulate the scanning. Each material has a corresponding perfectly matched layers outside of the the computation domain to damp out numerical reflection. This is not shown in the figure.

domain, essentially a discrete distribution of ε and μ, is divided into several meshes. Then an approximate solution, obeying the boundary conditions, is assumed and is refined iteratively by minimizing the residuals obtained from fitting the approximate solution in Eq. 1.4.

The superiority of FEM to handle complex geometries compared to other methods makes it appealing to the scientist community. More accurate results are obtained with finer meshing. However, the working principle of FEM makes the memory requirements high. This can be significant in 3-dimensional problems when a sufficiently refined mesh is needed for accurate solution.

This specific instance of the FEM used was suitable to simulate a focused field onto a sample [35], as required by CFS design. The standard model (with small variations when necessary) which we have used is shown in Fig. 1.5 as an example. The focused field, with the center of the spot at origin, is introduced in the computation domain from top. To implement that, first vector diffraction integral [36, 37] for the specific field at the entrance pupil of the microscope objective is solved and then the field at the top surface of the computational domain is calculated and inserted. In all 3D FEM computations discussed in this thesis, the computational domain was chosen to be a cube of 1 μm sides, with adaptive mesh (finer near discontinuity of permittivity) with size of $\leq \lambda/10$. The only exception is the FEM simulations shown in part A of Fig. 6.4 of chapter 6, where we used a larger illumination wavelength and consequently increased the computation volume to 1.5 μm sided cubes. This is to ensure that the first zeros of the focused spot always remain completely inside the computational domain.

Figure 1.6: The prototype CFS particle detector installed in production line. The transparent of polymer substrate can be seen under it.

1.4. The Clean4Yield Project

The work described in this thesis was financially supported by *Clean4Yield* [38] project, funded through the European Union's Seventh Framework Program (FP7-NMP-2011) under Grant Agreement No. 281027. Clean4Yield is a collaborative EU-funded project with experts from fourteen European companies and organizations, and one associated partner from Israel. The overall objective of the project was to demonstrate nano-scale inspection, detection, highly efficient cleaning-repair and contamination prevention techniques for flexible polymer substrates in roll-to-roll line. The responsibility of Delft University of Technology was to design and materialize a working prototype of a particle detection system capable of detecting and localizing particle scatterers of diameters from 100 nm to 500 nm.

The motivation of the project was to develop the necessary tools for flexible electronics industry to transit from low-yield sheet-to-sheet production to high yield roll-to-roll production [39, 40]. This implies that a necessary requirement of the prototype inspection tool was high speed to match the desired operating speed of a roll-to-roll line up to 3 meters/minute. The final prototype was installed and tested in March, 2015 in the production environment (Fig. 1.6) at Holst Centre in Eindhoven, The Netherlands and was successfully tested to detect particles at the required speed of the production line. More details about the test results are in Chapter 7.

References

[1] W. SHOCKLEY, *Semiconductor amplifier,* US Patent US2502488 (1950).

[2] *A new wave of innovation in computer chips,* (2015).

[3] H. J. Levinson, ed., *Principles of Lithography* (SPIE Press, 2005).

[4] V. Bakshi, ed., *EUV Lithography* (SPIE Press, 2009).

[5] S. Owa and H. Nagasaka, *Immersion lithography; its potential performance and issues,* Proc. SPIE **5040**, 724 (2003).

[6] R. Dammel, F. M. Houlihan, R. Sakamuri, D. Rentkiewicz, and A. Romano, *193 nm immersion lithography - taking the plunge,* Journal of Photopolymer Science and Technology **17**, 587 (2004).

[7] J. L. Opsal, H. Chu, Y. Wen, Y.-C. Chang, and G. Li, *Fundamental solutions for real-time optical CD metrology,* Proc. SPIE **4689**, 163 (2002).

[8] W. D. Mieher, T. G. Dziura, X. Chen, P. DeCecco, and A. Levy, *Spectroscopic CD metrology for sub-100-nm lithography process control,* Proc. SPIE **4689**, 957 (2002).

[9] P. C. Logofătu, *Sensitivity analysis of grating parameter estimation,* Appl. Opt. **41**, 7179 (2002).

[10] P. Thony, D. Herisson, D. Henry, E. Severgnini, and M. Vasconi, *Review of CD measurement and scatterometry,* AIP Conference Proceedings **683**, 381 (2003).

[11] I. Gereige, S. Robert, S. Thiria, F. Badran, G. Granet, and J. J. Rousseau, *Recognition of diffraction-grating profile using a neural network classifier in optical scatterometry,* J. Opt. Soc. Am. A **25**, 1661 (2008).

[12] P. Boher, M. Luet, T. Leroux, J. Petit, P. Barritault, J. Hazart, and P. Chaton, *Innovative rapid photogoniometry method for CD metrology,* Proc. SPIE **5375**, 1302 (2004).

[13] C. Raymond, *Overview of scatterometry applications in high volume silicon manufacturing,* AIP Conference Proceedings **788**, 394 (2005).

[14] M. Wurm, F. Pilarski, and B. Bodermann, *A new flexible scatterometer for critical dimension metrology,* Review of Scientific Instruments **81**, 023701 (2010).

[15] M. Wurm, S. Bonifer, B. Bodermann, and M. Gerhard, *Comparison of far field characterisation of DOEs with a goniometric DUV-scatterometer and a CCD-based system,* Journal of the European Optical Society - Rapid publications **6** (2011).

[16] P. van der Walle, S. Hannemann, D. van Eijk, W. Mulckhuyse, and J. C. J. van der Donck, *Implementation of background scattering variance reduction on the Rapid Nano particle scanner,* Proc. SPIE **9050**, 905033 (2014).

[17] A. Okamoto, H. Kuniyasu, and T. Hattori, *Detection of 30–40-nm particles on bulk-silicon and SOI wafers using deep UV laser scattering,* IEEE Transactions on Semiconductor Manufacturing **19**, 372 (2006).

[18] J. van der Donck, R. Snel, J. Stortelder, A. Abutan, S. Oostrom, S. van Reek, B. van der Zwan, and P. van der Walle, *Particle detection on flat surfaces,* Proc. SPIE **7969**, 79691S (2011).

[19] J. Pospíšil and S. Nešpurek, *Photostabilization of coatings. mechanisms and performance,* Progress in Polymer Science **25**, 1261 (2000).

[20] G. Deak and S. Jackson, *Film coated with glass barrier layer with metal dopant,* (1992), US Patent 5,084,356.

[21] N. Kumar, O. El Gawhary, S. Roy, S. F. Pereira, and H. P. Urbach, *Phase retrieval between overlapping orders in coherent fourier scatterometry using scanning,* Journal of the European Optical Society - Rapid publications **8** (2013).

[22] N. Kumar, P. Petrik, G. K P Ramanandan, O. El Gawhary, S. Roy, S. F. Pereira, Wim M. J. Coene, and H. P. Urbach, *Reconstruction of sub-wavelength features and nano-positioning of gratings using coherent fourier scatterometry,* Opt. Express **22**, 24678 (2014).

[23] P. Petrik, N. Kumar, M. Fried, B. Fodor, G. Juhasz, S. F. Pereira, S. Burger, and H. P. Urbach, *Fourier ellipsometry - an ellipsometric approach to fourier scatterometry,* Journal of the European Optical Society - Rapid publications **10** (2015).

[24] N. Kumar, O. El Gawhary, S. Roy, S. F. Pereira, and H. P. Urbach, *Phase information in coherent fourier scatterometry,* Proc. SPIE **8788**, 87881P (2013).

[25] M. G. Moharam, T. K. Gaylord, D. A. Pommet, and E. B. Grann, *Stable implementation of the rigorous coupled-wave analysis for surface-relief gratings: enhanced transmittance matrix approach,* J. Opt. Soc. Am. A **12**, 1077 (1995).

[26] L. Li, *Use of fourier series in the analysis of discontinuous periodic structures,* J. Opt. Soc. Am. A **13**, 1870 (1996).

[27] K. Knop, *Rigorous diffraction theory for transmission phase gratings with deep rectangular grooves,* J. Opt. Soc. Am. **68**, 1206 (1978).

[28] M. van Kraaij and J. Maubach, *A more efficient rigorous coupled-wave analysis algorithm, Progress in Industrial Mathematics at ECMI 2004,* Mathematics in Industry, **8**, 164 (2006).

[29] L. Li and C. W. Haggans, *Convergence of the coupled-wave method for metallic lamellar diffraction gratings,* J. Opt. Soc. Am. A **10**, 1184 (1993).

[30] L. Li, *Use of fourier series in the analysis of discontinuous periodic structures,* J. Opt. Soc. Am. A **13**, 1870 (1996).

[31] P. Lalanne and E. Silberstein, *Fourier-modal methods applied to waveguide computational problems,* Opt. Lett. **25**, 1092 (2000).

[32] O. El Gawhary, N. Kumar, S. F. Pereira, W. M.J. Coene, and H. P. Urbach, *Performance analysis of coherent optical scatterometry,* Applied Physics B **105**, 775 (2011).

[33] M. Pisarenco, J. Maubach, I. Setija, and R. Mattheij, *Aperiodic fourier modal method in contrast-field formulation for simulation of scattering from finite structures,* J. Opt. Soc. Am. A **27**, 2423 (2010).

[34] X. Wei, A. J. Wachters, and H. P. Urbach, *Finite-element model for three-dimensional optical scattering problems,* J. Opt. Soc. Am. A **24**, 866 (2007).

[35] A. C. Assafrao, S. F. Pereira, and H. P. Urbach, *On the focused field embedded in a super rens medium,* Jpn. J. Appl. Phys. 102206 **50** (2011).

[36] E. Wolf, *Electromagnetic diffraction in optical systems. I. an integral representation of the image field,* Proceedings of the Royal Society of London A: Mathematical, Physical and Engineering Sciences **253**, 349 (1959).

[37] B. Richards and E. Wolf, *Electromagnetic diffraction in optical systems. II. structure of the image field in an aplanatic system,* Proceedings of the Royal Society of London A: Mathematical, Physical and Engineering Sciences **253**, 358 (1959).

[38] *Official clean4yield project website,* (2015).

[39] R. R. Søndergaard, M. Hösel, and F. C. Krebs, *Roll-to-roll fabrication of large area functional organic materials,* Journal of Polymer Science Part B: Polymer Physics **51**, 16 (2013).

[40] F. Krebs, T. Tromholt, and M. Jorgensen, *Upscaling of polymer solar cell fabrication using full roll-to-roll processing,* Nanoscale **2**, 873 (2010).

2

CFS for Nano-metrology : Application on Gratings

I also pursued another dream - of a microscope,
not optical, but entirely mechanical.

Marvin Minsky in his Memoir on Inventing the Confocal Scanning Microscope [3]

Parts of this chapter have been published in Journal of the European Optical Society - Rapid publications **7**, 0 (2012) [1], except for section 2.5, which is published in Proceedings of Fringe, 2013; pp. 43-48 [2].

2.1. Introduction

This chapter is devoted to show the advantage of CFS over IFS, which we will investigate numerically, with an emphasis to show the importance of scanning in CFS. It is organized as follows. In the next section, we define a model for the typical grating we intend to retrieve by expressing its parameters as a vector, which may include the position of the grating with respect to the center of the spot as unknown, since the actual far field intensity pattern depends on it. We will be using this parameter vector in the next chapter as well. In the third section we introduce the relevant mathematical relations which we need to perform a sensitivity analysis, followed by the fourth section where we present the results. This section has two parts. At first, with explicit examples, we analyze the role of scanning and show how scanning helps to achieve better sensitivity in CFS and incorporate robustness in measurement. Then we discuss more about finding the position of the grating with respect to the center of the spot. In the final section, we discuss about another important issue other than parameter sensitivity, the cross-correlation between different parameters and its importance in scatterometry including the interesting case of 'zero cross-correlation gratings'.

2.2. Experimental conditions and definition of the grating vector

Let us consider a simple experiment in which a one-dimensional silicon grating having a profile of a trapezium[1] is illuminated by an ideal CFS system, i.e., it is at the focussed field of a diffraction limited objective with spatially coherent incident wavefront. As was already mentioned in 1.1, when operating in reflection the same objective is used to collect the reflected wavefront forming a so-called epi-illumination arrangement. Two polarizers are placed in paths of incoming and outgoing fields to independently polarize either or both of them. We will be considering ideal cases, i.e., a perfectly plane incident wavefront, absorption-free and diffraction-limited objective lens performance and ideal polarizers. Also, by coherent beam we mean complete spatial coherence and for incoherent beam complete spatial incoherence. The substrate and grating materials can in general have complex refractive indices, whereas, the medium surrounding the grating has real refractive index. The convention we follow in this thesis is that the grating is placed such that the grating vector is oriented along $\hat{x}$. Thus, for the incident beam before the objective (or the outgoing beam after the objective) the linearly polarized electric field perpendicular to the groove is referred to x-polarization and for the electric field along the groove, it is designated as y-polarization.

As was mentioned in section 1.1, the main difference between CFS and IFS is the phase shift occurring in CFS as the grating is shifted by a small amount Δx. A proof of this can be found in [4]. We can write the following formula for this phase

[1] Trapezium shaped gratings are commonly used for CD metrology in semiconductor manufacturing processes.

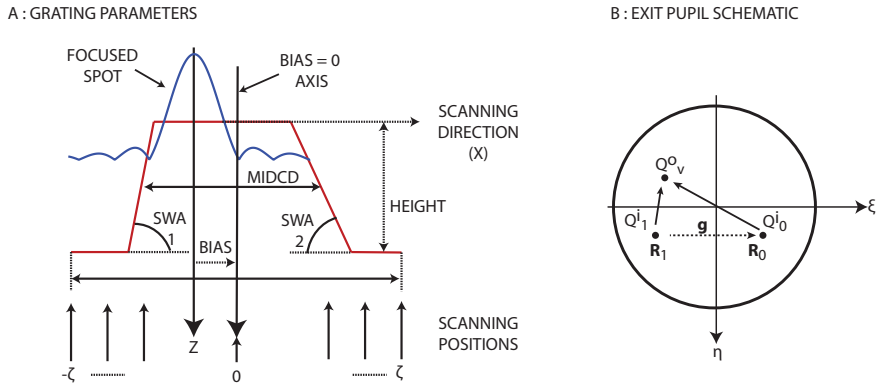

Figure 2.1: In the left (A), the grating parameters and the scanning are defined. Center of the $midcd$ defines the $bias = 0$ position, which, in general, does not coincide with z axis (the z axis, passing through the center of the spot, is the optical axis of the setup and is always attached to the spot). The scanning positions are designated by ζ. If the grating vector has only x-component, scan is done along x and ζth scanning position denotes a shift of $\zeta \Delta x$ from origin where Δx is the scanning step size. In the right side (B) the pupil of the objective is shown schematically. This is an example where the outgoing wave at Q^o_v is contributed by the zeroth order from incident wave at Q^i_0 and first order from incident wave at Q^i_1. x-component of wave vector at Q^i_0 and at Q^i_1 are separated by grating vector $\boldsymbol{g}$.

shift for an one-dimensional planar grating with grating vector $\boldsymbol{g} = \frac{2\pi}{\Lambda}\hat{\boldsymbol{x}}$,

$$\boldsymbol{R}'_m = \boldsymbol{R}_m \exp\left[i2\pi\left(\frac{m\Delta x}{\Lambda}\right)\right], \tag{2.1}$$

where, $\boldsymbol{R}'_m$ is the complex diffraction amplitudes for the m^{th} order after shifting $\Delta\boldsymbol{x}$ from its initial position, where the complex diffraction amplitudes were $\boldsymbol{R}_m$. There is no change when $m = 0$, i.e, for zero order. This means that CFS works differently than IFS only when at least one nonzero order is present. We can formally define scanning in CFS for one dimensional grating samples as capture of several frames by applying small shifts of the grating in the direction of its grating vector (i.e., x-axis) till the grating is displaced by the distance of one pitch. For the present context of one dimensional grating, as discussed in chapter 1.2, the scans are done along x. A typical CFS measurement will consist of several frames placed side by side, which, we call a superframe. This dependence of CFS far field with respect to the grating position compels us to define the position of the grating with respect to the optical axis. This is made through an additional parameter called $bias$.

In left of Fig. 2.1, the parameters defining the shape of the grating are shown. $height$ is the maximum height in the work cycle, swa are side walled angles (left is $swa1$ and right is $swa2$) and $midcd$ (MIDdle Critical Dimension, replacing the commonly used work cycle) is the width of the trapezium at half the height. Other choices are also possible but nonetheless this one makes a sufficient set. The possible lateral misalignment is taken care by $bias$, as mentioned before. The zero bias position is defined as the situation when the center of one period (as shown in Fig. 2.1), coincides with the optical axis (z) which is always attached to the center

of the focused spot. Any nonzero bias ($bias = 0$ axis and z axis do not coincide) implies some lateral misalignment. The scans are symmetrically distributed around the $bias = 0$ axis spanning the length of one pitch. The separation between them, which depends on the number of scanning positions we choose and the actual value of the pitch, is called shift. This is denoted as Δx in Eq. 2.1. If the number of scanning positions on one side of the $bias = 0$ axis including the one on the axis is given by ζ, then, with the configuration explained above we will have $2\zeta - 1$ scan positions inside the pitch for a given ζ where the first and the final one have identical far field for being exactly one period away. This implies that we will have effectively $2\zeta - 2$ independent scan positions. This way of numbering scans ensures that we get a symmetric scanning, however, this also implies that number of independent scan positions can only be even. We keep this numbering convention for this chapter, but in the next chapter we change the convention to allow any number of independent scanning positions, even or odd. To be noted, in the same scheme, no-scan implies $\zeta = 1$. To be noted when $bias = 0$ then the $bias = 0$ axis and z axis coincide, and scanning is then symmetrically distributed with respect to the z axis as well as the grating profile.

Taking all these into account, the vector defining the geometry of the grating was chosen to be

$$\boldsymbol{a} = [height, swa1, swa2, midcd, bias]. \tag{2.2}$$

For convenience, we will also assume symmetric grating with $swa1 = swa2$. This simplified assumption does not influence the general outcomes and leads to the simplified parameter vector

$$\boldsymbol{a} = [height, swa, midcd, bias]. \tag{2.3}$$

In an even simplistic case the position of the grating is assumed to be known as a priori information from some other way, we can further reduce the parameter vector to the most simple form $[height, swa, midcd]$, which should be the easiest one to investigate. It may be argued that dropping a physical parameter like this will create an error in the sensitivity analysis since the physical model is no longer sufficiently defined by the remaining parameters. However, as we will show later, this is approximately justified since $bias$ is almost uncorrelated to other shape parameters and it does not influence the parameter sensitivities provided sufficient scanning is performed. On the other hand, this will make the comparison of CFS and IFS much simpler and straightforward.

2.3. Mathematical relations for sensitivity analysis

In order to establish a scheme for the comparison of CFS from IFS, we have chosen to analyze the difference of sensitivities of each method and make a comparison between them. Given a merit function, the uncertainty matrix can be related to the Hessian of the function, and then elements of the inverse of this matrix will correspond to the sensitivities of different parameters. This approach is used by

many authors to analyze the precision of critical dimension metrology. One can, for example, refer to [5] or [6], for a brief or a detailed discussion, respectively.

Let a function f represent our model which transforms the input field into output intensity by simulating the reflection from the grating of the spot focussed by the objective on it. Many waves coming from different incident fields may be diffracted into the same outgoing pixel Q_v^o in the exit pupil (right of Fig. 2.1) this function can map many input waves to one output intensity value, i.e., $I(Q_v^o) = f_v(Q_0^i, Q_1^i, \ldots; \boldsymbol{a})$, where $I(Q_v^o)$ denotes the total intensity of the outgoing wave in pixel Q_v^o of exit pupil. Since we have assumed the incident beam as planar, so, $I(Q_v^o)$ depends only on those incident plane waves, namely waves passing through $Q_0^i, Q_1^i, \ldots$ in the entrance pupil[2], which contribute to the outgoing plane wave at Q_v^o. Let us define a least square merit function

$$\chi^2 = \sum_{v=1}^{(2\zeta-1)\times V} \left[\frac{I_v^{meas} - I(Q_v^o)}{\sigma_v}\right]^2, \tag{2.4}$$

where, I_v^{meas} is the experimentally measured intensity, V is the total number of pixels in a single fame containing whole pupil data, σ_v is the standard deviation of noise at pixel Q_v^o assuming a normal distribution. We already know, from the discussion of scanning following Fig. 2.1, one coherent superframe contains $2\zeta - 1$ frames, and that is why the sum extends to $(2\zeta - 1) \times V$. The covariance matrix is defined by $\boldsymbol{C} = \boldsymbol{A}^{-1}$, where elements of $\boldsymbol{A}$ are given by the Hessian matrix

$$A_{jk} = \sum_{v=1}^{(2\zeta-1)\times V} \frac{1}{\sigma_v^2}\left[\frac{\partial f_v}{\partial a_j}\frac{\partial f_v}{\partial a_k}\right]. \tag{2.5}$$

$\boldsymbol{C}$ gives us the variances and covariances of the parameters. We can find 3-sigma uncertainties from the diagonal elements of $\boldsymbol{C}$, while, the off-diagonal terms of $\boldsymbol{C}$ shows covariances between the parameters. The formula for uncertainty in parameter a_j is

$$\Delta a_j = 3\sqrt{(2\zeta - 1)VC_{jj}}. \tag{2.6}$$

The multiplication with number of pixels in a superframe is to allow the results to be independent of the number of pixels used in a specific simulation. This is needed to make a fair comparison between CFS and IFS owing to larger number of data in CFS.

Eq. 2.6 gives the 3-sigma uncertainty per unit pixel per unit noise standard deviation for j^{th} parameter. To make the desired comparison between CFS and IFS, we define coherent sensitivity gain $\boldsymbol{csg}$

$$csg_j = \frac{\Delta a_{j,incoherent}}{\Delta a_{j,coherent}}. \tag{2.7}$$

[2] To be noted that Q_v^o, Q_0^i and Q_1^i are two dimensional vectors in pupil plane (ξ, η). Here real integer $v \in [1, V]$ denotes a pixel in the pupil. In practice, a single frame will require a pixel to be designated by two integers, v_1 and v_2, as we will be using in chapter 4, but we can assume all pixels arrayed linearly for calculation of uncertainty.

From Eq. 2.7, it is apparent that for a pixel-independent noise, csg is same for any noise level. However, to determine the exact uncertainty, one has to put the noise value in Eq. 2.6.

We would like to introduce an useful parameter to help us understand the difference between CFS and IFS, the overlap variable F, defined as

$$F = \frac{\lambda}{\Lambda\ NA}, \tag{2.8}$$

where λ is the illuminating wavelength, NA is the numerical aperture of the objective and Λ is the period/pitch of the grating. This overlap variable is important quantity in CFS as it takes into account the system (illumination wavelength and NA) and the sample (pitch) factors together. We want to concentrate on mostly the geometrical effects as F is varied, so it is desirable to vary F by changing the pitch only. This is justified since pitch is assumed to be known and we are reasonably free to adjust it to obtain maximum sensitivity. Since we keep the wavelength of illumination constant, we can keep the same refractive index throughout the calculations.

To fix a certain range of F, let us consider F varying from 0.7 to 2.2, since this range of F includes most interesting features. For $F > 2$ there is no order other than zeroth which is captured by the system, so, according to Eq. 2.1, no effect of scanning can be seen in the far field. If this is the case, then coherent and incoherent scatterometry gives the same far field and the sensitivities of both processes should be identical. Thus $F = 2$ defines the lower limit for the pitch that is useful for obtaining the benefits of coherent scatterometry. This effect can be used as a check for reliability of the simulations. The values of F such as $1 < F \leq 2$ is the region where only zeroth and first orders are captured. In this region, the pupil starts to get populated by two beam interferences and the difference between coherent and incoherent far-field starts to build up. In the region $0.67 < F \leq 1$ the second order starts to be captured and most of the pupil is now the result of three-beam interference. The coherence of light starts to play a strong role here and significant change in the far field is expected, so also any effect due to scanning. Further lowering of F will lead to even larger pitch and more interferences. This is to be avoided as this calls for rapid increase of numerical complexity and accordingly the computational time, making the overall optimization required at the final step of CFS rather slow which is unacceptable in any practical environment. This is also not interesting for practical applications as grating period Λ becomes impractically large.

There are a few things to consider regarding no-scan CFS before we proceed further. The basic difference in the far-field of CFS is the amplitude superposition compared to IFS, which is intensity superposition. With no-scan CFS is not very robust and the sensitivity can be unpredictably low in special cases. This is due to the fact that for no-scan CFS it is more likely that the change of intensity level in a far-field pixel is minimal. It may happen because amplitude superposition manifests itself as squared modulus of superposed complex amplitude, in which the separate changes due to real amplitude and phase may be of opposite sign and cancel each other. Moreover, in a specific pixel, there is some probability that the resultant

intensity is zero and so without scanning this pixel is very sensitive to noise. By the same logic there may be some cases where no scan can give better sensitivity for some parameter than experiments with more scans, due to coincidental constructive interference in another pixel. This probability reduces with scanning, in which only the phase part of the superposed complex amplitude is varied, the real amplitude remain the same. As a result the chances of these accidental sensitivity gain or loss for no-scan case is greatly reduced. That is why for no-scan one can see very high or very low sensitivity in special cases. These are very special cases and general conclusions cannot be drawn from them, and, in most cases they will disappear or reappear in some random manner for a different NA, shape of the grating or $bias$.

2.4. Results of Sensitivity Analysis

In the remaining part of this section, we consider a specific grating as our sample. This grating is assumed to be made of silicon on a silicon substrate and the medium surrounding the the grating is air. We will assume the illumination wavelength to be 633 nm for this chapter and the next. At this wavelength the complex refractive index of silicon is $3.882 - i0.019$. Regarding sensitivity analysis simulations, the derivatives in Eq. 2.5 are computed by finite differences where the size of the grids has been fixed to 0.1 nm and the angular grid is 0.1 degrees. The incident polarization is linear and can be x or y, where we assume no polarizer at the output.

A typical nominal shape of the grating $[height, swa, midcd] = [150, 90, 0.5]$ (in nm, degree and fraction of pitch), is chosen without any special consideration for which we first analyze the sensitivity variation with pitch assuming that the $bias$ is known. Later we remove this restriction. The $height$ is chosen in the range as normally used in scatterometric measurements and 90 degree swa is most commonly used for binary gratings. As the pitch is varying, the $midcd$ is kept scaled to half of the pitch so that as the pitch decreases the grating profile is not becoming very small, and the incident field can still 'see' the refractive index variation. The $bias$ is kept at zero, i.e., the optical axis divides the profile symmetrically (Fig. 2.1). The specific choice of $bias$ does influence the sensitivity when no scanning is done but this influence becomes almost non-existent with sufficient scanning, as is shown later. The results were calculated using RCWA (chapter 1.2) with the number of Fourier modes retained are 30 (positive and negative), which has been tested to give sufficient convergence in the the range of F as mentioned earlier for silicon grating with 633 nm illumination and for both s and p polarization.

2.4.1. Sensitivity Gain in Coherent Fourier Scatterometry

Fig. 2.2 shows the results for csg for height with no polarizer at the output and the input is x-polarized (part A) or y-polarized (part B) for a numerical aperture of 0.4. The red line shows csg for no-scan ($\zeta = 1$) and the blue line is for minimal scan ($\zeta = 2$) of two scanning positions. As expected, csg starts to vary for $F \leq 2$. For no scan it oscillates till F is greater than 1, and starts to show a steady increase with smaller F. More than one scanning position increases the stability and the gain stays *always* above unity. Thus we may conclude that CFS is more sensitive than

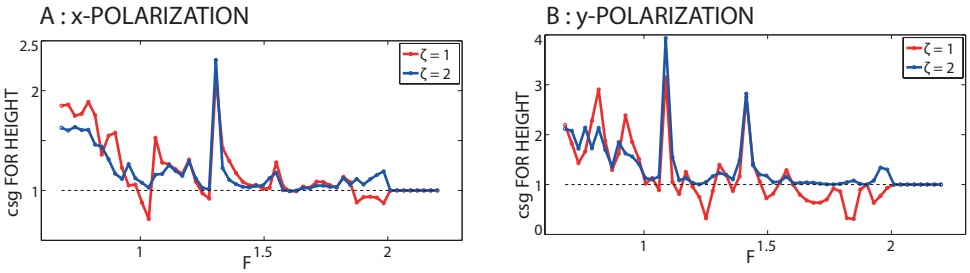

Figure 2.2: csg for height is plotted for no-scan ($\zeta = 1$, red) and minimal scan ($\zeta = 2$, blue) for incident beam polarization x (in A : left) and y (in B : right) with no polarizer at the output. The NA is 0.4.

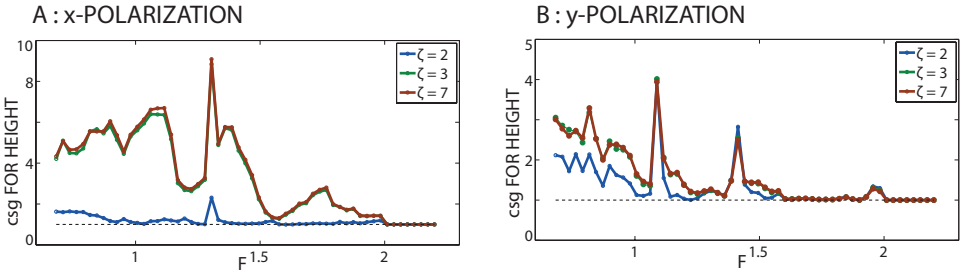

Figure 2.3: csg for height is plotted for minimal scan ($\zeta = 2$, blue), $\zeta = 3$ (green) and $\zeta = 7$ (brown) for incident beam polarization x (in A : left) and y (in B : right) with no polarizer at the output. The NA is 0.4.

IFS when scanning is employed. However, the gain may be made larger and more stable with more scanning, which is the next step to investigate.

Fig. 2.3 shows how the csg for height is improved upon addition of more scans and how this improvement is dependent on the polarization of the incident wave. Clearly, addition of more scans improve the $\boldsymbol{csg}$ although naturally there is an optimum number of scanning beyond which the gain is marginal. This number depends on the overlap parameter F through the number of interfering waves. The number of optimum scanning positions increases when more orders overlap, i.e., when F decreases. This effect is more clearly visible for relatively larger NA. Here a comparison between $\zeta = 3$ and $\zeta = 7$ reveals this effective optimum number to be $\zeta = 3$, or in other words, 4 scans. Also in this example the effect of scanning seems to have a more dominant effect when the incident light is polarized along x.

To show whether these conclusions are true for larger NA, which is normally used for practical scatterometry applications, the relevant plot of csg for height is shown in Fig. 2.4 for $NA = 0.9$. The basic nature of the plot is similar to the previous results involving smaller NA. With the larger NA, it can be noted that the optimum number of scans is changed from 4 ($\zeta = 3$) to 6 ($\zeta = 4$), which is clearly visible for y-polarization when F decreases below 1 and the second order comes inside the aperture. This effect is less for x-polarization possibly due to smaller change in the far field for this case. The behavior of other two shape parameters, namely swa

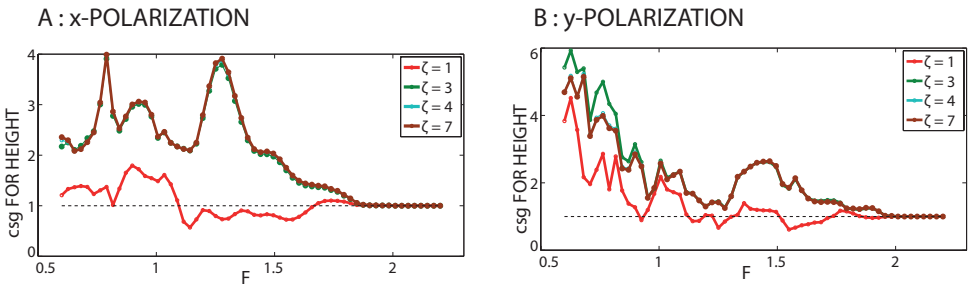

Figure 2.4: csg for height is plotted for no-scan (red), $\zeta = 3$ (green), $\zeta = 4$ (light blue) and $\zeta = 7$ (brown) for incident beam polarization x (in A : left) and y (in B : right) with no polarizer at the output. Note the change in the number of optimum scan positions, more apparent for input polarization y, as F becomes less than 1 and the second order is captured. The NA is 0.9.

Table 2.1: Optimum scanning positions in CFS

Range of F	No. of overlapping Orders	Optimum independent Scanning Positions $(2\zeta - 2)$
$F > 2$	None	No scanning needed
$2 > F \geq 1$	2 (zeroth and first)	3 ($\zeta = 3$)
$1 > F \geq 0.67$	3 (zeroth, first and second)	6 ($\zeta = 4$)

and $midcd$, can also be seen to be of similar nature. To avoid repetition we show only the results for no-scan and $\zeta = 3$, in top row of Fig. 2.5 for $midcd$ and bottom row of Fig. 2.5 for swa. A quick reference of optimum scan positions with overlap parameter F is given in table 2.1.

Table 2.1 can be explained drawing an analogy between CFS and phase-shifting-interferometry. When there are two orders superposing, it requires at least three phase-shifts for complete knowledge of interfering fields. This happens when $2 > F \geq 1$. By the same logic the number of required scanning positions required increases to 6 as F decreases below 1 and the second order is captured, resulting in three-wave-interference in each pixel. Recalling that according to our convention of numbering scanning positions, one can only have even number of independent scans $(2\zeta - 2)$ for a given ζ. Thus, when we need only 3 scanning positions, we need to set $\zeta = 3$. This problem can be overcome by numbering scanning positions differently, which is done in Chapter 3.

Let us now show with an example how the parameter $bias$, or the physical positioning of the grating under the spot, plays a role in uncertainty of another parameter. This is to justify the simplification of the parameter vector we made earlier about the fact that $bias$ is almost uncorrelated with other parameters. In Fig. 2.6 we show the 3-sigma uncertainty per pixel, as defined in Eq. 2.6, of $height$ with no-scan and $\zeta = 3$ with different values of $bias$. The example is for incident beam polarization x. The behavior of y-polarized incident beam is similar and not repeated. We assumed the standard deviation of the noise to be independent of

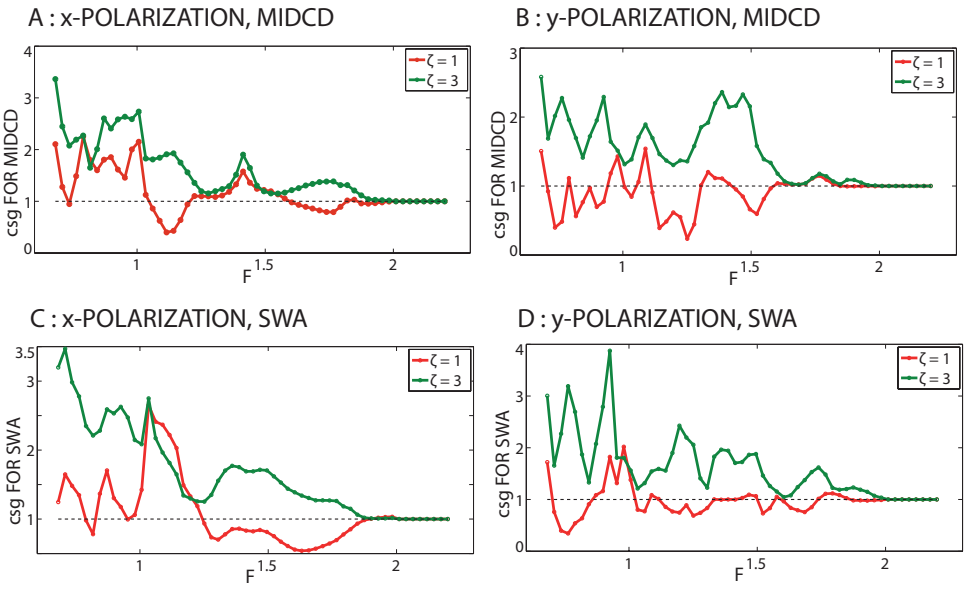

Figure 2.5: Top Row : csg for $MIDCD$ is plotted for no-scan (red) and $\zeta = 3$ (green) for incident beam polarization x (in A : left) and y (in B : right) with no polarizer at the output. Bottom Row: csg for swa is plotted for no-scan (red) and $\zeta = 3$ (green) for incident beam polarization x (in C : left) and y (in D : right) also with no polarizer at the output. The NA is 0.9.

pixel position having a value of $\sigma_{noise} = 1 \times 10^{-4}$ [7]. This level of noise is standard in IFS if some noise reduction image processing is done on experimental data. This gives an uncertainty in height of about 0.2 nm with scanning. From the values of the uncertainties in both plots it can be seen that the uncertainties are significantly lowered and stabilized with scanning. This means that exact positioning of the sample is not important if sufficient scanning is done and a possible choice of F can be made without considering effects due to specific position of the grating. Conversely, it indicates sufficient scanning results in small correlation between $bias$ with shape parameters and an independent determination of $bias$ may be possible without retrieval of shape parameters. This justifies our simplification of the parameter vector at the end of section 2.2. This results also show how scanning can lead to a stable behavior of the system.

2.4.2. Retrieval of $bias$: CFS for grating nano-positioning

After establishing the gain in sensitivity in CFS compared to IFS the next step would be to extend the usefulness of CFS to take into account the additional parameter $bias$ defining the position of the sample with respect to optical axis of the system.

There is a difference to determine the uncertainty of the $bias$ than the uncertainty of shape parameters. Since zeroth order is invariant towards any change in bias ($m = 0$ in Eq. 2.1), the number of pixels whose intensity is dependent on $bias$ increases as the F decreases, essentially being equal to the difference between the

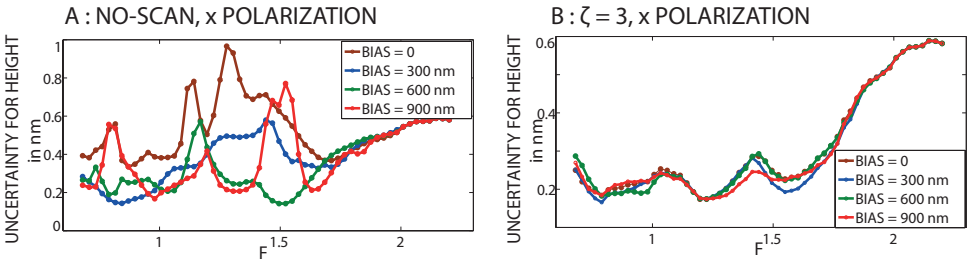

Figure 2.6: 3 sigma uncertainty per unit pixel with $\sigma_{noise} = 1 \times 10^{-4}$ for $height$ is plotted for no-scan (in A : left) and $\zeta = 3$ (in B : right) for incident beam polarization x with no polarizer at the output. In each plot sensitivities of different $bias$ values (0, 300 nm, 600 nm, and 900 nm) are shown in different color. The NA is 0.9. Note the drop of uncertainty as the scanning is introduced.

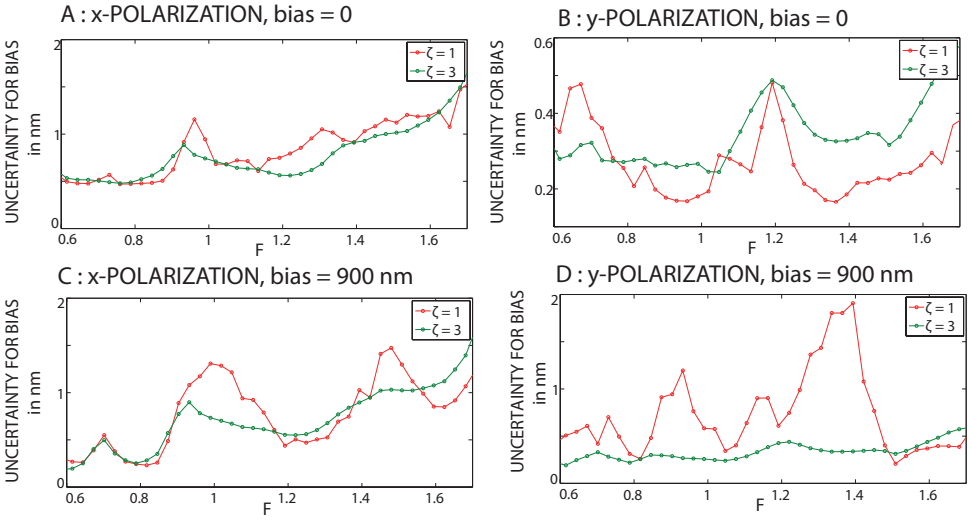

Figure 2.7: 3 sigma uncertainty per unit pixel with $\sigma_{noise} = 1 \times 10^{-4}$ for $bias$ is plotted for no-scan (red) and $\zeta = 3$ (green) for two input polarization x and y and no polarizer at the output. The top row is for $bias = 0$ and the bottom row is for $bias = 900nm$. The NA is 0.9.

total number of pixels and the pixels containing only zeroth order. If this is called V_{int} then Eq. 2.6 for $bias$ becomes

$$\Delta bias = 3\sqrt{(2S-1)V_{int}C_{jj}}. \tag{2.9}$$

Unlike V, V_{int} is a function of F and goes to zero for $F \geq 2$. As $F \to 2^{-}$, these contributing pixels will start to appear towards the edge of the aperture and are prone to be noisy. For $bias$ determination, thus, it is beneficial to keep F smaller so that sufficient samples exist with adequate SNR to allow for a faithful determination of $bias$. In the simulation we avoid this case by restricting ourselves to $F \leq 1.7$ so that no error arises due to the sharp reduction in number of data points that arises after this value of F. To obtain the uncertainties in $bias$ we may plot it for various scans. As shown in Fig. 2.7, the uncertainty ranges between 1 to 2 nm and is often about 0.5 nm. This is for a noise standard deviation of 1×10^{-4} as mentioned earlier. To be noted, due to small correlation of $bias$ with other parameters, it can be independently optimized with a reasonable a-priori knowledge of the grating sample. We have taken two examples here at $bias = 0$ and at $bias = 900nm$. Surprisingly, in $bias = 0$ case and y-polarization, no scan performs better than the multiple scanning for a large range of values of F. This is probably coincidental as it appears specifically for that $bias$. Also, since $bias$ is not a shape parameter scanning may have a less dominant effect to reduce the uncertainty in this case. Nonetheless, with this level of uncertainty for positioning, CFS seems to be a good and convenient tool for nano-positioning. For the experimental implementation of retrieval of $bias$, one can refer to Ref. [8].

2.5. The cross-correlation between two parameters

In reconstruction of grating parameters from optical scatterometry data the most important problem is optimization, which is quite prone to diverge even if the nominal values are quite close to the real values. The reason behind this is the highly ill-posed nature of grating parameter reconstruction, or in general, the ill-posedness of inverse diffraction problems [4, 9]. The final convergence depends on many factors, to name a few - a good set of nominal values, low noise in measurements and proper regularization of data. However, the speed of convergence and its accuracy are largely influenced by two factors - large sensitivity of most parameters and small correlation between maximum possible pairs of parameters. The final values are selected with a proper trade-off between these two factors as it is highly unlikely to have the best in both simultaneously. So far in this chapter we have discussed about sensitivity of individual parameters and in this section we will discuss about the cross-correlation of parameters.

The normalized cross-correlation can be obtained with little effort from the knowledge of covariance matrix $\boldsymbol{C}$ from Eq. 2.5, and it is given by Ref. [2]

$$\boldsymbol{C}_{cor} = (1 \circ \boldsymbol{C})^{-1}\, \boldsymbol{C}\, (1 \circ \boldsymbol{C})^{-1}, \tag{2.10}$$

where, $\circ$ denotes the Hadamard Product.

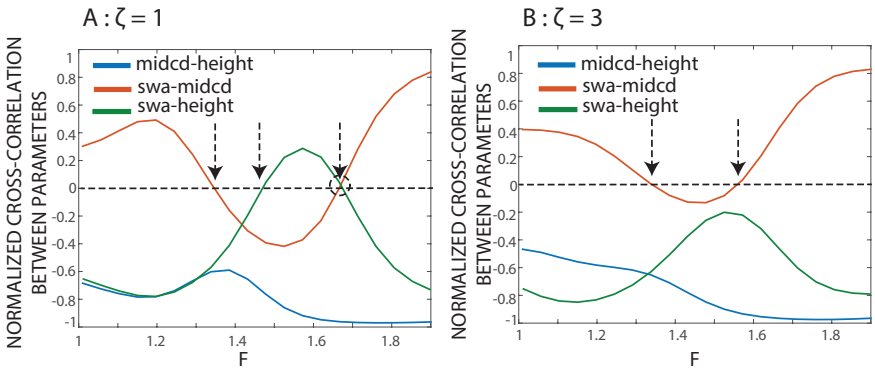

Figure 2.8: Variation of normalized cross-correlation of pairs of shape parameters with F. In the left side (A) the cross-correlations are plotted for no-scan, while on the right side (B) they are plotted for $\zeta = 3$. A reduction of peak-to-valley variation of cross-correlations are seen. The plots are for incident x-polarized beam and no polarizer at output, with $NA = 0.9$.

Fig. 2.8 shows the normalized cross-correlation between $height$, $midcd$ and swa for range $1 \leq F \leq 1.9$. Again we do not consider $bias$ as a parameter for these plots for the same reason as was discussed before. The plot in the left is for no-scan, whereas, the plot in the right is for sufficient scanning in the range of F ($\zeta = 3$). We can readily note the stabilization of cross-correlation terms with scanning, the difference between the maximum and minimum values for cross-correlation between swa-midcd and swa-height is decreased almost by half. This, unfortunately, has some negative practical consequence since the average cross-correlation becomes non-zero. On the other hand, this shows that the parameters are indeed physically correlated.

An important point to note is the fact that in some cases, cross-correlations change sign. This gives the so-called 'zero cross-correlation gratings' for which two parameters are uncorrelated. This happens in several places in Fig. 2.8, especially in the case of no-scan. Interestingly, for no-scan at $F \approx 1.68$, where we have a situation where swa is practically uncorrelated with $height$ and $midcd$, since both cross-correlation terms with swa are close to zero. Although interesting, it is not recommended to obtain CFS data without scanning, as we have already discussed. There are also cases when $swa - midcd$ correlation goes to zero for sufficiently scanned data, which may be a better set of nominal values to use.

We must also take the parameter sensitivity values before making a decision to take the 'zero cross-correlation gratings' as nominal values, since it may happen that the parameter sensitivities for that grating is so low that the practical advantage from small cross-correlation becomes negligible.

2.6. Conclusion

In this chapter we discussed on the benefits of CFS compared to IFS, with an emphasis on scanning in CFS. More specifically, through rigorous sensitivity analysis

we showed how scanning can lead to larger sensitivity in determination of shape parameters. This fact remains true for different numerical aperture of the objective of which we showed only two examples here, a smaller NA of 0.4 and a larger NA of 0.9. We found that given a value of the overlap parameter F, there exists an optimum number of scan positions. This number can be directly related to phase shifting interferometry if we consider the scanning to be an operation similar to phase-shifting of reference waves.

Another important message from this chapter is that with sufficient scanning it is possible to reduce the correlation of bias and shape parameters. This has two advantages, firstly, the choice of specific value of overlap parameter F for which all the shape parameters have sufficiently high sensitivity can be made regardless of the specific $bias$ of the grating; and secondly, an independent determination of $bias$ should be possible when shape parameters are not of interest. Both of these are desirable to make CFS a flexible tool for two different application, grating nano-positioning and CD meterology. Thereafter, we showed that positioning of the grating with respect to axis of the optical system can be achieved to an accuracy of fraction of nanometers in CFS under standard practical conditions of optical nano-metrology. With a standard deviation of noise $\sigma_{noise} = 1 \times 10^{-3}$, which is normally obtained without strict noise control, a positional uncertainty of 5 nm and height uncertainty of 2 nm is predicted to be possible in CFS. Finally, we discussed about cross-correlation of parameters, and showed how they can be stabilized with sufficient scanning, with few examples showing 'zero-cross correlation gratings'.

References

[1] S. Roy, O. El Gawhary, N. Kumar, S. F. Pereira, and H. P. Urbach, *Scanning effects in coherent fourier scatterometry,* Journal of the European Optical Society - Rapid publications **7** (2012).

[2] S. Roy, N. Kumar, S. F. Pereira, and H. P. Urbach, *Fringe 2013*, edited by W. Osten (Springer Berlin Heidelberg, 2014) pp. 43–48.

[3] M. Minsky, *Memoir on inventing the confocal scanning microscope,* Scanning **10**, 128 (1988).

[4] O. El Gawhary, N. Kumar, S. F. Pereira, W. M.J. Coene, and H. P. Urbach, *Performance analysis of coherent optical scatterometry,* Applied Physics B **105**, 775 (2011).

[5] R. Silver, T. Germer, R. Attota, B. M. Barnes, B. Bunday, J. Allgair, E. Marx, and J. Jun, *Fundamental limits of optical critical dimension metrology: a simulation study,* Proc. SPIE **6518,65180U** (2007).

[6] S. A. T. William H. Press, Brian P. Flannery and W. T. Vetterling, *Numerical recipes in C*, 2nd ed. (Camebridge University Press, 1992) pp. 661–663.

[7] H. Gross and A. Rathsfeld, *Sensitivity analysis for indirect measurement in scatterometry and the reconstruction of periodic grating structures,* Waves in Random and Complex Media **18**, 129 (2008).

[8] N. Kumar, P. Petrik, G. K P Ramanandan, O. El Gawhary, S. Roy, S. F. Pereira, Wim M. J. Coene, and H. P. Urbach, *Reconstruction of sub-wavelength features and nano-positioning of gratings using coherent fourier scatterometry,* Opt. Express **22**, 24678 (2014).

[9] D. Colton and R. Kress, *Inverse Acoustic and Electromagnetic Scattering Theory*, 2nd ed. (Springler, Heidelberg, 1998) pp. 85–93.

3

CFS for Nano-metrology : Interferometric Coherent Fourier Scatterometry

It is clearly granted by Newton, that there are undulations, yet he denies that they constitute light; but it is shown in the first three Corollaries and the last proposition, that in all cases the increase or diminution of light are referable to an increase or diminution of such undulations, and that all the affections to which the undulations will be liable, are distinctly visible in the phenomena of light; it may be therefore very logically inferred, that the undulations are light.

Thomas Young on Newton's corpuscular theory of light [3]

Parts of this chapter have been published in J. Opt. **324**, 289 (2013) [1], except for section 3.4, which is published in Proceedings of Fringe, 2013; pp. 43-48 [2].

3.1. Introduction

From the previous chapter, we learned that in CFS the overlapping orders interfere and the measured total intensity depends on the phase difference between them. As has been shown in [4], the intensities and phase differences of the overlapping orders can be retrieved by scanning the focused spot over the period of the grating. This makes CFS similar to a common path interferometer. The information about the overlapping orders can be retrieved in CFS provided the pitch is large enough. Since this is lacking in IFS, the sensitivity for grating shape parameters is considerably higher in CFS. However, if the pitch is so small that reflected orders higher than the zeroth order can not be captured by the objective, there is no difference in sensitivity between the coherent and incoherent versions of Fourier scatterometry. In this chapter, we show a way to overcome this problem. The rest of this chapter contains only theoretical discussion; the experimental verification of these concepts has been submitted very recently[1] [5].

Other than using scanning to get benefitted from using the phase information implicit in superposition of overlapping orders, there is also another area to improve CFS. In original CFS, which we discussed so far, information (implicit or explicit) about phases of individual scattered waves with respect to the incident wave is not available. The available phase information is only about the phase differences between them. If this information would also be available, even higher sensitivity is expected.

One conceivable way to solve both of these issues is by letting the outgoing wave interfere with a reference beam [6]. We shall refer to the combination of CFS with phase-shifting-interferometry as Interferometric Coherent Fourier Scatterometry (ICFS), to distinguish it from the original version of CFS.

With these motivations, the purpose of this chapter is to investigate by simulations the gain in sensitivity that can be expected with ICFS. The intensities and phase differences of overlapping orders are again obtained by scanning the spot, just as in conventional CFS, whereas the phases of the total scattered field is obtained by interfering the outgoing beam with a reference beam. The latter can always be done independent of the value of the pitch, hence in contrast with CFS, ICFS should always give a higher sensitivity compared to IFS, even for very small pitch ($F > 2$). Two orthogonal polarizations, x and y, as defined and used before, are again chosen for the incident and outgoing beam. To ensure maximum contrast, the polarization of the reference beam is chosen parallel to that of the outgoing beam. As will be shown in this chapter, with ICFS the complete complex scattering matrices can be determined for all reflected orders and all incident waves inside the numerical aperture of the objective. Hence, for given NA, with ICFS the maximum possible information about the scattered far field (i.e., the intensities and phases for all combinations of incident and outgoing polarization states) is available to reconstruct the grating parameters. Interestingly, we will show that by adding interferometry, the minimum number of scanning positions that is needed to retrieve the overlapping orders is less than the required minimum scanning positions

[1] One can have a look at section 8.1 for possible outlooks regarding this

under similar conditions in the conventional CFS.

Recently, extension of CFS with white light interferometry has been reported [7], where, a polychromatic source has been used to produce a reference wave that interferes with the scattered wave from the sample. However, interference with a monochromatic source should lead us closer to determining the full scattering matrix ([8, 9]) of the system, and so, towards maximum sensitivity to solve the ill-posed inverse grating problem. Also, it should allow us to limit the size of the data, thereby helping to achieve faster optimization.

At this point, the Coherent Goniometric scatterometry (CGS), mentioned in section 1.1, can be introduced in slightly more detail. Schematically illustrated in part A of Fig. 3.1, in goniometric scatterometry, plane waves corresponding to a specific of set of incident angles interact with the grating one at a time and the intensities of the reflected orders are measured. It can be done for all combinations of polarizations in the incident and outgoing beams. Being very well known, this technique gives us a good standard to compare ICFS with. Moreover, if this technique is extended by interferometry with a reference beam, the full information about the complex scattering matrix can also be retrieved as in ICFS. One may thus expect that the sensitivity for the grating parameters of Interferometric Coherent Goniometric Scatterometry (ICGS) must be the same as ICFS. Interestingly, as we will show later, the sensitivity of ICFS is larger if the pitch of the grating is large ($F \leq 2$), but the same for smaller pitch ($F > 2$).

This chapter is organized as follows, in section 3.2 we describe the model for CFS and ICFS. In section 3.3 we present the results of simulations and we discuss the sensitivity gain that can be obtained with ICFS. Then we discuss a special variation of CFS/ICFS, in which we consider only part of the data which produces a considerable gain in computation time without significant loss in parameter sensitivity. The final section, section 3.5, contains the conclusions.

3.2. Modeling of the Coherent Fourier Scatterometry

Let us first recall quickly how the data is captured in CFS. The focused spot can be expanded into plane waves that are incident on the grating. The sine of the angle of incidence of these plane waves with the z-axis must be smaller than the NA of the focusing objective. The interaction of an incident plane wave with the grating leads to diffracted orders. The propagating reflected orders of which the sine of the angle with the the z-axis (normal of the grating) is smaller than the NA, are captured by the objective and detected by a camera conjugate with the objective exit pupil. This way, every plane wave whose angle of incidence or angle of reflection with the normal of the grating is within the NA of the objective corresponds to a point in the pupil of the objective, respectively in the entrance and in the exit pupil.

From the discussion of previous chapter, if overlap parameter $1 < F \leq 2$; then the $+1, -1$ and 0th order are captured by the objective. Consequently, for some directions of the reflected beam, the total complex amplitude is the sum of a field that is the 0th reflected order of some incident wave and a field that is the $+1$th reflected order of another incident wave. Let us assume the number of outgoing orders which overlap is N. As long as $F > 1$, the -1th and $+1$th reflected orders

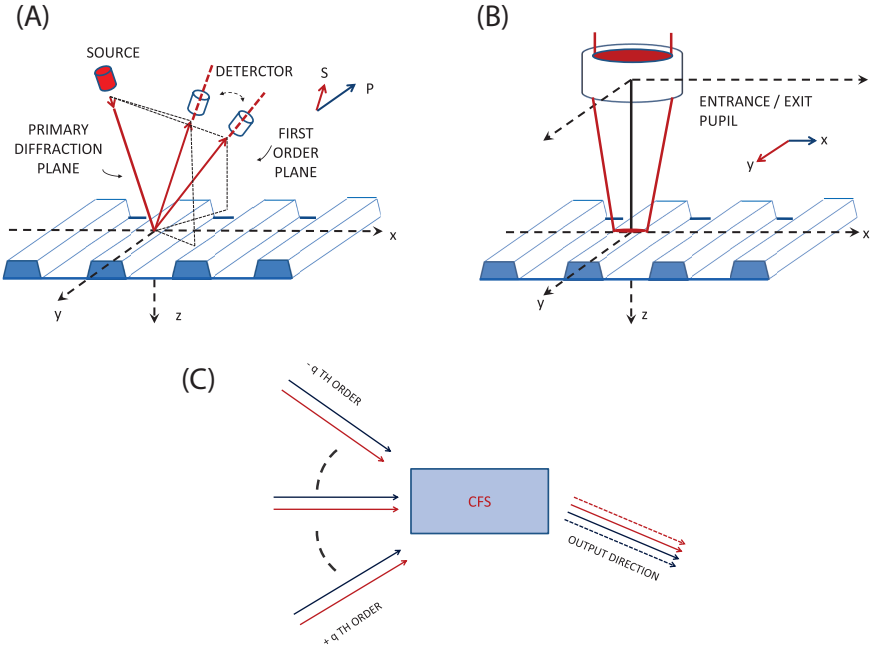

Figure 3.1: The schematics of CGS and CFS for an one dimensional grating. Like before, the co-ordinate system is such that x is the direction of periodicity of the grating. Two different orthogonal polarizations are shown in different colors, red and blue. In top left (A), simple schematics of CGS is shown. Each time a plane wave with a specific incident angle is incident on the grating, and the outgoing orders are collected. Each outgoing plane wave(s) can be made to interact with a reference beam to store the interference pattern, which will contain all the phase information, and this scheme, although maybe too slow to be realized in practice, is called ICGS. In top right (B), the a schematic diagram for CFS is presented. In bottom row (C) a block diagram of a CFS system is illustrated. Here we look at one outgoing direction in the pupil plane in which several incident 'red' or 'blue' waves can contribute depending on the pitch of the grating. When practically realized, (red,blue) can be seen as (s and p) in Coherent Goniometric Scatterometry and (y, x) in CFS.

never overlap, hence for $1 < F \leq 2$ we have $N = 2$, even though the total number of outgoing orders captured by the objective is 3 (visual examples are situations in bottom row of Fig. 1.4). As an example of the superposition for $N = 2$, we redraw part (B) of the Fig. 2.1 with more detail here in (A) of Fig. 3.2. The contributing orders are zeroth from Q_0^i and the first from Q_1^i, which appear in pupil point Q_v^o corresponding to outgoing wave vector $\boldsymbol{k}_v^o$. In part (B) of the same figure the relation between the basis (ξ, η) and (s, p) is shown in terms of azimuth angle φ.

As mentioned in Chapter 2.6, we also slightly change the convention of numbering scanning position ζ in this chapter. This is explained in Fig. 3.3. Now scans are numbered from $\zeta = (0, 1, \ldots \zeta_{min} - 1)$ and spans from $bias = 0$ axis to $bias = \Lambda$ axis. With this new convention, it will be easier to differentiate between scanning and phase-shifting (introduced later in this chapter). The basic physical definition stays of scanning stays the same.

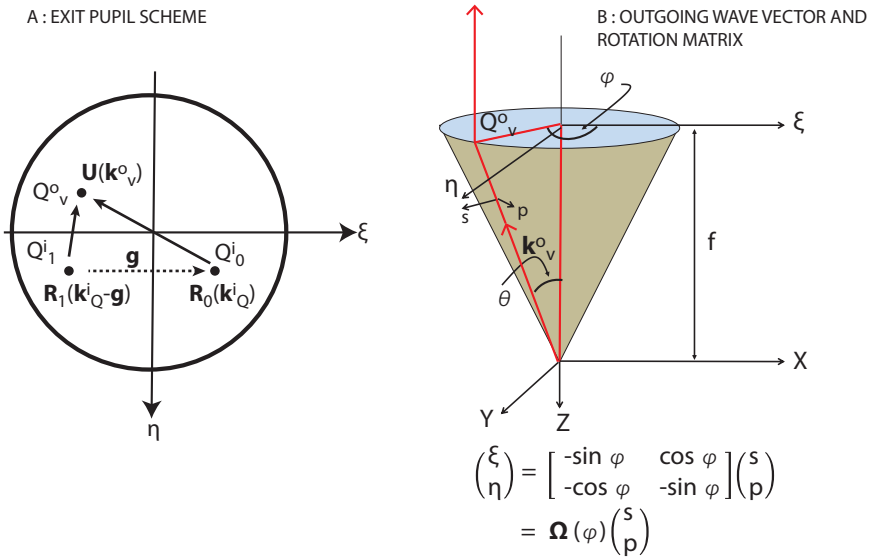

Figure 3.2: In left A: A pixel Q_v^o in the pupil corresponding to scattered transverse wavevector $\boldsymbol{k}_v^o$ is contributed by the waves from direction $\boldsymbol{k}_Q^i$ (corresponding pixel Q_0^i) and $\boldsymbol{k}_Q^i - \boldsymbol{g}$ (corresponding pixel Q_1^i), respectively through the superposition of their zeroth and first order. Here $\boldsymbol{g}$ is the grating vector, assumed to have only x-component. In right B: shows the polarization transformation matrix as shown in Eq. 3.1. The azimuthal (φ) and incidence (θ) angles are given by $\varphi = \tan^{-1}(\eta/\xi)$ and $\theta = \sin^{-1}\sqrt{\xi^2+\eta^2}$. Therefore, the polar coordinates (ρ, φ) is essentially $(\sin\theta, \varphi)$. Precisely, the rotation matrix transforms ξ-η to the polar basis ρ, φ, which are related to s and p polarization by unit matrix. Given the s and p components and the angles θ, φ; one has sufficient information to define the incident wave. Here, we do not consider any anisotropy of the objective.

As the number of superposing orders are determined by F, the minimum number of scanning positions (ζ_{min}) needed to obtain maximum sensitivity can be determined from table 2.1. With the new convention of numbering scanning positions, we can have odd numbered scans which was not possible with previous notation as it allowed only even numbered scans. From the table 2.1, $\zeta_{min} = 1$ if $F > 2$, $\zeta_{min} = 3$ in the range $1 < F \leq 2$, $\zeta_{min} = 6$ in the range $0.67 < F \leq 1$.

To simulate CFS for an objective of given NA, we express the incident wave vector in the $(\hat{\boldsymbol{x}}, \hat{\boldsymbol{y}})$-basis. The incident field in a given point Q_0^i of the pupil having pupil coordinates (ξ, η), is related to a unique plane wave incident on the grating with wave vector $\boldsymbol{k}_Q^i$. It's projection on the (x, y)-plane is given by (see chapter 1.2 and in part B of Fig. 3.2) :

$$\boldsymbol{k}_{Q,\perp}^i = -nk_0(\xi\hat{\boldsymbol{x}} + \eta\hat{\boldsymbol{y}}). \tag{3.1}$$

Here, n is the refractive index of the incident medium. Since the z-component of the wave vector is fixed once $\boldsymbol{k}_{Q,\perp}^i$ is specified, $\boldsymbol{k}_{Q,\perp}^i$ can be thought of as an unique direction. Each wave vector of the field scattered by the grating is similarly related to a particular pupil point as in (3.1). For example, in (A) of Fig. 3.2, for Q_0^i: $\xi, \eta > 0$; for Q_1^i: $\xi < 0, \eta > 0$ and for Q_0: $\xi, \eta < 0$.

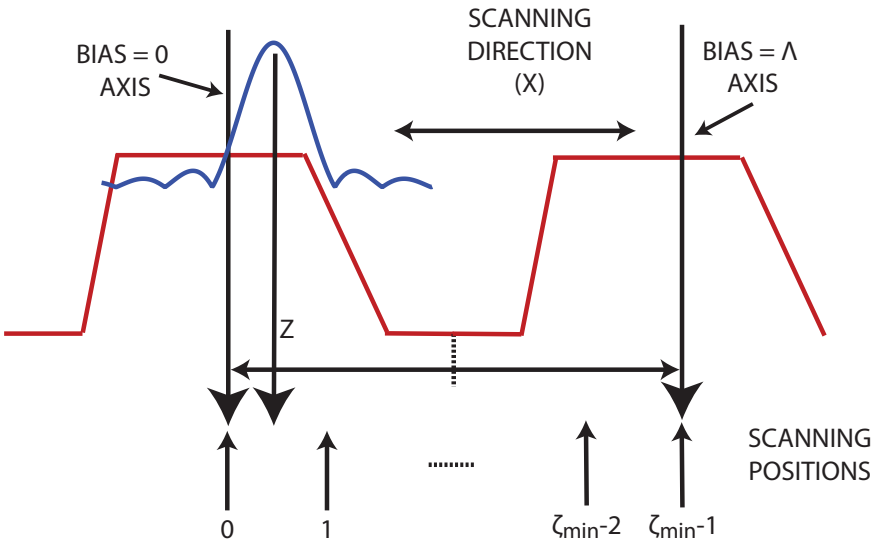

Figure 3.3: For convenience, we redefine how the scanning positions are numbered use a different convention than chapter 2 for this chapter. Now scans are numbered from $\zeta = (0, 1, \ldots \zeta_{min} - 1)$ and spans from $bias = 0$ axis to $bias = \Lambda$ axis (instead of numbered from $-\zeta$ to ζ and spanning across $bias = 0$ axis symmetrically). As before, the grating vector has only x-component, scan is done along x-axis and ζth scanning position denotes a shift of $\zeta \Delta x$ from origin where Δx is the scanning step size.

Now suppose that the mth reflected order with $M_1 \leq m \leq M_2$ contribute to the total outgoing wave with transverse wave vector $\boldsymbol{k}^o_{Q,\perp}$ corresponding to pupil point Q. Here M_1 and M_2 are the largest and the smallest number orders, respectively, which can be captured by the optical system and contribute to the total field of this reflected wave, (i.e., we have $N = |M_1| + M_2 + 1$, with N as introduced earlier)[2].

According to Flouquet's theorem, the transverse components of the incident wave vector $\boldsymbol{k}^i_{m,Q}$ whose mth reflected order is in the direction of $\boldsymbol{k}^o_Q$ satisfy:

$$\boldsymbol{k}^o_{Q,\perp} = \boldsymbol{k}^i_{m,Q,\perp} + m\boldsymbol{g}. \tag{3.2}$$

We must keep in mind that when expressed in terms of ξ and η, the scattered and incident wave vectors will have components with opposite signs, in accordance with the laws of vector addition. Also, as was introduced in Eq. 2.1 and illustrated in Fig. 3.2, $\boldsymbol{g}$ is the grating vector, which, for our one dimensional grating is given by (Fig. 3.1):

$$\boldsymbol{g} = \frac{2\pi}{\Lambda}\hat{\boldsymbol{x}}. \tag{3.3}$$

With this, we can write the total complex reflected field $\boldsymbol{b}$ in the pupil point Q

[2]From chapter 1.2, we know the maximum number of orders to be considered for the RCWA to converge as $2M + 1$, which is different and always larger than N

as[3]

$$\boldsymbol{b}(\boldsymbol{k}_Q^o) = \sum_{m=M_1(\boldsymbol{k}_{m,Q}^i)}^{M_2(\boldsymbol{k}_{m,Q}^i)} \boldsymbol{R}_m(\boldsymbol{k}_{m,Q}^i)\boldsymbol{a}(\boldsymbol{k}_{m,Q}^i). \tag{3.4}$$

Here $\boldsymbol{R}_m(\boldsymbol{k}_{m,Q}^i)$ is the 2×2 matrix giving mth order complex diffraction amplitudes in reflection, for a wave with complex amplitude $\boldsymbol{a}(\boldsymbol{k}_{m,Q}^i)$ incident from the direction with transverse projection $\boldsymbol{k}_{m,Q}^i$[4]. Note that the reflection matrix in (3.4) relates fields in the objective pupil, i.e. $\boldsymbol{b}$ and $\boldsymbol{a}$ are both fields in the pupil. The reason for this is that the polarizer of the incident field is in the entrance pupil of the objective before focusing and the analyzer of the outgoing beam is in the exit pupil after collimation. The incident field $\boldsymbol{a}$ in the pupil can be measured (amplitude and phase) by a wavefront sensor and can be expressed as a complex vector field dependent on pupil co-ordinates (ξ, η). Given the incident wave vector $\boldsymbol{k}_{m,Q}^i$, the matrix $\boldsymbol{R}_m$ is dependent on the shape of the grating, and so, is of central interest to us. We can write the reflection matrix for an linearly polarized incident beam as,

$$\boldsymbol{R}_{m,\Delta x}(\boldsymbol{k}_{m,Q}^i) = \begin{pmatrix} r_m^{xx}(\boldsymbol{k}_{m,Q}^i) & r_m^{xy}(\boldsymbol{k}_{m,Q}^i) \\ r_m^{yx}(\boldsymbol{k}_{m,Q}^i) & r_m^{yy}(\boldsymbol{k}_{m,Q}^i) \end{pmatrix} \exp(img\Delta x), \tag{3.5}$$

where, for example, superscript xy denotes polarization scheme x in the outgoing field and y in incident field, etc[5]. The overall phase factor, which forms the basis of scanning, appears due to shift of the grating by Δx (measured from the z-axis to the center of the pitch when the grating is in a specific scanning position) along the x-axis.

A general conically incident incoming wave with azimuthal angle φ and incidence angle θ (part B of Fig. 3.2) can be split in s and p polarized components (with respect to the plane of incidence), rigorously solved for interaction with grating and the output field can be similarly expanded. The commonly used reflection matrix for the interaction of a plane wave with a grating gives the reflection coefficients of the outgoing orders with respect to this s and p basis. To distinguish it from the matrix defined above, will denote this matrix for order m by $\boldsymbol{R}_m^R$. Its relation with $\boldsymbol{R}_{m,\Delta x}$ is (see [4] for details):

$$\boldsymbol{R}_{m,\Delta x} = fac(\theta, \theta_m)\boldsymbol{\Omega}(\varphi)\boldsymbol{R}_m^R\boldsymbol{\Omega}^{-1}(\varphi_m)\exp(img\Delta x). \tag{3.6}$$

Here $\Omega(\varphi_m)^{-1}$ is a rotation matrix that relates the incident field in pupil point Q_m^i with polar coordinates (ρ_m, φ_m) of the objective from the x, y basis to the s, p basis. This intermediate basis (ρ, φ) is illustrated in part B in Fig. 3.2. Thus, the pupil point

[3] In other chapters we have referred to the incident and outgoing (reflected) fields as $\boldsymbol{A}^i$ and $\boldsymbol{A}^o$, respectively. However, to simplify the equations in this chapter, we designate two different letters $\boldsymbol{a}$ and $\boldsymbol{b}$ to represent the incident and outgoing fields. We go back to the normal notations, $\boldsymbol{A}^i$ and $\boldsymbol{A}^o$, in other chapters.

[4] For simplifying the notations, we drop $\perp$ from now on in this chapter and by $\boldsymbol{k}$, we will mean that transverse components of wave vector automatically, unless explicitly specified

[5] The i, when inside exponent, has the traditional meaning of imaginary number. The incident field is denoted by an i in the superscript.

Q_m^i corresponds to the incident wave vector $\boldsymbol{k}_{m,Q}^i$ whose mth reflected order is in the direction of the outgoing wave vector $\boldsymbol{k}_v^o$, which, in turn, corresponds to pupil point Q_v^o with coordinates (ρ, φ). The reflection matrix $\boldsymbol{R}_m^R$ gives the reflected mth order on the s and p-basis. The rotation matrix $\Omega(\varphi)$ transfers the s and p components of the mth reflected order back to the x, y basis (see B of Fig. 3.2). Thus, $\boldsymbol{R}_{m,\Delta x}$ can be assumed to operate on the basis of x, y only. The scalar factor $fac(\theta, \theta_m)$ is necessary for conservation of the energy flux[6] [10].

Going back to Eq. 3.5, for each direction of scattering, the whole reflection process can be expressed by a set of N complex 2×2 matrices. Obtaining sufficient information to determine this scattering matrices is our main interest. Let us assume for simplicity that in an experiment with the μ-ν polarization scheme (μ or ν each can be either x or y) only the zeroth and the first orders (positive and negative) are captured but the positive and negative first orders do not overlap. This being the situation for which $1 < F \leq 2$. This is also the case shown in part A of Fig. 3.2. The total complex amplitude of the outgoing wave in the direction of $\boldsymbol{k}_v^o$ is then given by:

$$\begin{aligned} b_{\Delta x}^{\mu\nu}(\boldsymbol{k}_v^o) &= r_0^{\mu\nu}(\boldsymbol{k}_v^o) a^\nu(\boldsymbol{k}_v^o) \\ &\quad + r_1^{\mu\nu}(\boldsymbol{k}_v^o - \boldsymbol{g}) a^\nu(\boldsymbol{k}_v^o - \boldsymbol{g}) \exp(img\Delta x), \end{aligned} \tag{3.7}$$

where, Eq. 3.2 has been used to express the incident wave vectors in terms of the outgoing scattered wave vector. By symmetry, a similar expression will hold for superposition of the zeroth and the negative first order. The positive and the negative first orders do not superpose unless $F < 1$. Thus we can consider only one of the superpositions, namely, Eq. 3.7, and the analysis for the other superposition will be identical. The intensity in the pupil plane is

$$\begin{aligned} |b_{\Delta x}^{\mu\nu}(\boldsymbol{k}_v^o)|^2 &= |r_0^{\mu\nu}(\boldsymbol{k}_v^o) a^\nu(\boldsymbol{k}_v^o)|^2 + |r_1^{\mu\nu}(\boldsymbol{k}_v^o - \boldsymbol{g}) a^\nu(\boldsymbol{k}_v^o - \boldsymbol{g})|^2 \\ &\quad + 2|r_0^{\mu\nu}(\boldsymbol{k}_v^o) a^\nu(\boldsymbol{k}_v^o)||r_1^{\mu\nu}(\boldsymbol{k}_v^o - \boldsymbol{g}) a^\nu(\boldsymbol{k}_v^o - \boldsymbol{g})| \\ &\quad \times \cos[(\arg r_0^{\mu\nu}(\boldsymbol{k}_v^o) - \arg r_1^{\mu\nu}(\boldsymbol{k}_v^o - \boldsymbol{g}) + \\ &\quad \arg a^\nu(\boldsymbol{k}_v^o) - \arg a^\nu(\boldsymbol{k}_v^o - \boldsymbol{g}) - g\Delta x)], \end{aligned} \tag{3.8}$$

where, $\arg(r_m^{\mu\nu})$ is the phase of the μ-th component of m-th order originating from ν-th component of the incident field. Similarly, and $\arg(a^\nu)$ is the phase of the ν-th component of the incident field at the entrance pupil. The latter can be kept as an reference to be used if explicit phase evaluation from Eq. 3.7 is required. If we assume that the incident field is faithfully measured, for example, by a wavefront sensor, so that the vector $\boldsymbol{a}$ is known for all incident waves in the pupil, then Eq. 3.8 can be regarded as an equation with three unknowns, namely the moduli $|r_0^{\mu\nu}(\boldsymbol{k}_v^o)|$ and $|r_1^{\mu\nu}(\boldsymbol{k}_v^o - \boldsymbol{g})|$ and the phase difference $\arg r_0^{\mu\nu}(\boldsymbol{k}_v^o) - \arg r_1^{\mu\nu}(\boldsymbol{k}_v^o - \boldsymbol{g})$. Following standard algorithms of phase shifting interferometry, we require at least three scanning positions for obtaining all the unknowns in Eq. 3.8. This can be done by changing Δx and repeating the measurements. This argument can be extended

[6] This is the ratio of square roots of cosines of incidence and scattered angle, and is unity when they are equal (zeroth order).

when more orders overlap, by stating that we need at least $2N-1$ scan positions for N overlapping orders. Anyway, only the phase *difference* between overlapping reflected orders, i.e. $\arg r_0^{\mu\nu}(\boldsymbol{k}_v^o) - \arg r_1^{\mu\nu}(\boldsymbol{k}_v^o - \boldsymbol{g})$, can be calculated.

This shows why scanning is not sufficient for determining the individual phase of the orders, and to obtain this, interference with a reference wave is necessary. As a consequence there will be an unavoidable increase in the amount of data. This combined technique, which we refer to as ICFS, will contain $4V\zeta_{min}\iota_{min}$ data elements, where ι_{min} is the required number of steps of phase-shifting-interferometry and ζ_{min} is the minimum scanning positions (which may be different from ζ_{min} of CFS). Both of these are determined in the remaining part of his chapter.

Now et us assume that the reflected field $b_{\Delta x}^{\mu\nu}$ is made to interfere with another completely known reference wave a_{ref} polarized along $\boldsymbol{\mu}$, the polarization direction of the outgoing wave. The complex amplitude becomes

$$\begin{aligned} a_{ref}^{\mu} + b_{\Delta x}^{\mu\nu}(\boldsymbol{k}_v^o) &= r_0^{\mu\nu}(\boldsymbol{k}_v^o)a^{\nu}(\boldsymbol{k}_v^o) + a_{ref}^{\mu} \\ &\quad + r_1^{\mu\nu}(\boldsymbol{k}_v^o - \boldsymbol{g})a^{\nu}(\boldsymbol{k}_v^o - \boldsymbol{g})\exp(ig\Delta x). \end{aligned} \tag{3.9}$$

For simplicity, from now on let us assume that both the incident and the reference wave are perfectly planar. This does not change the general outcomes. Also, for simplicity of notation, let us drop the transverse wave vector $\boldsymbol{k}_v^o$ in $b_{\Delta x}^{\mu\nu}(\boldsymbol{k}_v^o)$ from now on. From Eq. 3.9, the interference is now a three wave one, and the intensity can be written as

$$\begin{aligned} I_{\zeta\Delta x,\iota}^{\mu\nu} &= |b_{\zeta\Delta x}^{\mu\nu} + a_{ref,\iota}^{\mu}|^2 \\ &= |b_{\zeta\Delta x}^{\mu\nu}|^2 + |a_{ref,\iota}^{\mu}|^2 \\ &\quad + 2|b_{\zeta\Delta x}^{\mu\nu}||a_{ref,\iota}^{\mu}|\cos[(\arg b_{\zeta\Delta x}^{\mu\nu} - \arg a_{ref,\iota}^{\mu})], \end{aligned} \tag{3.10}$$

where, $\arg a_{ref,\iota}^{\mu}$ is the phase of ιth step of the reference wave polarized along μ, with $\iota = (0, 1, ..., \iota_{min} - 1)$ and the scan positions are numbered by the index $\zeta = (0, 1, ..., \zeta_{min} - 1)$. Physically, $I_{\zeta\Delta x,\iota}^{\mu\nu}$ implies, following the notation for scanning and phase steps as introduced before, the intensity for the ιth phase step measured at the ζ_mth scanning position.

To understand the minimum number of frames required for one specific polarization scheme, it may be noted from Eq. 3.9 that the first and the zeroth order complex reflection amplitudes add up to the complex number $b_{\zeta\Delta x}^{\mu\nu}$ in Eq. 3.7. The latter complex number as a whole is derivable from phase-shifting-interferometry with a reference wave by taking at least 3 scanning positions ($\iota_{min} = 3$). However, to solve a system of equations as in Eq. 3.7, we need two more measurements, i.e. two scan positions ($\zeta_{min} = 2$), since this complex number contains two independent complex numbers in it, namely $r_0^{\mu\nu}(\boldsymbol{k}_v^o)$ and $r_1^{\mu\nu}(\boldsymbol{k}_v^o - \boldsymbol{g})$. Thus, the minimum number of frames required for measurement of one specific polarization scheme in ICFS is six, employing a three-step phase shifting interferometry each with two scanning positions, ($\iota_{min} = 3$; $\zeta_{min} = 2$).

This argument can easily be extended when more orders are overlapping ($F < 1$). For example, if three orders are overlapping, $b^{\mu\nu}_{\zeta\Delta x}$ will contain three independent complex numbers, and we will need nine measurements ($\iota_{min} = 3$; $\zeta_{min} = 3$). Successive overlapping orders will increase ζ_{min} by one each. An interesting remark can be made here by noting that ICFS, i.e., CFS with interference with a reference wave leads to a smaller minimum number of scanning positions than the CFS setup without interferometry with the reference wave.

Together, all the interferometric and scanning frames are considered as one set of intensity data, a scatter-interferometry super-frame can be constructed. After this super-frame is defined, standard sensitivity analysis for scatterometry (as explained already in chapter 2.3) of the model with respect to the required shape parameters can be done. Assuming a noise independent of pixel location and having a normal distribution with unit standard deviation, the 3-sigma uncertainty per pixel per unit noise standard deviation, Δa_j, for the jth shape parameter is given by Eq. 2.6

$$\Delta a_j = 3\sqrt{4V\zeta_{min}\iota_{min}C_{jj}}, \tag{3.11}$$

where the only change is the fact that compared to CFS, $4V\zeta_{min}\iota_{min}$ now stands for the number of pixels in an ICFS superframe. As per convention, we arrange the shape parameters (Fig.2.1) in one vector $\boldsymbol{a} = (a_1, a_2, a_3) = (height, swa, midcd)$ and the jth component of that vector has uncertainty Δa_j. Now we can define the coherent sensitivity gain due to interferometry, $\boldsymbol{csgi}$ as

$$csgi_j = \frac{\Delta a_{l,scatterometry\ without\ interferometry}}{\Delta a_{l,scatterometry\ with\ interferometry}}, \tag{3.12}$$

where it is assumed that for scatterometry without interferometry sufficient scanning is already done to obtain maximum possible sensitivity.

3.3. Results and discussion of Sensitivity Analysis

In this section, we consider example gratings of different pitches to evaluate the sensitivity gain and to verify the assumptions made through numerical simulations using RCWA [11, 12]. The independent variable is the overlap parameter which can be varied from $F = 1$ to some reasonable upper limit such that the case where only the zeroth order is present is also considered. In the following simulations, we set this upper limit as $F = 2.2$[7]. We set the simulation wavelength at $\lambda = 633$ nm and assume a NA of 0.9, while the pitch is kept variable. The work cycle is fixed at 0.5 so that midcd scales linearly with the pitch. In Table 3.1, we summarize the simulation parameters.

In Fig. 3.4, the results for ICFS is shown. It is seen that $\boldsymbol{cgsi} > 1$ for *all* values of overlap parameter and for *all* parameters, proving the benefits of ICFS. Depending on the specific value of the overlap parameter the gain, $\boldsymbol{cgsi}$, is seen to vary. This

[7] For $F > 2.2$, certain input-output polarization combinations start to become insensitive to grating shape variation which leads to large numerical error in finding the inverse of Hessian matrix 2.5

Table 3.1: Simulation parameters summarized

Simulation Settings			
Grating Type	Binary Symmetric, Resist (1.5) on Silicon in air		
Grating Shape	150nm (height)	90° (swa)	0.5 (midcd)
Overlap Parameter Settings	$\lambda = 633$ nm	$NA = 0.9$	variable Λ

indicates that for these given physical variables (wavelength, NA, grating materials etc.) some specific grating shapes have more sensitivities than the others. As was expected, $csgi > 1$ for all parameters even when there is only zeroth order ($F > 2$), which shows the benefits of coherence without the need of the overlapping orders, and so, without any theoretical lower bound of the value of the pitch. In practice, we expect this gain in sensitivity to gradually decrease for very small pitch, for which the information in the scattered field will be smaller than the noise level.

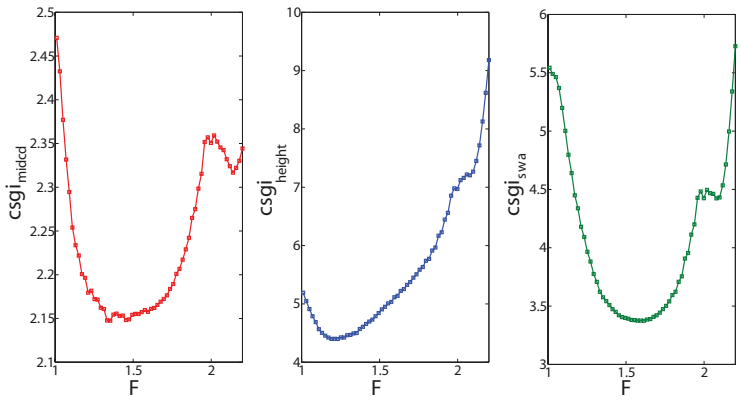

Figure 3.4: Gain in sensitivity of ICFS is compared to CFS, as $\boldsymbol{csgi}$ as a function of overlap parameter F is plotted for $midcd$ (left), $height$ (center) and swa (right) in the range $1.01 \leq F \leq 2.2$. Improvement in sensitivity is seen for all cases.

It will be interesting to make a comparison of ICFS with CGS here. As mentioned in section 3.1 and part A of Fig. 3.1, integration with interferometry can also be done for this technique (Interferometric Coherent Goniometric Scatterometry (ICGS)), and if we repeat the experiment for each of the incident waves in the NA, we can make a fair comparison with ICFS . As the scattered field of each incident plane wave will have to be interfered with the reference beam separately, this process will be very slow and have little practical importance. Nonetheless, the comparison with ICFS will show some interesting features. Since normally CGS is done for planar incidences (see Fig. 1.3 and Ref. [13]) only,a linear array along the x-axis ($\eta = 0$) will be considered for the interferometric version of both methods. This comparison is shown for $midcd$ in Fig.3.5. Here the sensitivities of ICFS is normalized with

the ICGS for two cases, no scanning ($\zeta_{min} = 1$) and with sufficient scanning[8]. For $F > 2$, we observe sensitivities of both methods are identical. To explain this, firstly we note that all calculations for ICGS requires only $\boldsymbol{R}_m^R$ mentioned in Eq. 3.6. As $F > 2$, only the zeroth order is captured ($fac = 1$ in Eq. 3.6), and, the sensitivities from both methods should be identical because the rotation matrices in (3.6) cannot add any overall gain in sensitivity. This can be used as a check for correctness in modeling both methods. For $F \leq 2$, without scan, the sensitivity of ICFS is poorer than ICGS. However, the situation changes as scanning is performed because then ICFS is seen to have more sensitivity. This seems surprising at first, as both techniques must have same physical information. The explanation for this observation can be found from the way in which this information is arranged in intensity measurements of the two cases. To explain this, we expand Eq. 3.10,

$$\begin{aligned} I^{\mu\nu}_{\Delta x,\iota}(\boldsymbol{k}_P^Q) \quad = \quad & |r_0^{\mu\nu}|^2 + |r_1^{\mu\nu}|^2 + 1 \\ & +2|r_0^{\mu\nu}|\cos[(\arg r_0^{\mu\nu} - \arg a^{\mu}_{ref,\iota})] \\ & +2|r_1^{\mu\nu}|\cos[(\arg r_1^{\mu\nu} + g\Delta x - \arg a^{\mu}_{ref,\iota})] \\ & +2|r_0^{\mu\nu}||r_1^{\mu\nu}|\cos[(\arg r_0^{\mu\nu} - \arg r_1^{\mu\nu} - g\Delta x)]. \end{aligned} \tag{3.13}$$

Here we have dropped the functional dependence of $r_0^{\mu\nu}$ and $r_1^{\mu\nu}$ on $\boldsymbol{k}_i^Q$ and $\boldsymbol{k}_Q^i - \boldsymbol{g}$, respectively, to make the equation compact assuming they are implied implicitly. If we take the derivative of Eq. 3.10 with respect to any shape parameter, a contribution of the last term is only available in ICFS. This term is independent of the phase of the reference wave. Without scanning, this term can be seen as an additional noise component with unpredictable contribution towards sensitivity, while with scanning, this gives a gain in sensitivity by adding more information. From the point of view of determination of the scattering matrices of the system, ICGS is simpler, since there is no need to retrieve overlapping orders. However, owing to the overlap, ICFS has superior sensitivity.

In Fig. 3.6 we test the remarks made after Eq. 3.10 about the values of ι_{min} and ζ_{min}. We designate our scatter-interferometry super-frame by $(\iota_{min}; \zeta_{min})$. For example, (0;4) will mean scatterometry without interferometry with 4 independent scanning position, likewise, (3;12) implies scatterometry with 3-frame Phase-Shifting-Interferometry and 12 scanning positions. If we notice the 3-sigma uncertainty in $midcd$ for two specific overlap parameters, then we can see for the specific grating with $F = 1.59$ (overlap between orders) the minimum is obtained for (3;2); (3;12) and (4;4), whereas, for the case $F = 2.08$, (only 0th order) there is no change after (3;1). Thus it is seen that when there is overlap, $(\iota_{min}; \zeta_{min}) = (3; 2)$ is sufficient and for no overlap, $(\iota_{min}; \zeta_{min}) = (3; 1)$ is sufficient[9]. If we compare the (0;4) and (3;2), we can see the increase in sensitivity due to addition of interferometry is comparatively larger for $F > 2$, about 3 times, than for $F \leq 2$ when it is about 2 times. Finally, we may note that a measurement scheme of (3;2) for

[8] As Goniometric Scatterometry has no superposition, scanning is unnecessary.
[9] To be noted, (0;4) is sufficient for CFS, while (3;0) is sufficient for ICGS.

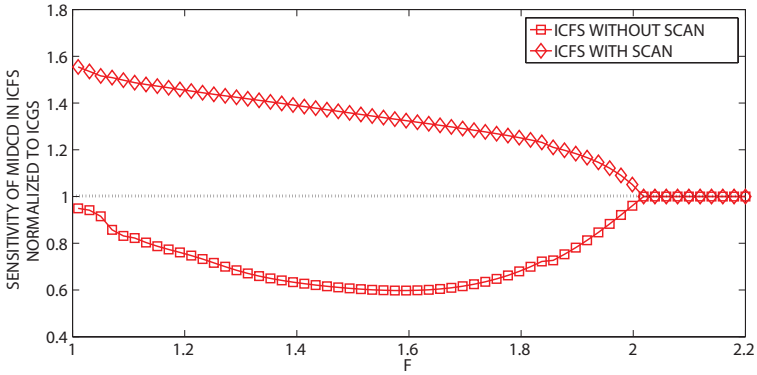

Figure 3.5: Sensitivities of ICFS is compared with ICGS. Sensitivity in ICFS for midcd is normalized with the sensitivity of ICGS and plotted as a function of the overlap parameter F for the cases when scanning is done (diamond) and not done (square). The results show that with scanning the sensitivities in ICFS becomes better when $F \leq 2$. As $F > 2$, the sensitivities of both methods are same.

$F > 2$ and (3;0) for $F \leq 2$ should provide sufficient information to obtain scattering matrices. For this reason, more intensity measurements did not lead to any gain in sensitivity. This remark supports the assumptions made after Eq. 3.10.

3.4. Sectioning in CFS and ICFS

One way to view CFS is modeling the whole process as a simultaneous incidence of a number of plane waves of different angles of incidence on the sample. It is always possible to section a specific fan of rays from the objective exit pupil, which, if properly chosen depending on the specific situation, often yields almost same sensitivity as considering the whole of the pupil. In other words, for specific nominal value of the grating, some parts of the pupil might be more sensitive than others. Identifying them will have a significant positive impact on the speed of optimization. In this section, we discuss about sectioning a part of CFS or ICFS superframe and consider that as our complete data set. We refer to this as sectioned CFS/ICFS.

In the present context, we will restrict ourselves to the simple case of planar sectioning, i.e., only the plane waves with planar incidences ($\varphi = 0$) are considered. This reduces the number of plane waves in the exit pupil by a factor of $2/\pi b$ where b is the number of samples along the radius of the pupil. To be noted, planar sectioning also allows us to avoid computationally expensive conical incidence solutions (part B of Fig. 1.3).

We consider two cases separately, where $1.01 \leq F \leq 1.9$ and $2.01 \leq F \leq 2.9$. This allows us to consider cases with and without considering bias, respectively. For each intervals, we consider 20 values. We simulate the grating with the same nominal values as in section 3.3 and table 3.1. The results in table 3.2, with pixel independent noise standard deviation of $\sigma_{noise} = 1 \times 10^{-3}$.

In table 3.2, we show the rms of the uncertainties over the full range of overlap

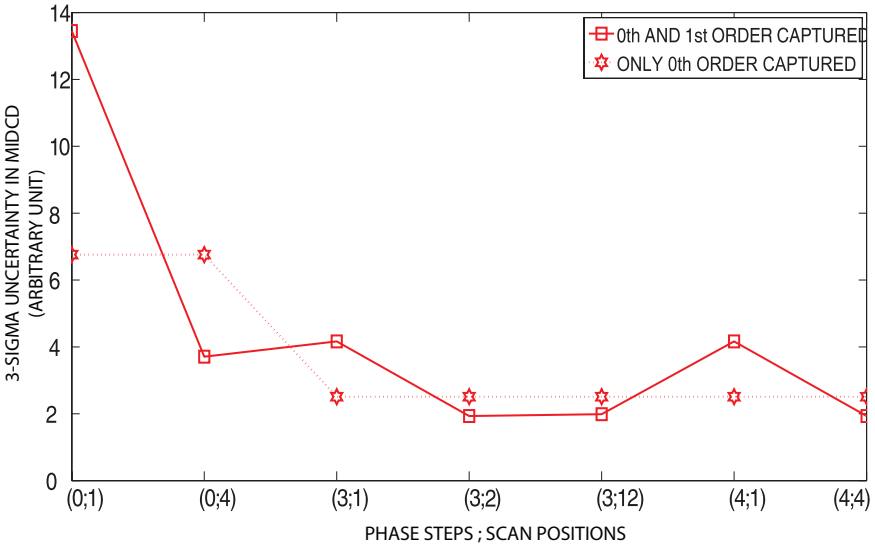

Figure 3.6: Verification of Eq. 3.10 is shown for two overlap parameters F=1.59 (square with solid line), when the 0th and the 1st orders are present, and, for F=2.08 (star with broken line), when only the 0th order is present. The abscissa denotes different cases of interference and scanning as ordered pair, where the first number is the number of phase steps in interferometry and the second is number of scanning positions. The 'saturation' of sensitivity shows no more sensitivity gain beyond $(3;2)$ for both gratings, agreeing with the predictions made after Eq. 3.10

Table 3.2: rms over F of parameter Uncertainties per unit pixel for noise standard deviation of $\sigma_{noise} = 1 \times 10^{-3}$

	ICFS	Sectioned ICFS
swa (degree)	2.646	2.181
midcd (nm)	2.406	1.985
height (nm)	0.864	0.763

parameter F. It can be readily seen that the average uncertainties remain in the same range for all parameters, and for $midcd$ and $height$, it is actually better in case of sectioned ICFS! This can appear to be strange at first thought, since it may seem that the sensitivity of a part of the data cannot be better than the full set. However, if we consider this is rms over F for average uncertainties *per unit pixel*, we can think of a situation where the average uncertainties per pixel along the planar section can be lower than average uncertainties of the whole far-field. Nonetheless, this is a special case which, according to our experience, is normally valid for binary gratings and planar diffraction.

The gain in speed of simulating one complete set of data (one superframe) of ICFS and sectioned ICFS is compared in Fig. 3.7. As was mentioned before, planar sectioning also helps us to avoid computationally expensive conical incident solutions, and so, the gain in computational time as shown here might be slightly

overestimated for a general case. Nonetheless, unless the sectioned area is large, there will always be significant gain in computational time for sectioned ICFS/CFS, which will be more evident when the far-field has to be generated iteratively several times in an optimization routine.

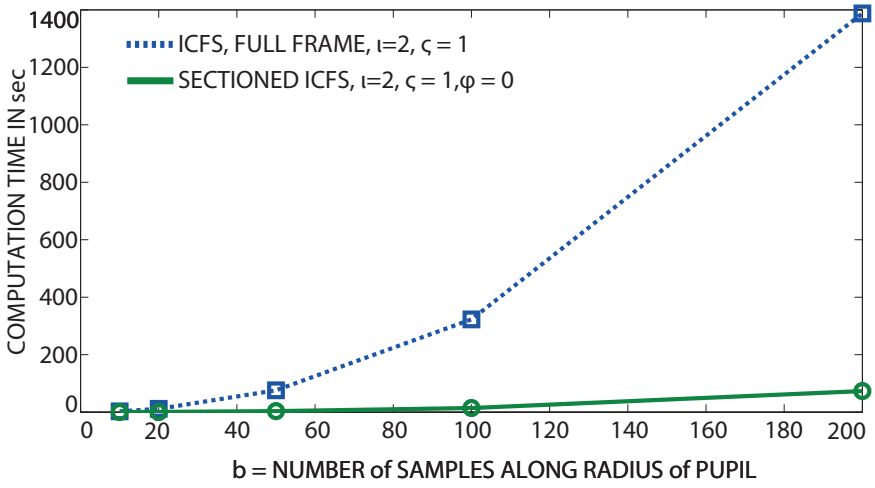

Figure 3.7: The computation time in sec for generation of each superframe for ICFS (blue, broken line) and sectioned ICFS (green, continuous line) plotted against b number of samples along radius of pupil. The gain in speed can be clearly seen. However, the speed gain is not exactly proportional to $2/\pi b$, because the conical diffraction takes longer to converge than planar.

3.5. Conclusion

In this chapter we showed how Coherent Fourier Scatterometry for CD metrology can benefit from its integration with phase shifting interferometry to improve the sensitivity. In section 3.2 we developed the model we will be using and in section 3.3 we presented the discussion. The results show an improvement in sensitivity even for small pitch such that $F > 2$. We also made a comparison with an interferometric version of goniometric scatterometry, ICGS, and showed that ICFS has some advantage when there is overlap between orders $F \leq 2$. Section 3.4 followed where we presented a sectioned version of ICFS, which can be implemented in situations where fast convergence is required.

It was pointed out ([14]) that one of the advantages of CFS compared to other angular scatterometry methods was the fact that a number of plane waves from different directions can be incident simultaneously, creating superposition and consequent enhancements of sensitivity. We showed how this fact can be further utilized to obtain the scattering matrix for all those incident waves. Moreover, unless the pitch was sufficiently large, the overlap between orders does not occur and CFS did not have any practical advantage in terms of sensitivity compared to Incoherent Fourier Scatterometry. With ICFS, improvement of sensitivity for these cases is also shown. In a comparison with CGS, we showed that even though these two

systems contain same physical information about the sample, with scanning, ICFS shows superior sensitivity. This is desirable for fast convergence of any optimization algorithm, a fact which is very important for industrial applications.

We end this chapter, and also the part of the thesis regarding CFS for CD metrology, with a summarizing picture (Fig. 3.8) showing the evaluation of Fourier scatterometry for CD metrology.

References

[1] S. Roy, N. Kumar, S. F. Pereira, and H. P. Urbach, *Interferometric coherent fourier scatterometry: a method for obtaining high sensitivity in the optical inverse-grating problem,* Journal of Optics **15**, 075707 (2013).

[2] S. Roy, N. Kumar, S. F. Pereira, and H. P. Urbach, *Fringe 2013*, edited by W. Osten (Springer Berlin Heidelberg, 2014) pp. 43–48.

[3] T. Young, *The Bakerian Lecture: On the theory of light and colours,* Philosophical Transactions of the Royal Society of London **92**, 12 (1802).

[4] N. Kumar, O. El Gawhary, S. Roy, S. F. Pereira, and H. P. Urbach, *Phase retrieval between overlapping orders in coherent fourier scatterometry using scanning,* Journal of the European Optical Society - Rapid publications **8** (2013).

[5] N. Kumar, L. Cisotto, S. Roy, G. Ramanandan, S. F. Pereira, and H. P. Urbach, *Determination of the full scattering matrix using coherent fourier scatterometry,* (2016), submitted.

[6] D. Malacara, M. Servin, and Z. Malacara, *Interferogram Analysis for Optical Testing* (CRC Press, 2005) chapter 7.

[7] V. Paz, S. Peterhansel, K. Frenner, and W. Osten, *Solving the inverse grating problem by white light interference fourier scatterometry,* Light Sci Appl **1** (2012).

[8] R. Rumpf, *Improved formulation of scattering matrices for semi-analytical methods that is consistent with convention,* Progress In Electromagnetics Research B **35**, 241 (2011).

[9] D. A. Bykov and L. L. Doskolovich, *Numerical methods for calculating poles of the scattering matrix with applications in grating theory,* J. Lightwave Technol. **31**, 793 (2013).

[10] L. Novotny and B. Hecht, *Principles of Nano-Optics*, 1st ed. (Cambridge University Press) pp. 56–60.

[11] M. G. Moharam, T. K. Gaylord, D. A. Pommet, and E. B. Grann, *Stable implementation of the rigorous coupled-wave analysis for surface-relief gratings: enhanced transmittance matrix approach,* J. Opt. Soc. Am. A **12**, 1077 (1995).

[12] M. van Kraaij and J. Maubach, *A more efficient rigorous coupled-wave analysis algorithm, Progress in Industrial Mathematics at ECMI 2004*, Mathematics in Industry, **8**, 164 (2006).

[13] M. Wurm, F. Pilarski, and B. Bodermann, *A new flexible scatterometer for critical dimension metrology,* Review of Scientific Instruments **81**, 023701 (2010).

[14] O. El Gawhary, N. Kumar, S. F. Pereira, W. M.J. Coene, and H. P. Urbach, *Performance analysis of coherent optical scatterometry,* Applied Physics B **105**, 775 (2011).

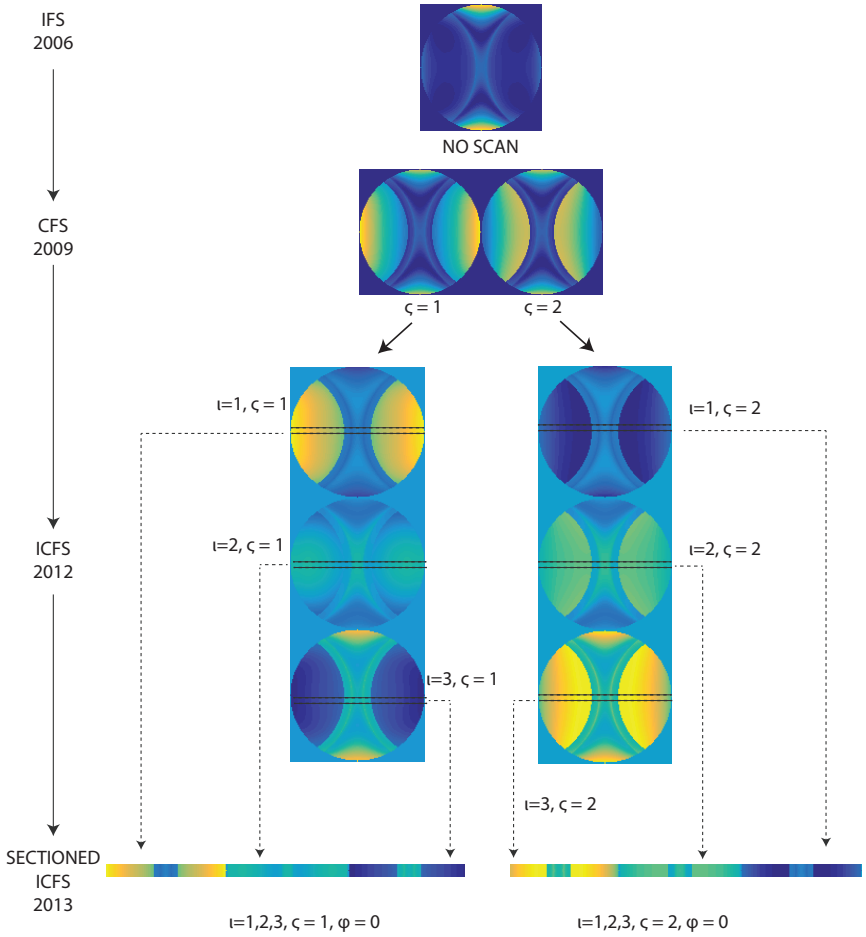

Figure 3.8: The evolution of Coherent Fourier Scatterometry for CD metrology. IFS predates this thesis, while CFS was conceived before this thesis as well. The benefits of CFS, and the concepts of ICFS and sectioned CFS have been discussed here.

Intermission

So far we have shown how CFS can be used to improve CD metrology by offering higher sensitivities for parameter reconstruction. The reason of the gain in sensitivity was mainly due to the fact of using the coherent illumination which contributed to implicit phase information. Even more sensitivity gain can be obtained by combining interferometry with scatterometry. Finally we showed that the sectioned Fourier scatterometry is suitable for fast optimization requirements.

After this intermission, we start to discuss the problem of particle detection with CFS. For particle detection, CFS is a relatively new technique, and so, we worked on several areas of the setup to make it more suitable for that task ; namely the detection part, the illumination part and also the sample, all of which will be presented in the following chapters. A common question is the benefit of coherence for CFS applied to particle detection. Initially we would have answered this question by saying that coherent spot is smaller than incoherent spot, and so, will offer higher sensitivity. Later on, we found out more benefits of coherence, which plays a key role to justify the modifications in the illumination part. We also found that top-coating the substrate with a very thin layer of certain materials can dramatically increase the detection sensitivity of CFS.

4

CFS for Particle Detection : Enhancement by Detector Arrangement

Parts of this chapter have been published in Opt. Exp. **11**, 22 (2014) [1].

As we have already mentioned in the introduction part, inspection tools for nano-particle contamination on a planar substrate surface is a critical problem in micro-electronics. Solutions for this inspection problem employing imaging techniques [2] or confocal imaging technology [3], mainly due to their simplicity and robustness, are not suitable due to diffraction limitation. The other class of non-imaging techniques, based on scattering, are presently expensive, slow and in most cases require large incident power. In this chapter we show that CFS is capable of low power detection of particles down to 100 nm in size, using a illumination wavelength of 405 nm. In this chapter we specifically concentrate on how to make the CFS particle scanning system fast and accurate by modifying the detection system.

4.1. Introduction

The problem of detecting isolated nano-particles [4] or small damages on a surface is an important requirement arising in many practical situations. One example is semiconductor manufacturing process, where silicon wafers need to be cleaned thoroughly to eliminate the 'killer particles' [5] prior to further processing. With the advent of newer substrates for flexible electronics devices based on polymer substrates [6, 7], having completely different surface topology than silicon, this problem is getting more diversified. At the same time, with emerging processes requiring more stringent cleaning requirement, for example extreme ultra violet lithography, [8, 9], this problem is getting more challenging as well. Often, besides detection, locating the detected particles and classifying them according to their sizes without carrying out any additional measurement is an additional requirement. This is true in many practical situations, for example, engineering of optical nano-circuits [10].

With the popular and very successful way of particle detection using scattering based dark-field techniques [11, 12], it is difficult to detect particle on substrates which can be damaged in high power illumination. We can have a brief look at the system described in [11] which follows from the basic setup for scattering based optical inspection tool. In that system, a laser beam is focused onto the sample from a high angle of incidence, being detected after reflection. The drawbacks include a complex experimental arrangement, slower and expensive operation and small room for further modification. The state of the art commercial scanners, that employs this technique in a dual-laser variation (for example KLA-Tencor Candela series), has reached sensitivities of about 60-80 nm (with dual wavelength illumination of 405 and 350 nm), whereas more specialized ones, which uses shorter wavelengths, are able to detect about 40 nm particles [5]. Recently a detection sensitivity down to 20 nm [13, 14] has also been reported. Their success in this problem is largely due to the high SNR that they can offer, which in turn, is because of the separation of specular reflection and scattered radiation. The basic principle of dark-field particle detection is shown in Fig 4.1.

However, the high SNR of these techniques comes at a price. For the same amount of incident radiation on the scatterer, the energy of the scattered light varies to the sixth power of the scatterer dimension [15], and thus to have sufficient SNR, the incident radiation must be very dense in energy. Thus, the power requirements

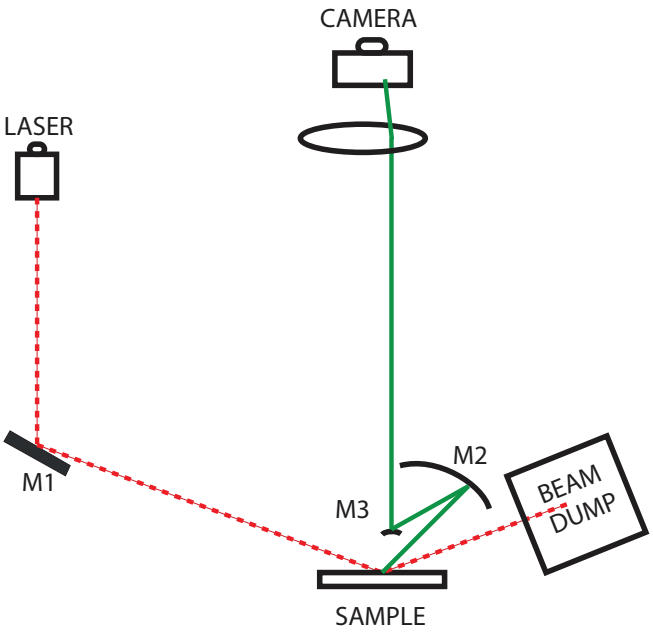

Figure 4.1: Schematics of a dark field particle detection technique. The excitation beam path is shown in thick dashed line and the scattered beam path is shown in thin continuous line. The direct reflected beam is dumped, while the scattered beam is steered using mirrors M2 and M3; and imaged using lens L1. There can be several pairs of incident-outgoing beams.

of the dark field particle detectors are significantly higher. For example, the dark field techniques typically require hundreds of milliwatt for particle detection in range of 100 nm [12], which is still usable for substrates like silicon wafers but can be destructive for polymer substrates [16]. Dark field detection unavoidably implies that a large amount of power will not be delivered to the scattering particle but to the substrate, which is not only waste of energy but also a possible source of inadvertent damage to the substrate due to prolonged heating.

On the other hand, in CFS, a bright field technique, a large fraction of incident power can be delivered to the scatterer, however, the SNR is poor since the specular reflection and the scattered light travel along the same path and cannot be separated. To increase the SNR, one must find a method to identify their presence separately. This can be done by using a scanning-based detection system after realizing that the specular reflection is invariant with scanning, whereas, the scattered radiation depends on the relative position of the optical beam and the scatterer. Using this idea, in this chapter we evaluate the performance of CFS for particle detection relying on far field asymmetry that occurs when the particle is scanned. CFS has the structural benefit of being simpler to configure than other scattering based techniques, as for example the one described by Okamoto et. al in Ref. [11]. The complexity of the experimental arrangement is greatly reduced by employing one single objective to focus and collect the reflected light where high angles of incidence are achieved by using objective with high numerical apertures. An additional benefit is that the coherent focused spot has a very small area so that the local departure from flatness of the substrate does not play a large role.

To summarize, in this chapter we present the performance of CFS for detecting

isolated elements as small as 100 nm and also establish the technique of detection of a particle based on asymmetry in the far-field. Our experimental setup utilizes a coherent source of 405 nm with an objective of numerical aperture (NA) of 0.9, which implies that the samples contain particles smaller than conventional diffraction limit associated with the confocal microscopy, namely $\lambda/4$[1]. We also show how the approximate location and size of the nano-particle, without making additional measurements, can also be determined by CFS. The versatility and possible ways to increase sensitivity are discussed in detail.

This chapter is organized as follows: in the next section, we briefly describe the experimental setup and the samples examined, including their preparation procedure. In section 4.3, we first consider the electromagnetic problem of interaction of a spherical particle on a flat isotropic substrate illuminated by a focused field of coherent illumination and solve the problem numerically. This helps us to do a feasibility study to check whether a CFS system with given parameters is able to detect contaminating particles of a given size, and if that is the case, to determine the sensitivity. After this, a direct comparison between theory and experiment is provided. Finally we discuss methods to increase the SNR for small particles. The conclusions of this work are given in Section 4.4.

4.2. Experimental setup and preparation of the samples

4.2.1. Setup

In Fig. 4.2, the experimental setup of CFS is shown. [17, 18]. This is essentially a commercial scanning near-field optical microscope (Witec Alpha 300S), largely modified to operate simultaneously as a CFS and conventional microscope. The advantage of having a conventional microscope is to have the possibility of visually confirming that the signal generated by CFS is coming from the contaminating particles and not from something else. Naturally, it works only for particles larger than 200 nm for which it is possible to directly image them. Moreover, the conventional microscope helps to set up the CFS by imaging the sample plane, which, if the CFS is set up correctly, should contain the focused spot. This plane is imaged in CAMERA1. The conventional microscope part uses a white light source (COL2) whereas the CFS part uses a diode laser operating at 405 nm. The laser beam is coupled into a single mode fiber and redirected to the main part of the setup through the collimator COL1. The light from the COL1 is made linearly polarized (POL1) before it passes through the beam-splitter (BS1) and focused by the objective (OBJ). Other elements can be easily inserted along the light path in order to obtain any desired input polarization other than linear. This is how we have implemented radially polarized incident field, a description of which is given in next chapter. The objective position in the axial z-direction can be adjusted by a stepper motor to aid focusing, up to a precision of 50 nm[2], till the maximum SNR is obtained. The sample

[1] Later we were able to detect $\lambda/6$ particles (see section 7.4), and the detection sensitivity can be further improved, so this is not the detection limit.

[2] In the experiments later we have used a better stepper motor with focusing precision of 10 nm.

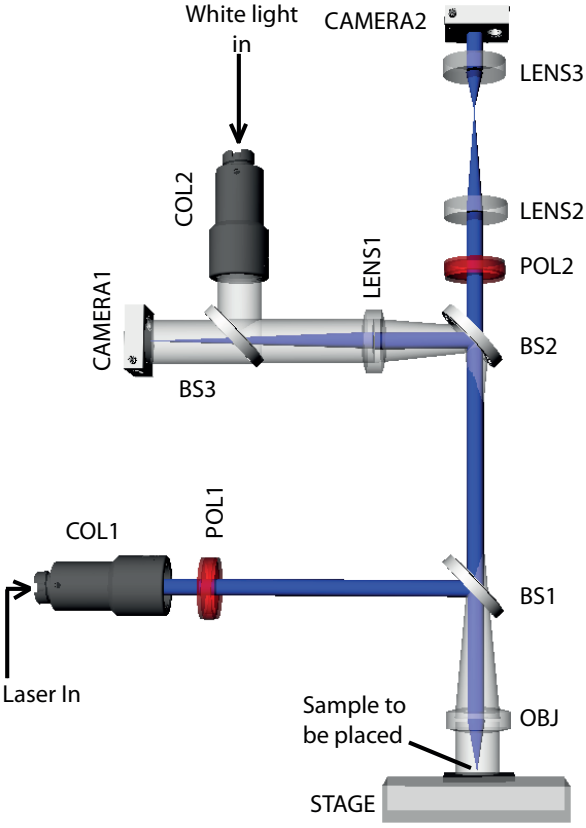

Figure 4.2: The experimental setup of CFS. Adding to the schematics of Fig. 1.1, we present here a more detailed configuration, together with the white-light microscope, used for observing the sample. The experimental results in this chapter here are obtained from this setup. In later chapters, small modifications are sometimes made of this setup (for example, to incorporate specific incident field polarization), but the basic CFS experimental principle stays same throughout the thesis.

is placed on the scanning table (STAGE) driven by a piezo-transducer which can move the sample in raster mode to perform scanning of the area of interest. The reflected field from the sample is captured by OBJ, and the output polarization is set by polarizer (POL2). A telescopic arrangement is formed by LENS2 and LENS3 to fit the reflected beam into the camera aperture (CAMERA2). The set-up is kept in a temperature controlled clean room.

4.2.2. Samples

We will consider two types of samples in this chapter. The first type consists of polystyrene latex (PSL) nano-spheres of diameters of 400 nm, 200 nm and 100 nm deposited on a polished silicon wafer with rms roughness < 3nm [19, 20] in the shape of a disc of diameter 2.54 cm, with densities of approximately 1300/sq.mm, 4100/sq.mm and 26000/sq.mm, respectively. To deposit the particles, mono-disperse PSL colloidal suspension (stabilized by ultra-sonic treatment and shaking) was dispersed by spin coating on the substrate, which was cleaned with UV-ozone treatment. The second type of sample is an organic light emitting diode (OLED) deposited on a square glass substrate of size 25 mm. In those sam-

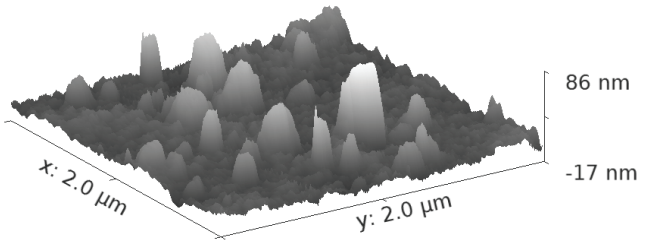

Figure 4.3: The AFM scan of the bare OLED sample. Water ingress into the pinholes in the cathode caused by the presence of particles, leads to an oxidation of the Al at the cathode-LEP interface. At these locations the electron injection is blocked, resulting in a local absence of emission, visible as a so-called black spot, or pinhole (see also part A of 4.10). The rms roughness is about 9.5 nm for an area of roughly the spot size. Due to numerous defects, the rms roughness rapidly increases for larger areas, for example, it is about 30 nm for an area of 20 μm square. This typically large roughness is probably due to degradation of cathode, where due to gas formation underneath the cathode when water reacts with aluminum, roughness increases.

ples, firstly poly-3,4-ethylenedioxythiophene (PEDOT): poly-styrenesulfonate (PSS) was spin-coated on top of ITO on a glass substrate to fabricate the anode. The light-emitting polymer (LEP) was spin-coated from toluene on top of the PEDOT:PSS. At the last stage a Ba-Al cathode was fabricated by thermally evaporating 5 nm Ba and 100 nm Al through a shadow mask [21]. An atomic force microscope (AFM) scan of the sample surface is shown in Fig. 4.3. It shows that the surface is damaged at several locations in form of pinholes, which acts as the objects for detection for this sample. Between these two classes of samples, the samples with nano-spheres are suitable for determination of the limit of sensitivity of CFS for isolated particles, while the OLED samples are used to verify whether CFS can be used to distinguish the difference between defects of different sizes on a sample with non-negligible surface roughness.

4.3. Results of Implementation

4.3.1. The Numerical Model

The electromagnetic problem of the interaction of a spherical particle on a plane surface with an incident plane wave is interesting from a theoretical point of view and has been studied by many authors in detail [22, 23]. A detailed study on numerical methods targeted especially for this problem can be found in [24]. For our simulations we have used rigorous three dimensional finite elements method (3D-FEM) [25]. To mimic the experimental conditions, we consider an objective lens with numerical aperture NA=0.9 focusing a plane wave of wavelength of 405 nm. In the FEM simulation environment (section 1.3), the PSL particle (refractive index = 1.58) is placed on a silicon wafer substrate of index $5.42 + 0.33i$ [26] in air. The structure of the simulation model, already mentioned in chapter 1.3 is also shown in detail here in Fig. 4.4. The permittivity function is summarized by

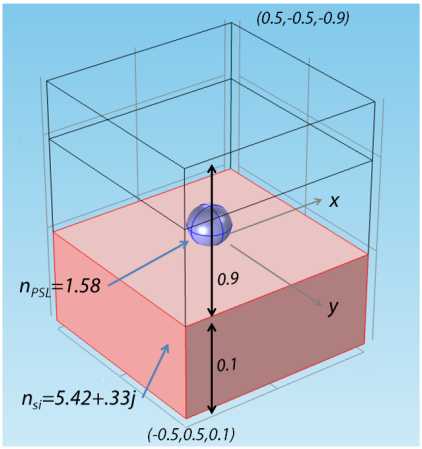

Figure 4.4: The numerical modeling of the problem. The simulation scheme is a cube of 1 μm enclosed by a perfect matched layer boundary. All numbers are in μm. Co-ordinate system is in accordance part B of Fig. 1.1. The co-ordinates of two diagonally opposite point are given. The air-silicon interface, containing the geometric focus, lies at $z = 0$ where the z axis (not shown) is the instrument's optical axis, with positive z downwards an attached to the spot. The incident wave is a beam focused at origin with the numerical aperture of 0.9, divided in to 10^4 incident angles.

$$\begin{aligned}\epsilon(x,y,z) &= 1 \text{ if } z \leq 0 \text{ and } x^2+y^2+(z-D/2)^2 > 0\\ &= (1.58)^2 \text{ if } z \leq 0 \text{ and } x^2+y^2+(z-D/2)^2 \leq 0\\ &= (5.42+0.33i)^2 \text{ if } z > 0\end{aligned} \tag{4.1}$$

where D is the diameter of the particle.

Linear polarizers are used in the incident and scattered field path (POL1 and POL2 in Fig. 4.2)[3]. To obtain the detection signal, at first the normalized power through the pupil is calculated. For a specific polarization scheme, we define the normalized power as the power in the pupil for each frame obtained during scanning divided by the power in the pupil of a reference frame (the frame in which the particle is sufficiently far from the focused spot to have detectable influence in the scattered field). This normalization procedure helps us to plot results for different samples in the same scale, and also to decrease the effects due to imperfection in optical elements. After the normalization, values that differ from unity indicate the presence of the particle. Mathematically, it can be defined as,

$$\text{Normalized power} = \frac{\sum_{v_1=1}^{\sqrt{V}}\sum_{v_2=1}^{\sqrt{V}} I_{v_1,v_2}}{\sum_{v_1=1}^{\sqrt{V}}\sum_{v_2=1}^{\sqrt{V}} I^{ref}_{v_1,v_2}}. \tag{4.2}$$

[3]It is possible to select specific combination of POL1 and POL2 to obtain sufficient information to obtain the polarization ellipse for each pixel in CAMERA2. However, measuring all these polarization schemes [27], which should improve the sensitivity, is more complex to implement and can be investigated if the linear polarization schemes would not generate sufficient sensitivity.

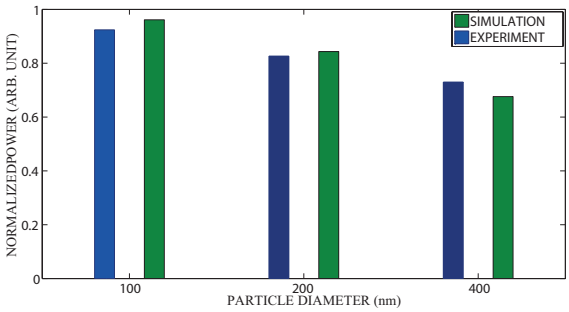

Figure 4.5: The simulated and measured normalized power for particles with varying diameters. The particles are inside the focused spot. Any deviation from unity indicates that the particle can be detected.

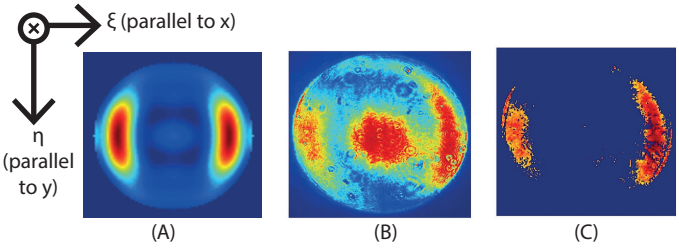

Figure 4.6: Comparison of simulated and measured far field distribution of a single 100nm particle under the focused spot, using the parallel LP-LP mode. The transverse axis used in the far field is parallel to the one defined in Fig. 1.1. (A) The simulation result, (B) experimental data without pixel by pixel normalization and (C) experimental result normalized by the reference frame. The presence of large power along the edges of the pupil in the direction of polarization is the main indication for presence of particle. All images are color-scaled similarly, so that same color implies same relative intensity.

Here, I_{v_1,v_2} is the scattered intensity at the (v_1, v_2)th pixel and $I^{ref}_{v_1,v_2}$ is the same for the reference frame. $\sqrt{V}$ is the total number of pixels in one side of the square pupil frame (with a total of V pixels) and is equal to 100 for the simulation and 572 for CAMERA2. In the way normalized power is defined, it will be finite even if the power in some pixels of reference frame is very small. The normalized power is generally smaller than unity (as the light is scattered out) for linear polarized (LP) incident light with the second polarizer parallel to it at the detection path (hereafter called parallel LP-LP, both polarized along x) and larger than unity for crossed LP-LP (second polarizer POL2 orthogonal to the first polarizer POL1, or, in our old polarization scheme, xy or yx)[4]. The primary feasibility study, for parallel LP-LP, is shown in Fig. 4.5 along with the experimental results. The sample with PSL particles on silicon wafer was used. From these results, detection seems feasible, though with a low SNR for particle size up to 100 nm.

[4]It is irrelevant for particle detection to distinguish between polarization x and y.

4.3.2. Experimental Results

As mentioned before, we consider primarily the parallel LP-LP case, with the particle positioned underneath the center of the focused spot. The simulated far field with normalized intensity (with reference) is shown in part A of Fig 4.6. The corresponding experimental result for the raw data and the data normalized with the reference intensity pattern are shown in the part B and part C of the same figure, respectively. To be noted, for this visual comparison the normalization was done pixel by pixel excluding those pixels for which reference intensity pattern had nearly zero intensity (and *not* normalized by power). A similar intensity distribution in the pupil can be noticed for the simulation and raw data. An even better agreement is obtained when the central bright spot is eliminated by normalization (see part C of Fig. 4.6). This central bright spot comes from the internal reflection between the optical components. There is a small asymmetry in the experimental data, likely caused by a small misalignment between the center of the spot and the center of the sphere, which is assumed to be zero in simulation. Nonetheless, both simulation and experiment are consistent with each other, validating thus the numerical model for describing the phenomena.

We now consider a raster scanning of a given sample. The normalized power is plotted as function of the scan distance in one direction. The starting position for each scan line is taken as the reference intensity pattern for that line. The scheme of the raster scanning for 100 nm particle is shown in part A of Fig. 4.7. Forward scans were used to capture the data frames. The re-initialization to the next line consists of a backward movement to the initial position followed by a downward cruise to the next line. During this time, no frames are captured. In part B of Fig 4.7 the detected signal of each particle is shown. The abscissa shows the shift from the initial scan position, in μm. Starting from a position far from the sphere (normalized power equal to unity), one can immediately notice a dip in the signal for light out-scattering due to the presence of the particle. The amplitude is larger for the 400nm particles and diminishes as the size of the illuminated object diminishes. For the 100 nm particle size, for the scan line with maximum modulation at $y = 100$ nm, the peak is less than 5%, but still distinguishable from the background noise. These results ultimately indicate that a simple integration method can result in the detection of particles as small as 100 nm, a function that can be readily performed by a single photo-detector, rather than a camera. We will now proceed by showing methods to enhance the SNR of the detected signal of 100 nm particles by using some modification in the detection mechanism.

4.3.3. Enhancement of the SNR for 100 nm particle

Blockage of inner part of the pupil

Although all particles considered have been detected by the CFS, one can clearly see a low SNR for the 100nm was obtained. Low SNR was expected in a bright field scheme, however, it is possible to enhance the SNR significantly. Because the scattering varies by the sixth power of the diameter [28], the scattering from 100 nm particle is about 0.02% of that from a 400 nm particle. Therefore, it is desirable to have a method to enhance the readout signal of small particles.

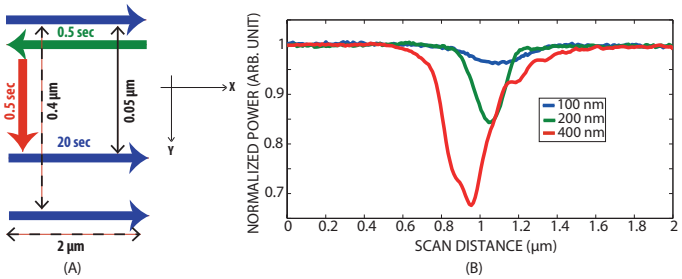

Figure 4.7: Detection of particle contamination with CFS. (A) The scheme of the raster scanning method employed. Each scan line (blue) of 2 μm takes 20 seconds and generates 200 frames. Re-initialization to next line takes 1 sec, with backward movement (green) and a downward cruise (red), generating 10 frames that are not captured by the camera. The total scan area, for this case, is 2 μm by 0.4 μm. This scheme is used for smaller particles, while, for for larger particles the shift between two lines is increased, resulting in larger scan area. (B) Normalized power against shift from initial scan position (scan distance, in μm) for particles of 400 nm (red), 200 nm (green) and 100 nm (blue). Signals with large SNR are generated by the larger particles. The bottom of the dip coincides with the center of the nano-sphere. Those frames were considered to generate the experimental data points in Fig.4.5.

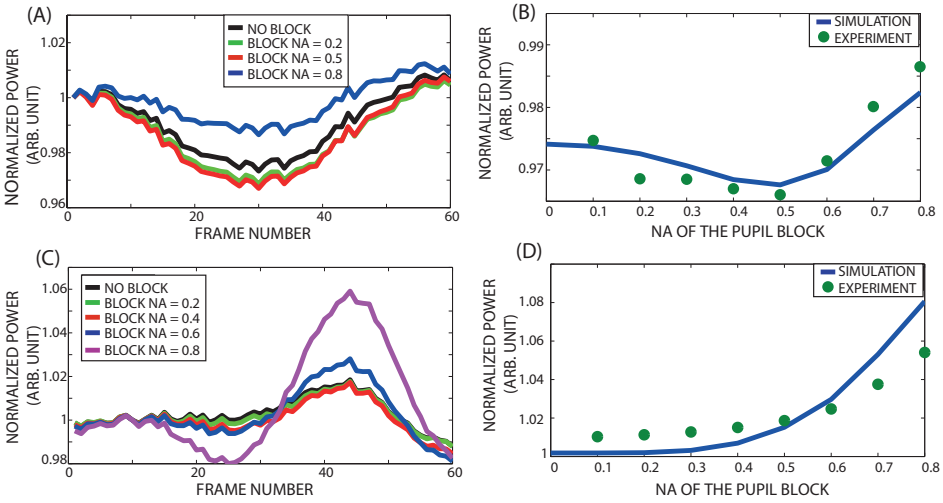

Figure 4.8: Detection signal of 100 nm PSL sphere with different amount of blocked NA from the center.(A) The improvement of the signal for 100 nm particle with different amount of blocking in the pupil is shown for parallel LP-LP scheme. (B) The comparison of the theoretical and practical data for parallel LP-LP. The optimum amount of blocking is found to about $NA = 0.5$ for this case. (C) shows the results for crossed LP-LP scheme. The blocking improves the SNR monotonically for this case. (D) comparison between simulation and experiment for case (C).

Since one would expect that the field at large angles will be more influenced by the particle than field at the smaller angles, the SNR of the readout signal can be enhanced if only the outer parts of the far-field distribution are integrated. Furthermore, spurious reflections from the optical elements that occur mostly near the central part of the pupil would be eliminated, increasing thus the SNR. We will now apply this concept to experimentally evaluate whether the SNR can indeed be improved. In part A of Fig. 4.8, the normalized power for the best scan line is plotted as function of the scan distance for different blockages of the inner part of the pupil. The results indicate an optimal improvement in the signal for the case of blocking NA=0.5 for this special case. This result is supported from the simulation results, as shown in part B of Fig. 4.8, where the trend predicted by simulation is approximately followed by the practical data. Another interesting result arises from the crossed LP-LP case. If there is no particle underneath the focused spot, a darker background is seen in the detector. However, the total power through the pupil was still finite. Whenever the particle is illuminated, the scattered field introduced by the particle becomes visible in the far-field as more light is scattered in the pupil. As a result, a larger peak-to-peak readout signal is obtained, as seen in part C of Fig. 4.8 for the best scan line. This is different than the standard dark field systems, since for a crossed LP-LP scheme, only the light whose polarization is changed by the particle is detected. The simulated and experimental results are compared in part D of Fig. 4.8.

The asymmetry in the far field

Up to now we have integrated the output signal either over the entire pupil or in the outer parts of it. A third type of integration can be done using differential or quadrant detection. The motivation for quadrant detection comes from the fact that any loss of symmetry in the far field [27] caused by scanning the particle could be immediately observed in the output signal. Therefore, by dividing the pupil into quadrants of equal area and calculating the asymmetry of power distribution between them, thereby simulating a quadrant detector (QD), there is a possibility of achieving better SNR. To implement this permanently, one can replace CAMERA2 with a quadrant detector.

In part A of Fig. 4.9, the schematics of the QD is shown. The results of this analysis for a 100 nm particle with parallel LP-LP scheme, normalized by the simulated QD signals from the first frame of the scan line, is shown in part B of Fig. 4.9 after applying a pupil blocking of $NA = 0.5$ from center. The blue line shows the detection based on normalized power, similar to part A of Fig. 4.8, while the green lines show the signal obtained from approximate QD. The dashed green line, designated as LR signal hereafter, shows the difference in power between left and right part of the approximate QD, while the dotted green line, the TB signal, shows the same for top and bottom quadrant. The solid green line is the average of the maximum and minimum signal from LR, and can be considered as zero line (ZL). Mathematically, the QD signals are evaluated as

$$LR = \frac{\sum_{v_1=1}^{\sqrt{V}/2}\sum_{v_2=1}^{\sqrt{V}} I_{v_2,v_1} - \sum_{v_2=\sqrt{V}/2+1}^{\sqrt{V}}\sum_{v_2=1}^{\sqrt{V}} I_{v_1,v_2}}{max\left|\sum_{v_1=1}^{\sqrt{V}/2}\sum_{v_2=1}^{\sqrt{V}} I_{v_1,v_2} - \sum_{v_1=\sqrt{V}/2+1}^{\sqrt{V}}\sum_{v_1=1}^{\sqrt{V}} I_{v_1,v_2}\right|}, \tag{4.3}$$

where, to eliminate the experimental misalignment and incident beam asymmetry, LR signal was set to zero for the first frame (the reference). Similarly TB signal was evaluated.

There are few interesting things to note here. Firstly, improvement of SNR by almost twice of an order is observed (the scale for QD signal is 20 times as large as the scale of normalized power), especially in LR, supporting the practicality of using asymmetry in field distribution for particle detection. Secondly, the fact that the particle has been approached more from left to right than from top to bottom, evident from the signal amplitude, gives an indication of the position of the particle from the initial scanning position. Thirdly, the approximate center of the particle can be found as the point of interaction of the ZL with LR signal. ZL corresponds to the case when the field has very small asymmetry, which happens when the spot is far from the particle or when the particle is best aligned with the z-axis or the optical axis. If the illumination was ideally planar and the reference frame was captured when the spot is infinitely far away from the particle, ZL should pass through zero. In practice, small field asymmetry is always present in the reference which shifts ZL slightly away from zero. Calculation of the approximate position of the particle can be done from the intersection of this 'practical zero line' ZL and the signal. Moreover, a scan through the center of the particle TB signal should also pass through this point and this should also correspond to the minimum of the normalized power. Another way to look at this is by assuming that the LR or TB signal are essentially derivatives of the of the normalized power, so they reaches zero when the normalized signal is at its minima.

These results are seen in part B of Fig. 4.9, for the best scan line at $y = 100$ nm, where the maximum SNR was achieved previously (refer to Fig. 4.8). In part C of Fig. 4.9, the fall of SNR is shown as the scanning spot moves further away from the center of the particle. However, detectable signal still exists for a scan at $y = 300$ nm, implying an area of diameter 200 nm is influenced by the presence of the particle. In the part D of the same figure, the position of the particle, its 'sphere of influence', and the scan lines are shown schematically in the scan area.

4.3.4. Samples with large roughness and size classification

In order to verify whether the CFS system can differentiate between particle sizes, and also, whether it can work on a surface with substantial roughness, the OLED sample is tested. The OLED sample contains defects with the shape of pinholes of various sizes on it. Part A of Fig. 4.10 is an image of the surface of the OLED, where two pinholes in close vicinity but of different sizes are marked out. In Part B

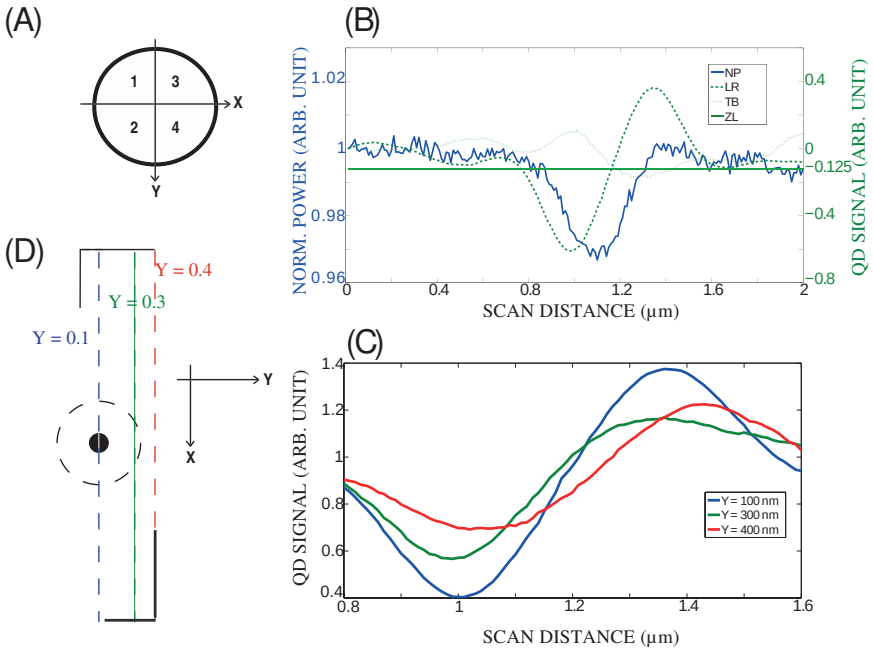

Figure 4.9: Application of QD approximation on the data obtained for 100 nm particle (sub-figures are numbered clockwise). (A) The quadrant detector approximation : LR refers to the LR signal which is the difference between the left and right part of the pupil ((1+2)-(3+4)). Similarly, the TB refers to the TB signal between the top (1+3) and bottom part (2+4). (B) For the best scan line at $y = 100$ nm, the normalized power analysis (similar to Fig. 4.8) is shown in blue, while different cases of quadrant detector approximation are shown in green. The schematic QD is shown in top left. The scale for QD signal is 20 times the signal from normalized power analysis. The fact that LR signal is more sensitive than TB signal indicates that when the scanning was done, the particle was approached by moving from left to right. (C) The decrease of SNR as the spot moves away from the particle in Y-direction. The blue line is the scan at $y = 100$ nm, green at $y = 300$ nm and red at $y = 400$ nm, relative to scan origin. It may be seen that the particle can be detected at a distance of about 200 nm away on each side of the particle. Assuming the scan line with the maximum SNR is closest to the particle center, approximate location of the particle in the scan area, along with the area over which it can be detected (dashed line), is shown in (D). In this figure, the axis orientation is interchanged for drawing convenience. All co-ordinates in μm. More precise results can be obtained with a finer scanning and a better reference.

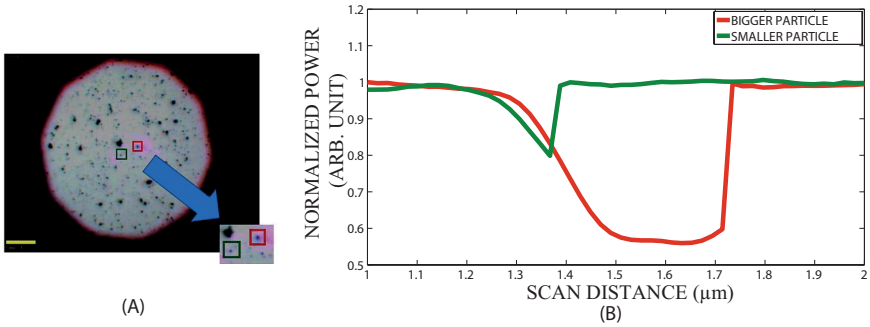

Figure 4.10: Difference of defect sizes as detected by CFS. In (a) the image of the sample size made using the white light source is shown with two pinhole defects of different sizes. The bigger on is boxed in red, and the smaller one boxed in green. The sizes of the smaller one is approximately 200-220 nm, while the bigger one is about 400-420 nm. The signal after they were scanned is shown in (b), using the same scanning parameters. The difference in sizes is evident from the scanning distances for which the normalized power is smaller than the reference.

of Fig. 4.10 we observe how this difference in size is visible in readout signal. From this, we can conclude that if a CFS system is calibrated for defects of known sizes, it can then give an approximate value of the particle size while detecting the particle, without making any additional measurement. This is discussed in detail later in chapter 7. Moreover, CFS is shown to be able to detect defects on a substrate having substantial surface roughness.

4.4. Conclusion

In this chapter we have discussed how Coherent Fourier Scatterometry (CFS) can be applied in the problem of detection of isolated particles and also shown how it can be used to detect particles down to size of diameter 100 nm on a silicon wafer surface. We mentioned how this method can distinguish between various defect sizes on an OLED sample and how enhanced SNR can be achieved by employing partial blocking of the aperture and how this can be predicted from the numerical model. The presence of the particle slightly away from the axis of the instrument creates far-field power distribution which is asymmetric, and we have shown that this loss of symmetry can be used to detect the scatterer with an enhanced SNR. Both of these techniques of SNR enhancement can be applied together to facilitate the detection. The coherence of the source makes it possible to add phase control in the illumination and to use the implicit polarization information. However, to avoid complexity and processing time, and also to primarily establish CFS for particle detection on a flat substrate, the experiments were performed in the most simple configuration possible which implies that higher sensitivity, if required, can be achieved by using more complex polarization control, structured illumination or with some data processing of different kind, without reducing the illumination wavelength. Some of this options were exercised in the remaining part of this thesis. It is important to point out that the simplicity of the method lies not only in its prac-

tical implementation but also in the analysis of the data it produces, since simple measurements, like change in the amount of power through the pupil or differential analysis, can be used for successful particle detection. This allows CFS particle detector to be used in environments where scanning speed has to be extremely high.

4.5. Acknowledgments

The author acknowledges Christiaan Hollemans of TNO, Delft and A. C. Assafrão for their help in the work presented in this chapter.

References

[1] S. Roy, A. C. Assafrão, S. F. Pereira, and H. P. Urbach, *Coherent fourier scatterometry for detection of nanometer-sized particles on a planar substrate surface,* Opt. Express **22**, 13250 (2014).

[2] H. Oerley, *Metrology systems for quality and process control of coatings on glass and plastic films,* Proceedings of International Conference on Coatings on Glass and Plastics (2012).

[3] J. F. Aguilar and E. Méndez, *On the limitations of the confocal scanning optical microscope as a profilometer,* Journal of Modern Optics **42**, 1785 (1995).

[4] J. Berger, *Detection of Particles on Clean Surfaces* (Springer US, 1989).

[5] A. Chen, V. Huang, S. Chen, C. J. Tsai, K. Wu, H. Zhang, K. Sun, J. Saito, H. Chen, D. Hu, M. Li, W. Shen, and U. Mahajan, *Advanced inspection methodologies for detection and classification of killer substrate defects,* Proc. SPIE **7140**, 71400W (2008).

[6] Editorial, *Embracing the organics world,* Nat. Mater **12**, 591 (2013).

[7] H. Hoppe and N. S. Sariciftci, *Organic solar cells: An overview,* Journal of Materials Research **19**, 1924 (2004).

[8] U. Okoroanyanwu et. al., *Towards the optical inspection sensitivity optimization of EUV masks and EUVL-exposed wafers,* Proc. of SPIE **8352** (2012).

[9] V. Bakshi, ed., *EUV Lithography* (SPIE Press, 2009).

[10] N. Engheta, *Circuits with light at nanoscales: Optical nanocircuits inspired by metamaterials,* Science **317**, 1698 (2007).

[11] A. Okamoto, H. Kuniyasu, and T. Hattori, *Detection of 30–40-nm particles on bulk-silicon and SOI wafers using deep UV laser scattering,* IEEE Transactions on Semiconductor Manufacturing **19**, 372 (2006).

[12] J. van der Donck, R. Snel, J. Stortelder, A. Abutan, S. Oostrom, S. van Reek, B. van der Zwan, and P. van der Walle, *Particle detection on flat surfaces,* Proc. SPIE **7969**, 79691S (2011).

[13] P. van der Walle, S. Hannemann, D. van Eijk, W. Mulckhuyse, and J. C. J. van der Donck, *Implementation of background scattering variance reduction on the Rapid Nano particle scanner,* Proc. SPIE **9050**, 905033 (2014).

[14] V. Jindal, A. John, J. Harris-Jones, P. Kearney, A. Antohe, E. Stinzianni, F. Goodwin, and T. Onoue, *Inspection and compositional analysis of sub-20 nm EUV mask blank defects by thin film decoration technique,* Proc. SPIE **8679, 86791O** (2013).

[15] B. Deutsch, R. Beams, and L. Novotny, *Nanoparticle detection using dual-phase interferometry,* Appl. Opt. **49**, 4921 (2010).

[16] J. Pospíšil and S. Nešpurek, *Photostabilization of coatings. mechanisms and performance,* Progress in Polymer Science **25**, 1261 (2000).

[17] N. Kumar, O. El Gawhary, S. Roy, V. G. Kutchoukov, S. F. Pereira, W. Coene, and H. P. Urbach, *Coherent fourier scatterometry: tool for improved sensitivity in semiconductor metrology,* Proc. SPIE **8324**, 83240Q (2012).

[18] A. da Costa Assafrão, A. J. H. Wachters, S. F. Pereira, and H. P. Urbach, *Near-field self-induced hollow spot through localized heating of polycarbonate/ZnS stack layer,* Appl. Opt. **51**, 7684 (2012).

[19] B. E. Roberds and S. N. Farrens, *An atomic force microscopy study on the roughness of silicon wafers correlated with direct wafer bonding,* Journal of The Electrochemical Society **143**, 2365 (1996).

[20] C. Teichert, J. F. MacKay, D. E. Savage, M. G. Lagally, M. Brohl, and P. Wagner, *Comparison of surface roughness of polished silicon wafers measured by light scattering topography, soft-x-ray scattering, and atomic-force microscopy,* Applied Physics Letters **66**, 2346 (1995).

[21] S. Harkema, S. Mennema, M. Barink, H. Rooms, J. S. Wilson, T. van Mol, and D. Bollen, *Large area ITO-free flexible white OLEDs with orgacon PEDOT:PSS and printed metal shunting lines,* Proc. SPIE **7415**, 74150T (2009).

[22] G. Videen, *Light scattering from a sphere on or near a surface,* J. Opt. Soc. Am. A **8**, 483 (1991).

[23] B. R. Johnson, *Calculation of light scattering from a spherical particle on a surface by the multipole expansion method,* J. Opt. Soc. Am. A **13**, 326 (1996).

[24] R. Schmehl, B. M. Nebeker, and E. D. Hirleman, *Discrete-dipole approximation for scattering by features on surfaces by means of a two-dimensional fast Fourier transform technique,* J. Opt. Soc. Am. A **14**, 3026 (1997).

[25] X. Wei, A. J. Wachters, and H. P. Urbach, *Finite-element model for three-dimensional optical scattering problems,* J. Opt. Soc. Am. A **24**, 866 (2007).

[26] P. Blake, E. W. Hill, A. H. Castro Neto, K. S. Novoselov, D. Jiang, R. Yang, T. J. Booth, and A. K. Geim, *Making graphene visible,* Applied Physics Letters **91**, 063124 (2007).

[27] O. G. Rodríguez-Herrera, D. Lara, K. Y. Bliokh, E. A. Ostrovskaya, and C. Dainty, *Optical nanoprobing via spin-orbit interaction of light,* Phys. Rev. Lett. **104**, 253601 (2010).

[28] H. R. Huff, R. K. Goodall, E. Williams, K. Woo, Y. Liu, H. Benjamin, T. Warner, D. Hirleman, K. Gildersleeve, W. M. Bullis, B. W. Scheer, and J. Stover, *Measurement of silicon particles by laser surface scanning and angle-resolved light scattering,* Journal of The Electrochemical Society **144**, 243 (1997).

5

CFS for Particle Detection : Enhancement by Illumination Shaping

1. Two orthogonal, coherent linearly polarized waves cannot interfere.
2. Two parallel coherent linearly polarized waves will interfere in the same way as natural light.

First two statements of Fresnel-Arago Laws

Parts of this chapter have been published in Phys. Rev. Lett. **114**, 10 (2015) [1].

In this chapter we will focus on the incident illumination part of CFS. To do that, it is important for us to understand the phenomena happening in the far-field as a particle is scanned, and only after understanding that we can determine what illumination will be the optimal to maximize the sensitivity in the far field. From the basic geometry of the 'particle on a plane substrate' problem, it is known to us that the far-field is a superposition of specular reflected and scattered radiation [2, 3], and the illumination being coherent, it is a superposition of amplitudes. Thus, the far field is basically an interference pattern, with the scanning providing modulation. The sensitivity to detect any change in this pattern is mostly suitable when the pattern is asymmetric. This is the knowledge we have from last chapter.

5.1. Introduction

A variation of the 'particle detection on a planar surface' problem, namely, particle detection in a solution, has importance in the field of biological microscopy [4]. A number of works intended for that field forms a good source to look for more information, for example, in Ref. [5, 6]. The main message from these works on nano-particle detection is : since the scattered field amplitude decreases with the third power of the scattering particle size and hence the intensity varies with the sixth power, the field detection type solutions (mainly interferometric techniques) are significantly more sensitive for this problem. Unfortunately, an interference with external reference wave, like ICFS discussed in Chapter 3, is not a practical solution when the detection has to be done very fast on a moving substrate. However, these references still motivate us to check if it is possible to use this unavoidable interference taking place in the far field between specular reflection and scattered wave to increase the sensitivity of detection of particle.

In this chapter we present a modified CFS configuration that utilizes radially polarized light at $\lambda = 405$ nm to simultaneously detect sub-wavelength nano-particles and locate them with high accuracy and speed limited mainly by experimental noise. The method is based on the interaction of the scattering and spurious reflected field and uses differential data-processing, so that just a quadrant detector can be used for the whole detection scheme. To do that, in this chapter we shall be using the same procedure to simulate the quadrant detector by a camera as was done in last chapter.

It is intercutting to note when the scattering particle is on a substrate, a common path interferometric phenomenon is initiated between the reflected and scattered field which can be modulated by small shifts of the scatterer, resulting in a detectable asymmetry in the far-field. This asymmetry effect is somewhat similar to optical spin-Hall effect [7] of fields with spin momentum, although, the physical principles are different. Similar interference effect also has been utilized by several authors [2, 3] to develop techniques that can track metal nano-particles in water as small as 5 nm, using confocal or wide-field microscopy (not differential detection). These techniques are mainly targeted towards biological microscopy which utilizes the metal nano-particles as labels. The situation is different for particle detection for contamination control, for this case the particles are most often dielectric on a flat substrate in air.

5.2. Theory

To understand the principle in more detail, let us consider a Cartesian system (x, y, z) with z as propagation direction. An electric dipole in air with dipole vector $\boldsymbol{q} = (q_x, q_y, q_z)$ at the origin radiates electric field $\boldsymbol{E}^{dip}$ [8]

$$\boldsymbol{E}^{dip}(\boldsymbol{r}) = -\frac{k^2}{\epsilon_0}\boldsymbol{q}G(\boldsymbol{r}) - \nabla(\boldsymbol{\nabla}.\frac{\boldsymbol{q}}{\epsilon_0}G(\boldsymbol{r})), \tag{5.1}$$

where, $G(\boldsymbol{r})$ is the free space Green's function and k is the wave number. Taking the Fourier transform in a plane orthogonal to z,

$$F\left[\boldsymbol{E}^{dip}(k_x, k_y, z)\right] = -(k^2\boldsymbol{q} - (\boldsymbol{k}.\boldsymbol{q})\boldsymbol{k})\frac{e^{ik_z z}}{2ik_z}, \tag{5.2}$$

where $\boldsymbol{k} = k_x\boldsymbol{x} + k_y\boldsymbol{y} + k_z\boldsymbol{z}$ is the wave vector.

The plane wave expansion of an electric field is commonly written in terms of the complex amplitudes of the perpendicular (s) and parallel (p) components to the plane of incidence [9]

$$\begin{aligned} A_s^{dip} &= \frac{1}{2i\epsilon_0}\frac{k/k_z}{\sqrt{k_x^2 + k_y^2}}[kk_xq_y - kk_yq_x] \\ A_p^{dip} &= \frac{1}{2i\epsilon_0}\frac{k/k_z}{\sqrt{k_x^2 + k_y^2}}[k_xk_zq_x + k_yk_zq_y - (k_x^2 + k_y^2)q_z], \end{aligned} \tag{5.3}$$

where, $\boldsymbol{A^{dip}} = A_s^{dip}\boldsymbol{s} + A_p^{dip}\boldsymbol{p}$ is the complex vector amplitude of the plane waves. With proper sign of k_z, Eq. 5.3 is valid when the field propagates along positive or negative z. If an objective, with z axis as optical axis, is placed such that its geometrical focus is at the origin, then the outgoing s and p fields are respectively converted to azimuthally (A_ϕ)[1] and radially (A_ρ) polarized field in the pupil plane through $(A_\phi^{dip}, A_\rho^{dip}) = \sqrt{k/k_z}(A_s^{dip}, A_p^{dip})$ [10]. If the dipole is on a substrate there will be other fields besides $\boldsymbol{E}^{dip}$, which we are going to consider.

From Eq. 5.3, we note that if the dipole moment is oriented along z, i.e., $q_x = q_y = 0$, then the electric field at the pupil of the objective is purely radially polarized. Conversely, it is well known that the field at the focus of a radially polarized pupil distribution has large longitudinal component [11, 12]. Thus a dipole, which is excited by a tightly focused radially polarized wave, will also radiate radially polarized light. If the dipole is on a substrate, there will also be the spurious reflected field which is obviously radially polarized. The whole objective-dipole system works as a common path interferometer. The contrast of the superposition of this scattered field and the spurious reflected field will be high since the interfering

[1] To avoid confusion, we have used ϕ to denote azimuthally polarized field and φ for the azimuthal angle. Also, (ρ, ϕ) basis denotes the same plane, the entrance/exit pupil, as the (ξ, η) basis. For this chapter, it is more useful to use the (ρ, ϕ) basis.

fields are parallel polarized at every point in the pupil. This situation arises when a sub-wavelength nano-particle present on a planar surface is illuminated by a focused radially polarized wave. A reasonable approximation of the dipole moment $\boldsymbol{q}$ is to assume it to be proportional to the incident local electric field $\boldsymbol{E}^f$ at the position of the nano-particle through the complex polarizability α which depends on the material, size and surrounding of the particle [5][2]. $\boldsymbol{E}^f$ is expressed in terms of incident plane wave amplitudes $\boldsymbol{A}^i$ at objective pupil as

$$\boldsymbol{E}^f(\boldsymbol{r}) = \int (A^i_\phi \hat{\boldsymbol{s}} + A^i_\rho \hat{\boldsymbol{p}}) e^{i\boldsymbol{k}\cdot\boldsymbol{r}} \sqrt{k_z/k}\, dk_x dk_y. \tag{5.4}$$

If the incident field is radially polarized before the objective, $A^i_s = A^i_\phi \sqrt{k_z/k} = 0$, and close to focus, $\boldsymbol{E}^f(\boldsymbol{r}) \approx E^f(\boldsymbol{r})\hat{z}$. Following the shift properties of the Fourier transform, if we shift the nano-particle in the focal plane along the x axis by $r = x$ then there will be a corresponding phase shift of $ik_x x$ in the scattered far-field. The resulting scattered field components can now be written from Eq. 5.3 as $A^{dip}_s = 0$ and

$$\begin{aligned} A^{dip}_p &\approx -\frac{\alpha}{2i\epsilon_0}\left[\frac{k\sqrt{k_x^2+k_y^2}}{k_z}\right] E^f(x) e^{ik_x x} \\ &\approx -\frac{\alpha}{2i\epsilon_0}\left[\frac{k\sqrt{k_x^2+k_y^2}}{k_z}\right] E^f(0) e^{ik_x x}, \end{aligned} \tag{5.5}$$

where, we assume that $x << \lambda$.

However, there will be another part of the scattered field which is reflected from the substrate. We also assume the dipole to be very close to the substrate interface so that the phase difference between the directly scattered and reflected scattered signal is very small compared to the wavelength of illumination. This assumption is approximately valid in the experiments when the beam is focused at the interface, so that the effective dipole remains very close to the surface. Moreover, this phase is not a function of x. Under this assumption, the total scattered signal can be obtained by multiplying Eq. 5.5 by $1+r_p$, where, r_p is the complex Fresnel reflection coefficient for p polarization. Thus, the total outgoing complex field $\boldsymbol{A}^o$ can be

[2] It is interesting to note that for metal particles in dielectric media, α can be made to approach very large values which increases the scattering from the particle by large amount. This fact is utilized in iSCAT microscopy [3], but not applicable in our case.

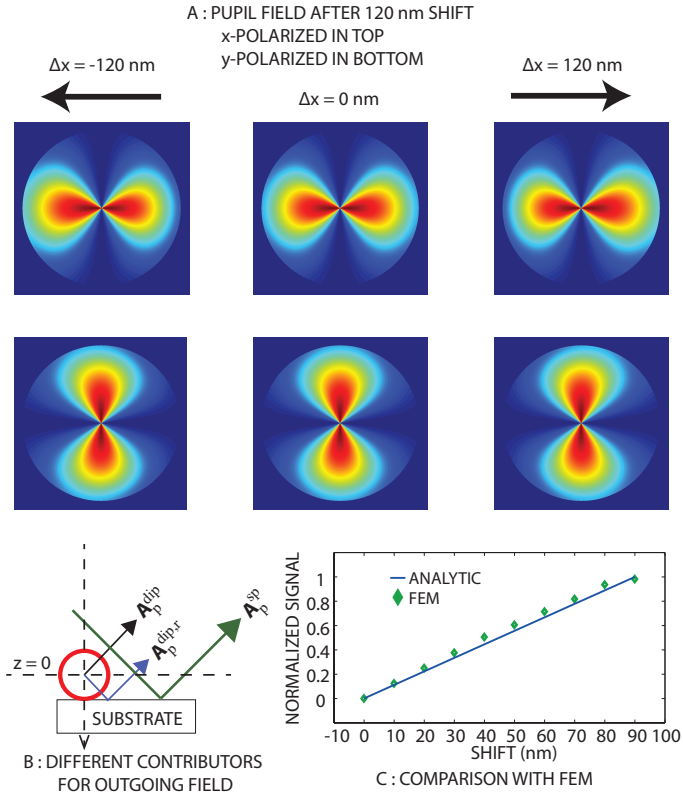

Figure 5.1: In top (A): x and y-polarized field ($|E_x^{pupil}|$ and $|E_y^{pupil}|$), respectively on top and bottom row, at pupil after a large shift of 120 nm, when visible asymmetry can be observed. The fields are calculated from analytic model. In bottom (B) : The different contributors towards outgoing field. In (C) : A comparison between the single dipole model (blue line) and FEM simulations (green diamond) of difference of the total intensities in the left and right halves of the pupil for the for x-component of the far-field. For $x < 100$ nm, the variation is almost linear with a slope of 1.1%/nm of maximum signal, which is approximately proportional to $r_p(1 + r_p)\alpha$, for given NA, λ and $\boldsymbol{A}^{inc}$.

written as a superposition of the total scattered and spurious reflected wave as

$$\begin{aligned} A_s^o &\approx 0 \\ A_p^o &\approx r_p A_p^i \\ &\quad - (1 + r_p)\frac{\alpha}{2i\epsilon_0}\left[\frac{k\sqrt{k_x^2 + k_y^2}}{k_z}\right] E^f(0) e^{ik_x x}. \end{aligned} \tag{5.6}$$

Here, the spurious reflected field is the incident field $\boldsymbol{A}^i$ directly modulated by r_p. The effect of the modulation by shift x in the pupil is an asymmetry of energy distribution between the left and right half. This can be seen in part A of Fig. 5.1 where the field amplitudes in the pupil for x and y polarized outgoing field is plotted. Three cases are shown as the particle moves from $\Delta x = -120$ nm to $\Delta x = 120$ nm. Visible asymmetry can be seen for both polarizations, however, the effect is more pronounced for x-polarized field. This implies that data from each polarization bears information based on the direction of the shift of the particle, and thus, the particle can be located in two orthogonal direction almost independently. Also, it implies quantitatively a differential analysis between these halves of the pupil will be related to the shift of the particle (a through-focus shift z-axis will also create a phase difference between the scattered signals, which is not possible for particle on a substrate, however, that does not create asymmetry). In part B of Fig. 5.1 different fields that are contributing towards the total outgoing field A_p^o are shown. The scattered field consists of directly scattered ($\boldsymbol{A}_p^{dip}$) and reflected-scattered ($\boldsymbol{A}_p^{dip,r}$), where, from our assumption, $\boldsymbol{A}_p^{dip,r} = r_p \boldsymbol{A}_p^{dip}$. The specular reflected field is $\boldsymbol{A}_p^{sp} = r_p A_p^{inc} \boldsymbol{p}$. Thus, for each $\boldsymbol{k}$, total outgoing signal is $\boldsymbol{A}_p^o = \boldsymbol{A}_p^{sp} + \boldsymbol{A}_p^{dip} + \boldsymbol{A}_p^{dip,r}$.

More conveniently, because of the shape of the field distribution, no power flows on the optical axis in the pupil. This makes the system more robust for a differential analysis than incident fields without a singularity, such as the circularly polarized field. For this a small alignment error in the optical system will not produce large error in the differential signal. To note, the differential signal will not only be zero when there is no particle ($\boldsymbol{A}_p^{dip} = 0$) but also when the particle center coincides with the spot ($x = 0$) axis restoring the symmetry. This fact can be used to localize the particle.

To validate the analytic model, a comparison of it with FEM simulation (similar to chapter 1.3) with following simulation parameters : A particle of diameter 100 nm on Silicon substrate ($\lambda = 405$nm, $NA = 0.9$, substrate refractive index $5.42 + 0.33i$, particle refractive index 1.5) is also performed. The result is shown in part B of Fig. 5.1. Here the differential signal between two halves of the pupil is plotted as a function of shift x. We can observe a good match in the small shift regime, with deviation starts to build up after $x = 90$ nm as the transverse components become stronger. The area where the model remains valid, $0.16\lambda^2$, is slightly less than the longitudinal spot size $0.2\lambda^2$ [11].

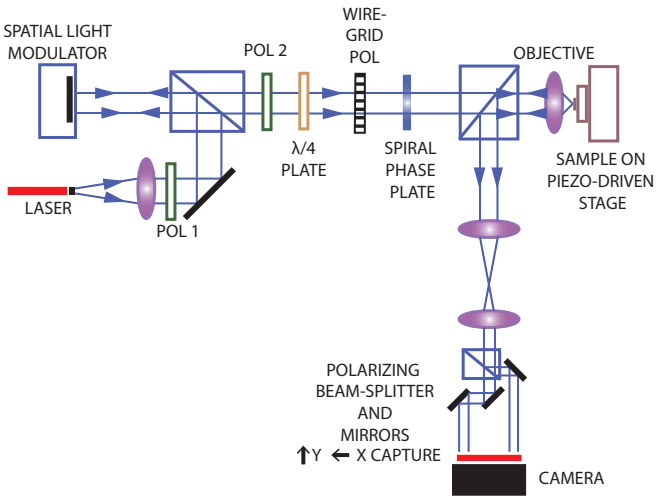

Figure 5.2: A schematics of the experimental setup, which is slightly modified version of the setup shown in Fig. 4.2 to incorporate incident radial polarization and simultaneous x and y polarized light capture.

5.3. Samples and Experimental Setup

For experimental demonstration, the same sample mentioned in the previous chapter, by depositing PSL spheres of diameter 95 ± 7 nm on a polished silicon wafer with rms roughness < 3 nm over an area of 5 μm^2 [13], is used. The experimental setup is shown in Fig. 5.2. A collimated diode laser beam at $\lambda = 405$ nm with beam diameter of 3.8 mm passes through two Glan-Laser prism polarizers and a Holoeye LC-R2500 (SLM). The SLM is used to create an annular incident field. After that, a quarter-wave plate, a wire grid polarizer (WGP) and a spiral phase plate is used to create radial polarization [14, 15]. The WGP, consisting of concentric Al cylinders on the glass substrate, was specially fabricated to generate radially polarized light at wavelength of 405 nm [16]. This beam is focused by an objective ($f = 2$ mm) of NA =0.9 on the sample on a PI P-611.3 NanoCube XYZ 100x100x100 μm closed loop piezo driven stage. The reflected beam is split by the polarizing beam splitter and mirrors such that two beams of orthogonal linear polarizations can be recorded on the same camera.

5.4. Experiments

In the experimental setup, the intensity data captured in the camera simultaneously provides information for x and y direction by monitoring the difference in energy between two lobes. The LR signal, obtained from only the x-polarized field, is shown in left column of Fig. 5.3 A,C, while the TB signal, obtained from only y-polarized field, is shown in the right column of Fig. 5.3 B,D. The top row (Fig. 5.3 A,B) are for full aperture illumination and the bottom row is for annular aperture $0.5 \leq NA \leq 0.9$. Annular aperture, created using the SLM to shape the pupil, is known to enhance

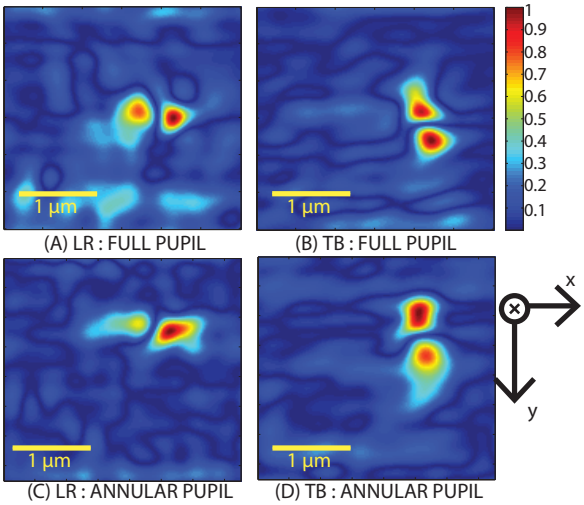

Figure 5.3: Experimental LR and TB differential scanning maps of an 3×3 μm^2 area of the sample containing one nano-particle. A Gaussian low-pass filter has been applied to reduce noise of the data. The plots are normalized and in absolute numbers. To draw the maps, firstly, frames on the rightmost line parallel to y are taken as reference. Each of them is subtracted from all other frames on the same scan-line parallel to x to eliminate effects of internal reflections from optical elements [2]. Then, differential signals are calculated between top-bottom (TB) or left-right (LR) halves (for example, $LR = \left| \iint_L \left| E_x^{pupil} \right|^2 - \iint_R \left| E_x^{pupil} \right|^2 \right|$, where L,R respectively denotes left and right half of pupil). Finally this signal is normalized by the maximum of each map.

the longitudinal field generation for radial polarization [11], and so, it should be more effective in detection. Moreover, from previous chapter, we know that annular aperture helps to increase the sensitivity of detection (section 4.3.3). The combined effect is seen in Fig. 5.3, where the bottom row has larger size of the 'patch' in the particle location, implying it has been detected from larger distance. This is useful to reduce the number of scan lines for faster detection.

To localize the particle, it is necessary to find the zero-crossing positions, which translates to finding the minimum between the two peaks when absolute values are plotted. This is a different numerical problem than image based localizations [17, 18]. The final convergence will be determined by the sensitivity of the method which is dependent mainly on the slope of the signal and the measurement noise level. A closer look at the slope is shown in Fig. 5.4. In the top of Fig. 5.4, experimental LR cross section is shown for both full and annular apertures, parallel to x. A positive detection is made when SNR reaches above certain threshold. Thus, detection is more effective with the annular aperture, for which we have approximately 20% wider signal. This also proves that the dipoles excited by longitudinal components are contributing more to the signal than transverse ones. The slope near the minimum is almost similar for both cases, because, when the particle approaches very close to the center of the spot, relative amplitudes of longitudinal to transverse components become almost similar for both apertures. In the bottom of Fig. 5.4, LR and TB signals are plotted for the same scan line parallel to y. The scanning direction is also reflected by the number of peaks in each signal. Specifically, a changing sign of TB signal, which is evident from the two peaks, indicates that the scanning direction is y. This is an important reason for independent localization in two orthogonal directions, and therefore, the working of this method. Near the spot center, the slope seen in the measured signal is about 0.75%/nm for TB and 0.65%/nm for LR (fraction of the maximum signal), somewhat smaller than the slope predicted from theory (Fig.5.1). For the present experiment, since no special noise control was used, the noise values were typically higher (4% and 6% of maximum signal, in TB and LR respectively, indicated approximately by the black arrow), yielding a positional uncertainty $\Delta x \Delta y \approx \frac{noise}{slope} \approx 7.7 \times 3$ nm^2. This is in the same order of accuracy as obtained by tracking of individual fluorescent molecules [19]. Special noise controls can reduce the noise significantly, for example a noise level of 1% of the maximum signal can yield $\Delta x \Delta y \approx 2 \times 2$ nm^2 using this method.

5.5. Discusssion

In this chapter, we present how the use of radially polarized light can increase the detection sensitivity of CFS particle detector. Although a camera and a piezo-scanner is used in primary experimental verification of the principle, in production environment commercial actuators and a pair of differential detectors (similar to [6]) can be used to obtain detection speed in the order of centimeters per second, and detection-localization speed of tens of millimeters per second, like compact-disc readers [20]. Our final results show that a localization accuracy of $\approx 10^{-4}\lambda^2$ is possible with a particle of area $\approx \lambda^2/16$, almost independently in two orthogonal

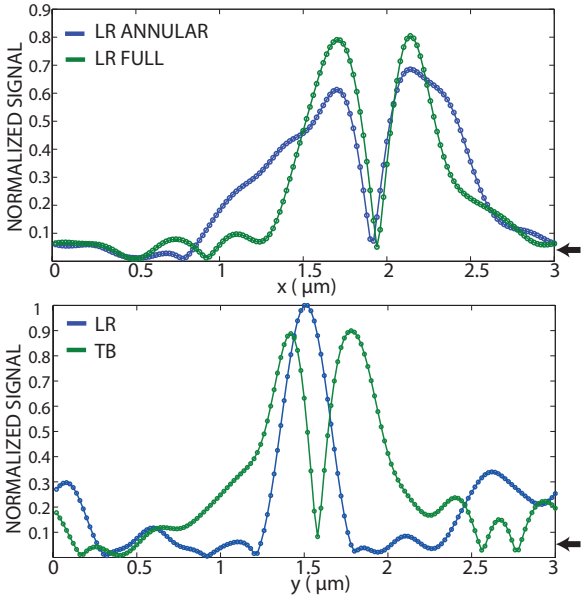

Figure 5.4: Top : Experimental LR profile comparison along x for annular aperture (blue) and full aperture (green). Bottom : Experimental LR (blue) and TB (green) profile of the same scan line parallel to y. For both figures, the experimental noise level is shown by the black arrow, approximately to scale. Actual scan points are spaced 20 nm apart.

directions.

There are definitely more ways to improve the sensitivity of the system. Firstly, extending the benefits of pupil shaping, the illumination can be even better optimized for the specific problem parameters [21]. In the final chapter (chapter 8) we will show an approach to this problem using the Lagrange Multiplier methods. Secondly, the substrate can also be modeled to enhance the interaction [22] (if it is possible to be chosen). This is essentially the topic to discuss in the next chapter. Thirdly, we can also take some additional measures to reduce the noise. For these results, we have taken the final scan line parallel to y as reference. In principle the reference positions can be anywhere, chosen randomly or systematically, provided it is sufficiently far from the scatterer. In this way, under noisy environment, it is possible to take several measurements from single experiment and average the results.

We would like to conclude this part of the present chapter by thinking about a possible application of this technique for moving particles on a substrate. This method can also be used to determine direction of motion of a moving scattering particle under stationary spot by rotating the polarizing beam splitter such that either the LR or the TB signal attains minimum modulation, which will then show the direction orthogonal to the particle motion.

5.6. Acknowledgments

The author acknowledges Katsiaryna Ushakova and Quincy van den Berg for their help in the work presented in this chapter.

References

[1] S. Roy, K. Ushakova, Q. van den Berg, S. F. Pereira, and H. P. Urbach, *Radially polarized light for detection and nanolocalization of dielectric particles on a planar substrate,* Phys. Rev. Lett. **114**, 103903 (2015).

[2] V. Jacobsen, P. Stoller, C. Brunner, V. Vogel, and V. Sandoghdar, *Interferometric optical detection and tracking of very small gold nanoparticles at a water-glass interface,* Opt. Express **14**, 405 (2006).

[3] J. Ortega-Arroyo and P. Kukura, *Interferometric scattering microscopy (iscat): new frontiers in ultrafast and ultrasensitive optical microscopy,* Phys. Chem. Chem. Phys. **14**, 15625 (2012).

[4] T. Plakhotnik and V. Palm, *Interferometric signatures of single molecules,* Phys. Rev. Lett. **87**, 183602 (2001).

[5] B. Deutsch, R. Beams, and L. Novotny, *Nanoparticle detection using dual-phase interferometry,* Appl. Opt. **49**, 4921 (2010).

[6] A. Mitra, B. Deutsch, F. Ignatovich, C. Dykes, and L. Novotny, *Nano-optofluidic detection of single viruses and nanoparticles,* ACS Nano **4**, 1305 (2010).

[7] O. G. Rodríguez-Herrera, D. Lara, K. Y. Bliokh, E. A. Ostrovskaya, and C. Dainty, *Optical nanoprobing via spin-orbit interaction of light,* Phys. Rev. Lett. **104**, 253601 (2010).

[8] L. Novotny and B. Hecht, *Principles of Nano-Optics*, 1st ed. (Cambridge University Press) pp. 484–486.

[9] J. Braat, S. van Haver, A. Janssen, and P. Dirksen, *Progress in optics*, edited by E. Wolf, Vol. 51 (Amsterdam: Elsevier, 2010) Chap. 6, pp. 349–468.

[10] L. Novotny and B. Hecht, *Principles of Nano-Optics*, 1st ed. (Cambridge University Press) pp. 56–60.

[11] R. Dorn, S. Quabis, and G. Leuchs, *Sharper focus for a radially polarized light beam,* Phys. Rev. Lett. **91**, 233901 (2003).

[12] Q. Zhan and J. Leger, *Focus shaping using cylindrical vector beams,* Opt. Express **10**, 324 (2002).

[13] C. Teichert, J. F. MacKay, D. E. Savage, M. G. Lagally, M. Brohl, and P. Wagner, *Comparison of surface roughness of polished silicon wafers measured by light scattering topography, soft-x-ray scattering, and atomic-force microscopy,* Applied Physics Letters **66**, 2346 (1995).

[14] Q. Zhan, *Cylindrical vector beams: from mathematical concepts to applications,* Adv. Opt. Photon. **1**, 1 (2009).

[15] H. Wang, L. Shi, B. Lukyanchuk, C. Sheppard, and C. T. Chong, *Creation of a needle of longitudinally polarized light in vacuum using binary optics,* Nat. Photon. **2**, 501 (2008).

[16] K. Ushakova, A. d. Costa Assafrao, S. F. Pereira, and H. P. Urbach, *Near ultraviolet-visible radial wire grid polarizer for tight focusing applications,* Optical Engineering **54**, 104101 (2015).

[17] N. Bobroff, *Position measurement with a resolution and noise-limited instrument,* Review of Scientific Instruments **57**, 1152 (1986).

[18] L. Novotny and B. Hecht, *Principles of Nano-Optics*, 1st ed. (Cambridge University Press) pp. 111–121.

[19] A. Yildiz, J. N. Forkey, S. A. McKinney, T. Ha, Y. E. Goldman, and P. R. Selvin, *Myosin v walks hand-over-hand: Single fluorophore imaging with 1.5-nm localization,* Science **300**, 2061 (2003).

[20] G. Bouwhuis, J. Braat, A. Huijser, J. Pasman, G. van Rosmalen, and K. Schouhamer-Immink, *Principles of optical disc systems,* (Adam Hilger, Bristol, 1985) pp. 70–71.

[21] H. P. Urbach and S. F. Pereira, *Field in focus with a maximum longitudinal electric component,* Phys. Rev. Lett. **100**, 123904 (2008).

[22] Y. Hennequin, C. P. Allier, E. McLeod, O. Mudanyali, D. Migliozzi, A. Ozcan, and J. M. Dinten, *Optical detection and sizing of single nanoparticles using continuous wetting films,* ACS Nano **7**, 7601 (2013).

6

CFS for Particle Detection : Enhancement effect by the Substrate

We do not doubt that there are
many further practical consequences of this concept;

Sir J. B. Pendry on perfect lens [1]

While discussing the problem of detection of a scatterer on a flat substrate, we have already covered two possible ways to improve the detection sensitivity. At first, in chapter 4, we discussed how CFS can benefit from using simple detection techniques like differential detection by having not only an increased sensitivity but also a faster operation. After that, in chapter 5, we discussed how the specific polarization of the incident wave can enhance the system sensitivity. In this chapter, we will discus how the substrate affects the sensitivity enhancement. It can be argued that this method of engineering the substrate might alter the properties of a substrate and so, may not be ultimately beneficial. However, we intend to show here how a very thin layer ($\approx \lambda/20$) on a substrate, which we will refer to as enhancing layer, can significantly enhance the delectability of particles on it. In many situation, such a thin layer might not substantially change the outcome.

6.1. Introduction

The motivation of this part of the thesis came from works related to theoretical exploration using negative refractive index medium (both negative electric permitivity ε and magnetic permeability μ), pioneered by Veselago [2]. It was later suggested by Pendry [1] that this effect can be exploited to achieve super-resolution using restoration of amplitudes, also known as the enhancement of evanescent waves by negative index medium. Although such material does not exist in reality, in optical frequency and in for subwavelength strucures the assumption of almost no coupling between electric and magnetic field is still valid (quasi-static assumption), one can approximate such a material by thin slabs of noble metals in p-polarized light [3]. It was later shown that similar enhancement can also be realized by thin layer of dielectrics with some absorption, for example El Gawhary [4] treats the problem with III-V elements, while Zhang [5] uses absorptive glass. These results were interesting to researchers not only for the fact that it explained more clearly the working principle of the enhancing layer but it was also of significant design interest, as such a design can be fabricated without extensive effort. This is because the practical benefits of using dielectric instead of metal. Among many, an important one is that maintaining the flatness of a very thin layer of dielectric is easier than metal. This indicates the fabrication can be extended to large area deposition, which can have significant impact in many applications of microscopy, such as biological samples in iSCAT microscopy [6], or in the problem of particle detection which we have been dealing with. These results also strengthen the fact that surface plasmonic effects may not be the only origin of the enhancement, rather, excitation of guided modes inside the enhancing layer could be another way to obtain it [7].

Being motivated by these works, it was interesting for us to investigate how the behavior of two samples under identical conditions, one of a particle on a substrate and the other of a particle on a substrate with an enhancing layer, will differ when detection of the particle is concerned. These simple samples, together with our differential detection scheme, is very suitable to show the evanescent wave enhancement, which we explain in next section. In the remaining part of this chapter we treat this question with numerical simulations and experimental results. We shall concentrate on the difference in terms of detection sensitivity of two samples

with and without enhancement to show the presence of the enhancement. For simplicity, we will consider only a single layer of fixed thickness under fixed illumination wavelength. We refrain ourselves from the discussion of whether or not it would have been possible to further enhance the effect by optimizing the enhancing layer into multiple layers of different thicknesses. For this, one may refer to various works in this topic, for example, [8, 9]. Specifically, we consider the physical thickness of the enhancing layer to be 20 nm throughout this chapter, unless otherwise specified. The substrate is assumed to be glass of refractive index of 1.48. We do not consider the substrate to be dispersive, since the refractive index variation of glass in the visible range is very small compared to the materials that will be used for enhancing layers.

6.2. Numerical Simulations

Let us consider the basic model of the problem first. We can follow the procedure outlined in [4], where, first a simplified model, evaluated using a thin-film modeling algorithm based on multiple beam interference formulae [10], is used to verify the feasibility of the enhancing layer design. And then rigorous simulations were performed.

The origin of the enhancement is due to guided modes coupled inside the enhancing layer. Thus, one needs an element inside the sample to effectively generate the evanescent modes so that they can be coupled. Commonly, a subwavelength grating [3, 4] or a prism [5] is used to generate those modes, however, in our case, we have the advantage that they can be generated by the subwavelength particle scatterer. Once the evanescent waves are amplified, we need another element to scatter them back in the far field as propagating waves, the particle itself is suitable to do that task as well. Essentially, the system should work as the following,

1. The subwavelength particle scatterer, illuminated by a focused field, will generate propagating and evanescent waves.
2. Guided mode(s) inside the enhancing layer will be excited by these waves.
3. The guided mode(s) generated from evanescent waves will extend out of the layer and interact with the particle. The particle will scatter back some part of the radiation in the detector, resulting in an increased sensitivity.

These steps are illustrated schematically in Fig. 6.1. The differential LR or TB detection scheme of CFS particle detector eliminates any effect regarding change of reflectance of the substrate due to the addition of the enhancing layer, and brings out the evanescent wave enhancement effect only.

Our starting point to analyze the problem by investigating the enhancement effects with a simplified thin-film model. We are interested in how the modulus of the intensity reflection coefficient, R, is modified by the presence of the enhancing layer[1]. Let us define the normalized x-component of the incident wave vector $\boldsymbol{k}^i$ as

[1] Since they are physically similar, we have used the same symbol $\boldsymbol{R}$ for indicating the reflection matrix for grating in chapter 3, however, for gratings, the reflection matrix always contained a subscript indicating the corresponding order, for layers, this is absent.

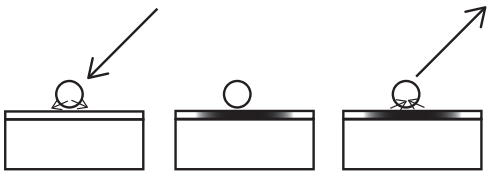

Figure 6.1: The three stages of scattering from a particle on an enhancing layer. Left: Coupling of incident light, Middle: Generation of guided mode(s), Right: Scattering of evanescent waves.

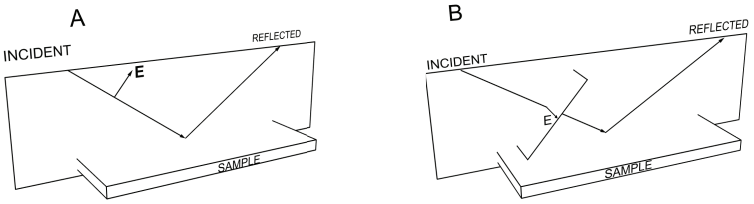

Figure 6.2: The parallel p polarization (A) and perpendicular s polarization (B) incident on a sample. The electric field direction is shown.

β^i, i.e., $\beta^i = k_x/n^i k_0$, where, n^i is the refractive index of incident medium, which, in our case, is air[2]. Similarly, β^o can be defined for outgoing field. The incident wave in general can be s or p polarized, (shown in Fig. 6.2), and we need to solve for these two cases separately.

The intensity reflectance of the substrate should be enhanced in presence of the layer. Let us consider the case in which evanescent waves, generated by the particles, are incident from the air side to the substrate with β^i, where, $10 \geq \beta^i > 1$. The upper limit of β^i is chosen arbitrarily, which can be any value > 1 depending on the specific situation. One has to check that this upper limit of β^i is not too low so that some evanescent waves which might have been significantly amplified are not considered, and on the other hand, it should not be extremely large so that the computational load becomes unnecessarily very high. For the present case, we verified that this range is nearly optimal.

To have a quantitative idea about the enhancement, we can define percentage enhancement EP as

$$EP(\lambda) = \frac{\int_{\beta^i}\int_z R_{enh} d\beta^i dz - \int_{\beta^i}\int_z R_{oriz} d\beta^i dz}{\int_{\beta^i}\int_z R_{oriz} d\beta^i dz} \tag{6.1}$$

where R_{enh} and R_{oriz} are the intensity reflectance of the sample calculated with and without enhancing layer, respectively. z is the distance in air from the air-enhancing

[2]To avoid confusion we would like the reader to note that β and ξ, both representing the normalized x-component of the wave vector, is differentiated with respect to their applicability. We have used ξ in the far field and it represents propagating wave ($\xi \leq 1$). On the other hand, we use β in the near-field which can take any value, propagating or evanescent.

layer (with enhancement) interface or the air-glass layer (without enhancement) interface. The integration over β^i and z gives us an measure of overall enhancement not only at the interface but also near it for a large number of wave vectors. This consideration is necessary for practical point of view, as the scattering particles have certain size.

It was found that the dependence on EP with wavelength λ due to dispersion of the material in the enhancing layer is an important observation to give insight into the mechanism. To have a specific example, we consider three different materials, two III-V elements - Indium Antimonide (InSb) [11] and Gallium Arsenide (GaAs) [12]; and glass (BK7) [13], each deposited as a thin layer of 20 nm separately on a dispersion free glass substrate. Percentage enhancement EP from these three samples are shown in Fig. 6.3. Following Eq. 6.1, a value of $EP > 0$ means enhancement. Plot A, for GaAs, shows very high enhancement for s polarization and for $\lambda > 700$ nm. For shorter wavelength, p-polarized waves show better enhancement. For InSb the plot is shown in B, the behavior is also similar, however, the enhancement is in a smaller scale. Moreover, to verify the correctness of the simulations, we also use BK7 as an enhancing material. The results in C are for BK7, which expectedly, shows no enhancement. There is actually a small loss in case of BK7, since its refractive index is always slightly smaller than substrate.

The enhancing layer, essentially works as a slab waveguide and cavity. The behavior of larger enhancement of p polarized wave for shorter wavelength and s for larger wavelength can be explained by following the idea from Pendry, [1]. The message from those equations are, if an evanescent wave $\sim \exp(ikx)$ (with purely imaginary k) is to be amplified, one has to find a way to change the sign in the exponent. This can be done when the wave is put inside a Fabry-Perot cavity, as then, the transmittance or reflectance takes the form of $\sim \frac{\exp(ikx)}{1-F(r,t)\exp(i2kx)}$, where, $F(r,t)$ is a function which depends on cavity reflectance or transmittance. If $F(r,t)$ is sufficiently large, then amplification of evanescent wave can take place, with a consequent attenuation of propagating waves. The best condition is when the denominator approaches zero, infinite amplification occurs for any wave, leading to resonance. This is essentially step 2 in the work mechanism of the our system, excitation of guided modes. Certainly, for the highly subwavelength thickness of 20 nm of the enhancing layer, the modes it can support has to be highly evanescent in air. The fundamental mode in a slab waveguide is s, which is why for larger wavelengths only s polarized waves can be supported. For shorter wavelength, p polarized waves can also guide modes. This may be the reason why p polarized waves tend to be enhanced in shorter wavelengths. To be noted, generally the absorption is higher for shorter wavelength, and consequently, EP will be smaller for shorter wavelengths than higher wavelength. On the other hand, this increasing absorption implies the existence of guided modes can be over a large band of wavelengths. However, at this point, it is necessary to further analyze the reason(s) for enhancement of p-polarized light in dielectric in shorter wavelengths and relate it to absorption to justify our intuitive ideas. We will explore the effects of absorption in enhancement layers with another example later in section 6.4.

Moving on to the rigorous simulations with FEM (similar to chapter 1.3 with

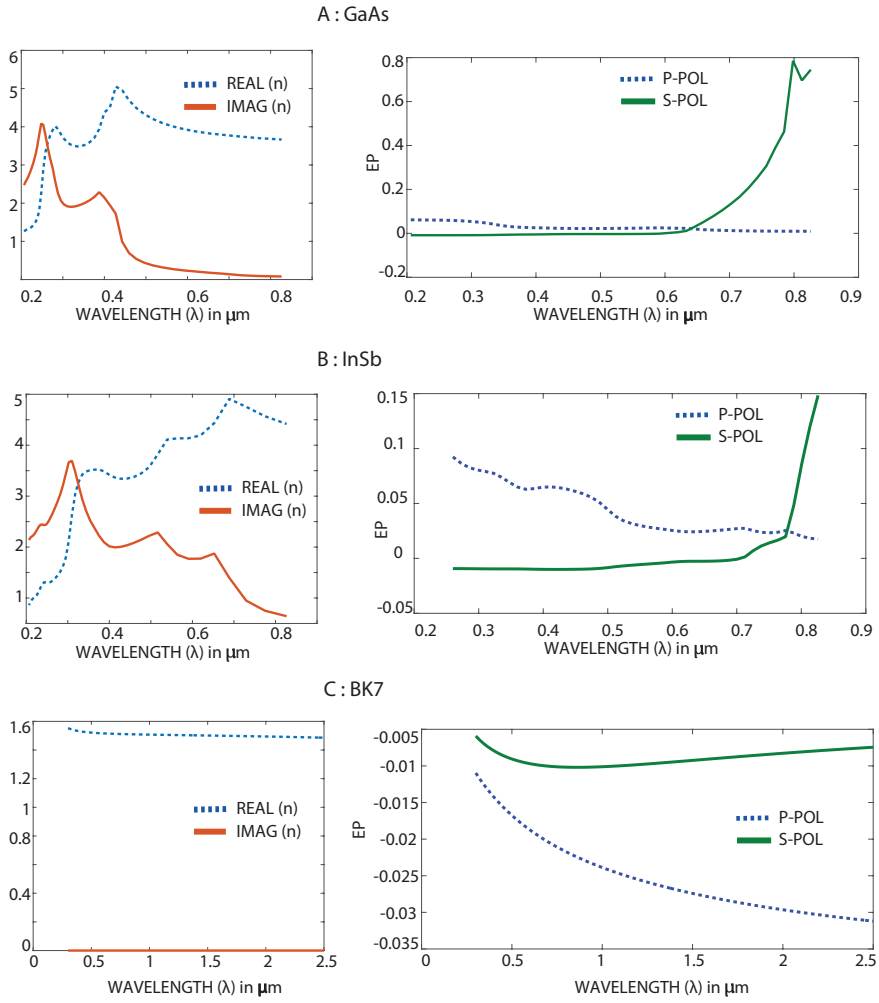

Figure 6.3: The left column shows the variation of real (blue, broken) and imaginary (red, solid) part of refractive index. The right column of figures show percentage enhancement EP for s (green , solid)and p polarization (blue, broken) as a function of wavelengths for the three materials of the enhancing layer each with a thickness of 20 nm. The substrate is assumed to be glass ($n = 1.48$, without dispersion). The incident medium is air. β^i is varied from 1 to 10, and z from 0 to 100 nm, both in 100 steps. From top row to bottom, results are for (A) : GaAs, (B) : InSb and (C) : BK7. Note the difference in scales for each plot. It should be noted that these results are specific to the thickness of the layer and can change for other thickness.

Table 6.1: Simulation Parameters

	$\lambda = 405$nm	$\lambda = 632$nm
InSb layer refractive index	$3.4 + 2i$	$4.28 + 1.81i$
NA	0.9	
Particle refractive index	1.5	
Substrate refractive index	1.48	

the parameters shown in table 6.1. The results for FEM simulation of a 200 nm PSL particle on glass and on 20 nm thick InSb coated glass is shown in Fig. 6.4, assuming the incident light is linearly polarized along x (see, for reference, Fig. 1.1). The illumination wavelength is 632 nm for part A (in top part) of the picture where we have used a larger computation volume (as already detailed in chapter 1.3). The modulus of the x-component of the electric field, $|E_x|$ is shown, respectively without (top row) and with the enhancing layer (bottom row) of InSb for two positions of the particle. For the left column, the particle is at the center of the spot, while, for the right column, it is shifted in the x direction by 150 nm. In part (B) of the same figure, the same field is shown for 405 nm illuminating wavelength, for the case when the particle is at center of the spot. A cross section of the field modulus is also provided, to have an idea about the contrast improvement. The effect of the enhancing layer is clearly seen in both the cases. Essentially, the sensitivity for LR or TB signal (see chapter 5.4) towards a shift calculated from these simulations are about one order better in the presence of the enhancing layer as compared to the case when there is no enhancing layer.

6.3. Experimental Results

To verify the principles, two physical samples were made. The first one was 200 nm PSL particles on a flat glass plate (UV grade fused silica, flatness less than 20 nm, 5 mm thick). The second one was a 600 μm glass plate of same material with a layer of 20 nm InSb [14]. Both substrates can be considered infinitely thick for visible wavelengths. The experimental setup is the same one mentioned in Fig. 4.2 in Chapter 4, except only one difference that we will be using both the 632 nm He-Ne Laser illumination and the 405 nm illumination. This is for two reasons, although from Fig. 6.3, the enhancement for 20 nm InSb is better for shorter wavelength of 405 nm, the particle is more subwavelength for larger wavelength of 632 nm, which should generate evanescent waves more efficiently. Thus, this way we can have a better overall verification of the principle. Similar to Chapter 4, the incident light is taken as linearly polarized along x, producing both s and p polarized fields. Each time the two samples were scanned with same setup, with identical power level, ambient temperature and exposure time. The results are shown in Fig. 6.5, where on top we show the variation of LR signal in two cases for a scanning area of $10 \times 15\mu$m^2 area with samples per 10 nm separation. The effect of enhancing layer is evident from the signal maps in part A and B of Fig. 6.5. Quantitatively, the enhanced sample shows an increased contrast of about 5.34 times better than the

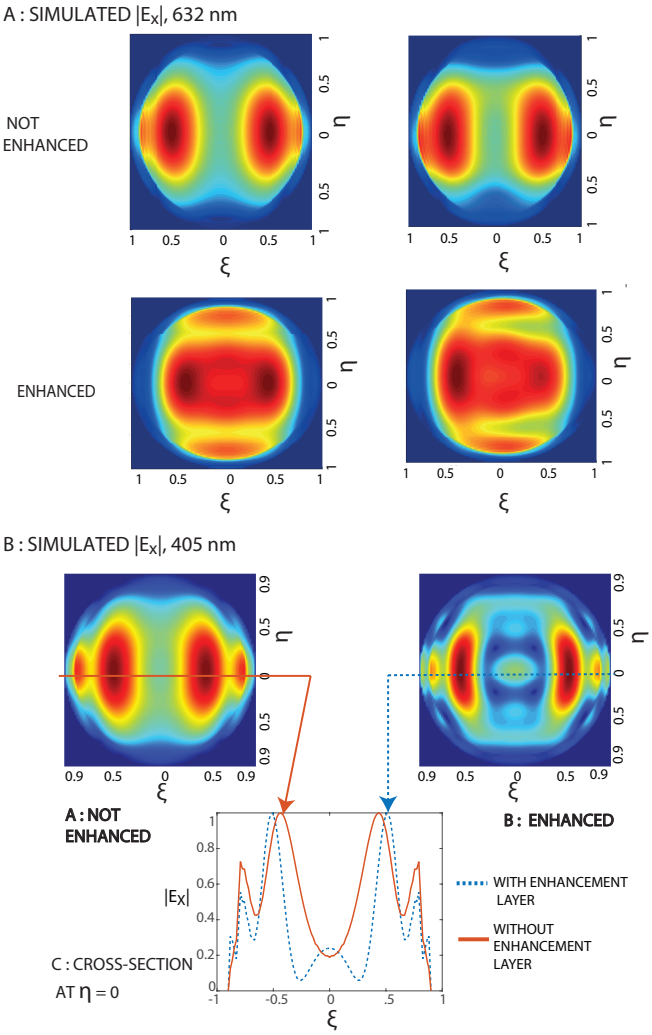

Figure 6.4: In the top part (A) : The simulated absolute value of the electric field ($|E_x|$) at far-field for 632 nm illuminating wavelength, assuming a linearly x-polarized incident field. The left column is when the particle is at center of the spot (or the z-axis, see chapter 1.2), while the right is for particle shifted by $x = 150$ nm. The upper row shows the field without the layer, and lower row shows the field with the layer. The effect of the layer is clearly visible. In the bottom part, (B) the same field for 405 nm illuminating wavelength in the presence of the particle is shown (no shift), together with a cross-section. All the plots are normalized to unity and have the same colormap.

standard sample without enhancement, with an increased photon count of about 1.35 times. In the lower part of the figure, we show the LR signal variation map for the same pair of samples at 405 nm for a scanning area of 10 μm^2 with same sampling rate. The conclusion is similar, the enhanced sample produces an increased contrast of about 3 times. The enhancement for this case is smaller than expected, for which the reason may be that the particle was not small enough so that the propagating waves generated were quite significant. Probably, this is why the particle is better detected for the sample without enhancing layer at this wavelength than at larger wavelength of 632 nm.

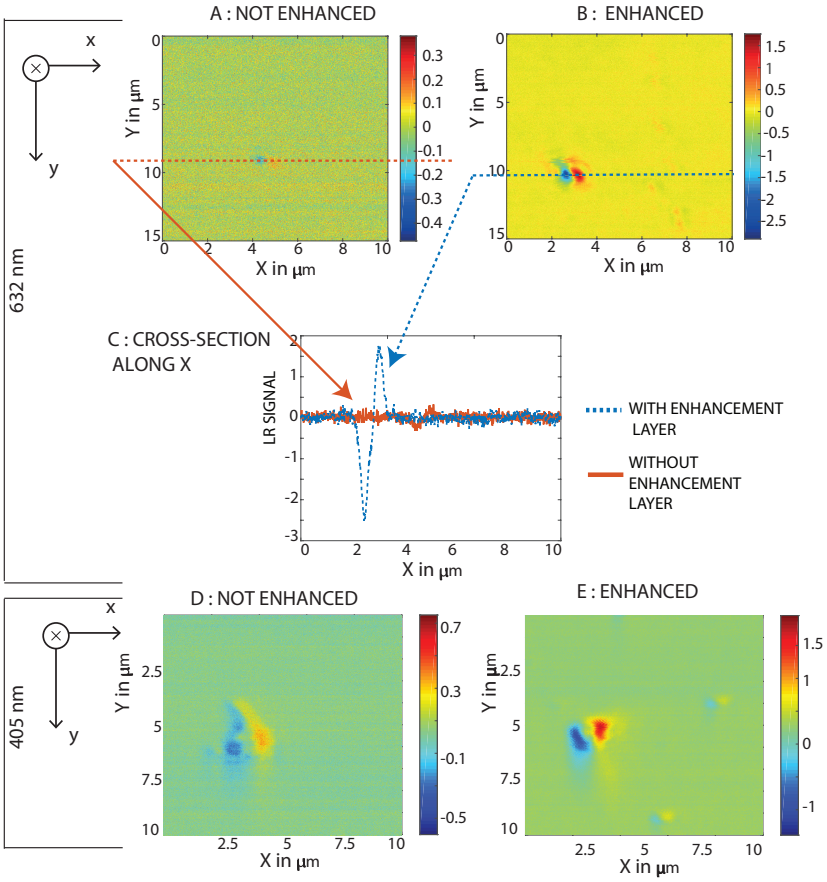

Figure 6.5: The experimental far-field LR signal maps for a glass substrate containing 200 nm PSL particles without (A) and with (B) enhancement layer, under identical condition. The dynamic range of signal (max-min) is 5.47 times better with the sample having the enhancement layer. In (C) we show the cross-section of the maps along x axis. The signal from the glass substrate is barely modulated (red, continuous line) , whereas, the signal from glass substrate with enhancing layer (blue, broken line) is significantly modulated. In (D) and (E), results when the same experiment is repeated for illumination wavelength of 405 nm without and with enhancing layer, respectively. The bias level of the signal for 632 nm is about 0.1V, while at 405 nm it is about 0.17V, irrespective of sample type.

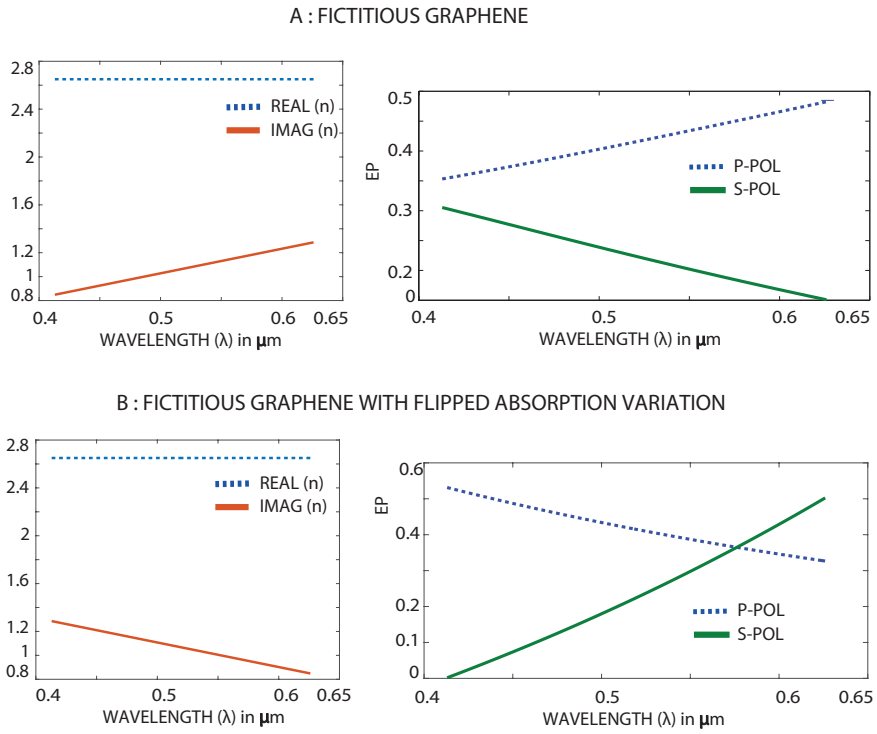

Figure 6.6: Left (right) column shows refractive index (enhancement percentage) of a 20 nm layer by two fictitious materials each with a constant real part of refractive index. In the top row the material has a increasing absorption (A) and that gives rise to a gradually decreasing EP for s-polarization (gradually increasing for p polarization). In the bottom row the material has an deceasing absorption (C) which gives rise to a gradually increasing enhancement for s-polarization (gradually decreasing for p-polarization).

It is also important to consider that all the signal maps are obtained from differential signal, making them independent of any change in the amount of power reflected back directly from the substrate without the presence of the particle. Or in other words, the measurements are independent of the change of sample reflectivity. The signal cannot change between samples far away from the particle because of this differential nature of the signal.

6.4. Discussion and Outlook

Before starting with the discussions, we would like to point out that fact that all simulations presented in this chapter are for the specific thickness of the layer. In fact, similar to a guided mode in a waveguide, the thickness can have a definite relationship with wavelength which can be used to design highly resonating structures. However, that discussion about optimization of the structure, as stated before, is beyond the scope of this thesis.

It is interesting to analyze the effect of absorption on the enhancement fac-

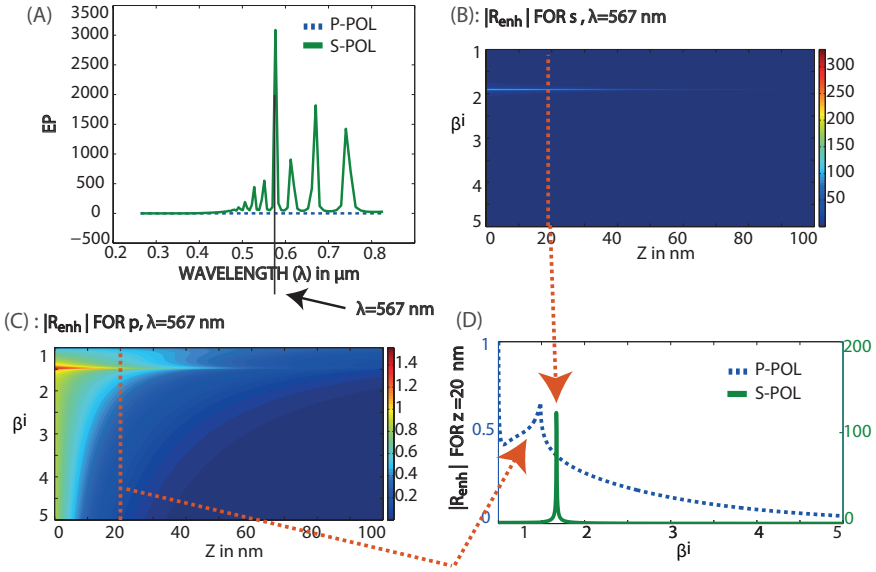

Figure 6.7: A: Variation of EP with wavelength for a 20 nm layer of Silicon. Very large value of EP is observed. In B: $|R_{enh}|$ is plotted for s-polarization in $\beta^i - z$ plane. In C: $|R_{enh}|$ is plotted for p-polarization in $\beta^i - z$ plane. In D : Comparison of the enhancement between s and p polarization is made by plotting $|R_{enh}|$ for $z = 20$ nm for both cases.

tor EP, which also brings out polarization dependence of the enhancement more clearly. For example, in Fig. 6.6 we consider two 'fictitious' materials. For each of them the imaginary part (absorption) of the refractive index varies linearly with wavelength, either increasing or decreasing, while the real part stays the same. For the top row (part A) of Fig. 6.6, the real part of the refractive index stays at 2.65 and the imaginary part increases linearly with wavelength. The exact values are typical for Graphene [15, 16] but we consider much larger thickness of 20 nm. The percentage enhancement EP increases for p-polarized wave with wavelength, while it decreases for s-polarized wave. In the bottom row (Fig.B), the simulations for the same fictitious material is shown, only now with the absorption decreasing with wavelength. The effect on EP becomes opposite, i.e., it increases with for s-polarization and decreases for p-polarization. These examples show that there is a relation between absorption coefficient and the polarization of the enhanced evanescent wave.

Finally, we would like to consider another material with interesting behavior, Silicon (Si), for which the variation of EP with wavelength is shown if Fig. 6.7. The enhancement for s-polarization shows very narrow and large peaks. This is due to resonant coupling of guided modes which gives rise to very strong but very narrow enhancements at specific wavelengths. This is shown in the top left part (A) of the figure. A specific example at $\lambda = 567nm$ resonant peak, is shown in part (B) where the variation of $|R_{enh}|$ for s-polarization is plotted in the $\beta^i - z$ plane. Very large

and narrow enhancement is seen at $\beta^i = 1.67$. The similar plot for p-polarization is shown in part C (bottom-left). The resonance is significantly weak for this case. This comparison is made in (D), where we plot $|R_{enh}|$ at $z = 20$nm from the air-Si interface for both polarization. The difference in scale for p (blue, left side) and s (green, right side) is significantly large.

6.5. Acknowledgments

The author greatly acknowledges Dr. Omar El Gawhary and Xukang Wei for their help to perform the works presented in this chapter.

References

[1] J. B. Pendry, *Negative refraction makes a perfect lens,* Phys. Rev. Lett. **85**, 3966 (2000).

[2] V. G. Veselago, *The electrodynamics of substances with simultaneously negative values of ϵ and μ,* Sov. Phys. Usp. **10**, 509 (1968).

[3] Z. Liu, S. Durant, H. Lee, Y. Pikus, N. Fang, Y. Xiong, C. Sun, and X. Zhang, *Far-field optical superlens,* Nano Letters **7**, 403 (2007).

[4] O. El Gawhary, N. J. Schilder, A. da Costa Assafrao, S. F. Pereira, and H. P. Urbach, *Restoration of s-polarized evanescent waves and subwavelength imaging by a single dielectric slab,* New Journal of Physics **14**, 053025 (2012).

[5] Y. Zhang, C. Arnold, P. Offermans, and J. G. Rivas, *Surface wave sensors based on nanometric layers of strongly absorbing materials,* Opt. Express **20**, 9431 (2012).

[6] J. Ortega-Arroyo and P. Kukura, *Interferometric scattering microscopy (iscat): new frontiers in ultrafast and ultrasensitive optical microscopy,* Phys. Chem. Chem. Phys. **14**, 15625 (2012).

[7] J. Christensen and F. J. García de Abajo, *Slow plasmonic slab waveguide as a superlens for visible light,* Phys. Rev. B **82**, 161103 (2010).

[8] R. Lopez-Boada, C. J. Regan, D. Dominguez, A. A. Bernussi, and L. G. de Peralta, *Fundaments of optical far-field subwavelength resolution based on illumination with surface waves,* Opt. Express **21**, 11928 (2013).

[9] C. J. Regan, D. Dominguez, L. Grave de Peralta, and A. A. Bernussi, *Far-field optical superlenses without metal,* Journal of Applied Physics **113**, 183105 (2013).

[10] M. Born and E. Wolf, *Principles of Optics*, 7th ed. (Cambridge University Press, 2003).

[11] D. E. Aspnes and A. A. Studna, *Dielectric functions and optical parameters of Si, Ge, GaP, GaAs, GaSb, InP, InAs, and InSb from 1.5 to 6.0 eV,* Phys. Rev. B **27**, 985 (1983).

[12] D. E. Aspnes, S. M. Kelso, R. A. Logan, and R. Bhat, *Optical properties of* $Al_xGa_{1-x}As$*,* Journal of Applied Physics **60**, 754 (1986).

[13] *SCHOTT optical glass data sheets*, SCHOTT, Duryea, PA (2012).

[14] A. C. Assafrao, A. J.H. Wachters, M. Verheijen, A. M. Nugrowati, S. F. Pereira, H. P. Urbach, M. F. Armand, and S. Olivier, *Direct measurement of the near-field super resolved focused spot in insb,* Opt. Express **20**, 10426 (2012).

[15] M. Bruna and S. Borini, *Optical constants of graphene layers in the visible range,* Applied Physics Letters **94**, 031901 (2009).

[16] S. Cheon, K. D. Kihm, H. g. Kim, G. Lim, J. S. Park, and J. S. Lee, *How to reliably determine the complex refractive index (RI) of graphene by using two independent measurement constraints,* Scientific Reports **4**, 6364 EP (2014), article.

7

CFS for Particle Detection : Calibration and Working Prototype

Everything is theoretically impossible,
until it is done.

Robert A. Heinlein

Parts of this chapter has been published as an article in Rev. Sci. Instr. (2015) [1].

In this chapter of the thesis, we show the results after implementing a prototype of the CFS particle detector setup in a roll-to-roll production line in Holst Center, Eindhoven to evaluate its performance. We also present results about an experiment in which we compared the performance of CFS particle detector with a benchmark dark field particle scanner called Rapid Nano, from TNO, Netherlands [2, 3]. Finally, we present some results of detection particles below 100 nm.

7.1. Introduction

In previous chapters we have presented methods to enhance the sensitivity of particle detection in CFS, and in this chapter, we show the implementation of CFS as a prototype for online particle detection measurements. As we have already mentioned, the intention of the *Clean4Yield* project was to help migrate flexible electronics production procedure from sheet-to-sheet to roll-to-roll line for higher yield [4, 5], and so it is necessary to check whether the prototype is able to detect particles down to 100 nm with the full speed of the roll, which is 3 meter/minute, under production environment. Moreover, to ensure that all the scatterers of size 100 nm or more are detected, we carried out a comparison experiment with a standard dark field scanner. These results will be presented in this chapter.

This chapter is organized as follows: in the next section, we describe the optical setup and explain how the illumination and the detection system work. The subsequent section contains the results, which are presented in three steps. Firstly, we show the results of off-line experiments to calibrate the experimental setup with known scatterer size. Secondly, we present the results obtained from a working prototype installed in production environment and use the data obtained from the off-line experiment to find the scatterer size distribution. Thirdly, we compare the performance of the experimental bright field scanner with a standard dark field scanner. Finally, we present the discussions.

7.2. Experimental Setup

Although we are using almost the same setup as shown in Fig. 4.1, we give a short description of the exact prototype we used to highlight the small changes. The schematics of the bright field scanner capturing the far field distribution is shown in Fig. 7.1. In the present setup, illuminating wavelength is $\lambda = 405$ nm, with the numerical aperture of the microscope objective being $NA = 0.9$. Also for all the results which will be presented in this chapter, only LP light was used. A telescopic demagnifying arrangement is made with lens L1 ($f = 6$ cm), L2 and L3 (both $f = 4$ cm) to accommodate the complete beam inside the central part of the detector. The whole instrument, except the objective aperture, was encased inside a box of dimension 40 cm $\times$ 20 cm $\times$ 10 cm. The sample can be placed in a scanning table, or, is automatically scanned in case of a moving roll to roll line. The detection is performed by a single split detector (SD1) when the sample is scanned in one direction. In table 7.1, the parameters of the SD1 are given. For two dimensional scanning, a pair of similar split detectors (SD1 and SD2) were simulated from the camera using the same scheme as explained in chapter 4.3.3.

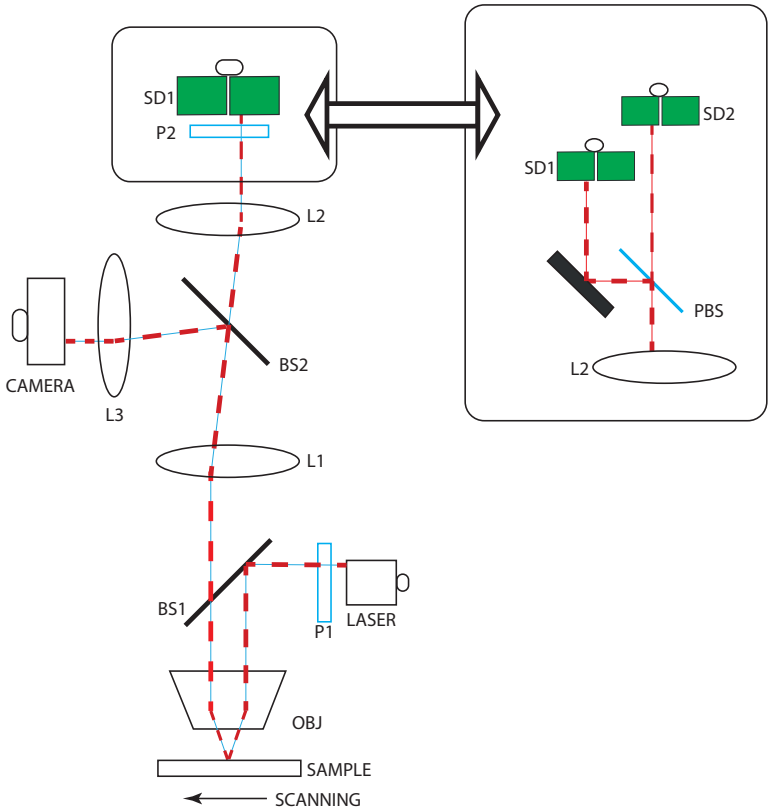

Figure 7.1: The prototype CFS to be tested for particle detection. This is the prototype version of CFS bright field particle detector (Fig. 1.1). Light coming from the LASER is linearly polarized with polarizer P1 before being incident on the sample through beamsplitter BS1 and a microscope objective. The sample is placed in the focal plane of the objective and can be scanned in that plane. The reflected beam, containing both specular and scattered light, is demagnified (in the present setup at 3:2) before being incident on a CAMERA and a split detector SD1. To upgrade the prototype for two-dimensional particle detection one can use a polarizing beamsplitter (PBS) and a pair of split detectors SD1 and SD2. The signal from the split detector is amplified and digitized using an 16-bit Analog to Digital Converter (ADC) and a Field Programmable Gate Array (FPGA).

Table 7.1: Parameters of the split detector(s): Advanced Photonix Bi-Cell Silicon Photodiode

Active area	2×1.22 mm
Dark Current	$\leqslant$5 nA
Responsivity	$\geqslant$0.32 A/W
Noise Equivalent Power	2.5×10^{-14} W/$\sqrt{Hz}$
Response time	$\approx$ 190 ns

From previous chapters, especially from Fig. 4.9, we know that the LR and TB signals coming from the detector(s) are typically in the form of a pulse with a positive and a negative peak. The part of the pulse between the positive and negative peak signifies restoring of the symmetry in the far field due to the coincidence of the scanner optical axis (z-axis) with the center of the scatterer and can be used for localization. The width of the pulse is related to the size of the particle while the difference between absolute values of the peaks is a measure of how well the particle is scanned. A symmetric pulse with the same magnitude of voltage of the positive and negative peak implies that the scanner axis has passed through the center of the particle. In production environment, it is very rare to have a perfectly symmetric pulse, however, slightly imperfect symmetric pulses can also be utilized for approximate scatterer size determination.

For the task of comparison of the CFS bright field detection system with a benchmark dark field particle scanner Rapid Nano [2], a special sample was made and was characterized by both scanners. A square frame shaped marker, with 1 μm frame edge width and 100 μm inner square width, is first patterned by e-beam lithography on a 150 nm Zep520 resist film spin coated on Silicon substrate; the pattern is then transferred to the silicon substrate by reactive ion etching with a depth of around 80 nm, by using the pattern resist film as a mask. The remaining resist is removed by Nitric Acid. This pattern works as a marker to designate the required scanning area. Then PSL spheres of 100 nm diameter were deposited on the sample with a density of about 30000 spheres/ sq.mm.

For the performance evaluation under production environment, the prototype scanner was installed in a roll to roll flexible electronics production line where a web[1] of polymer substrate was driven under the scanner. The stability of the web was maintained using a commercial air bearing from IBS Precision Engineering of Netherlands. The transverse vibrations perpendicular to the web was less than a few microns once the air table and web motion had stabilized, and thus, no additional mechanism was necessary to keep the web at the focal plane of the objective. It was sufficient to scan in only a single direction to evaluate this specific task and only a single detector was used, while the moving web automatically provided the necessary linear movement for scanning.

7.3. Results

7.3.1. Off-Line Measurements

At first, off-line experiments were performed to find the relation between pulse width and the size of the particle. The pulse that is observed by scanning a 100 nm diameter scatterer is shown in part A of Fig. 7.2. To separate the pulse from noise, a thresholding is performed and then the pulse converts to two successive square pulses of alternating polarity (the dashed line in Fig. 7.2). The pulse width is then determined by adding the width of both pulses and the time T occurred due to the error in thresholding. Different pulse widths were calibrated using known scatterer

[1] A very wide ($\approx$ 1meter) sheet of polymer substrate is termed as web in industrial terminology (see Fig. 1.6).

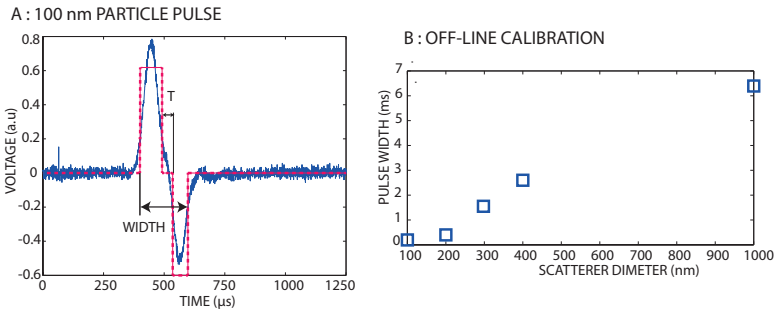

Figure 7.2: A : a typical pulse from a 100 nm scatterer and the corresponding square pulses (broken red line), and the error T (explained in detail in the text). B: Variation of pulse width with different scatterer size. Both plots assume a scan speed of 0.3 m/min.

sizes, and this plot is shown in the part B of Fig. 7.2, where the pulse widths of symmetric pulses, assuming a web speed of 0.3 m/min (the low speed), are plotted for different scatterer sizes. The approximate width of the pulse generated by a 100 nm scatterer is about 200 μs at this speed. It can be noted that the pulse widths fall almost linearly till scatterer size reaches below 200 nm, which is approximately the diffraction limit for $\lambda = 405$ nm, and then decreases more gradually.

7.3.2. In-Line Measurements

The performance evaluation of the experimental scanner in the production environment was done on a polymer web in the roll to roll production line at two different speeds, low (0.3 m/min) and high (3 m/min). For creating artificial contamination in the clean web, dense solution of 100 nm PSL spheres (10% solid content) diluted to 1% solids content with 90 vol% H_2O and 10 vol% Isopropanol, was sprayed across the width of the web intermittently, making successive stripes of contaminated and clean web. The data from the scanner were captured at a sampling rate of 1 MHz, which was limited by the present electronics in the prototype but can be increased with better components[2]. The results are shown in Fig. 7.3, top (low speed) and bottom (high speed). Referring back to Fig. 7.2, to evaluate the scatterer count, the number of pulses (asymmetric and symmetric) within a time frame has to be counted. In Fig. 7.3 the scatterer counts/sec is plotted against time. The green continuous line shows the contaminated stripes clearly, also showing their width and scatterer density variation along the width. The blue broken line shows similar data from a clean part of the web, with a very low scatterer count. The results were similar for both speeds. For both of these experiments, the incident power was 20 μW, which corresponds to a dose of 21.2×10^{-6} μJ/μm^2, assuming a spot size of 1 μm in diameter and the sampling rate of 1 MHz.

In order to find the size of the contaminating scatterers, the width of the symmetric pulses can be used. The size distribution of the contaminating scatterers

[2]In the present setup, the slowest component was the ADC and FPGA assembly. With a 8-bit ADC, the bandwidth can be increased significantly, without significant loss of sensitivity.

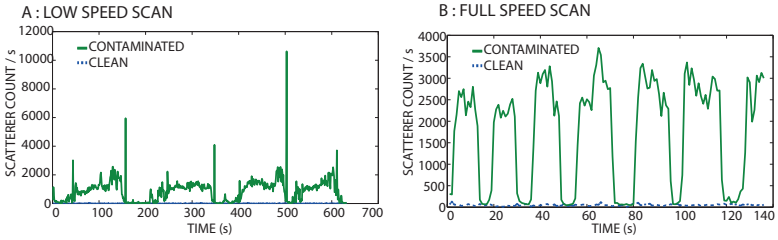

Figure 7.3: The particle count variation with time for two different web speeds : low web speed 0.3m/min (in A) and full web speed (in B). The contaminating stripes are clearly differentiated from clean parts, also the density variation of scatterers in each stripe can be seen. For A, large number of particle counts are observed at the end of each stripe, which is probably because of the accidental increase of the particle deposition rate just before sprayer was stopped.

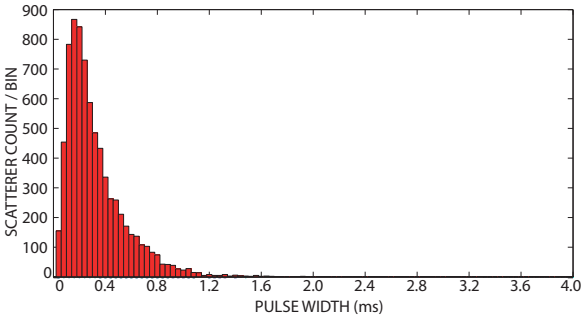

Figure 7.4: The size distribution of the particle scatterers as obtained from pulse width. It shows the size distribution of contaminating particles from the data obtained from the low web speed of 0.3 m/min. The bin size of pulse width is 0.04 ms. The maximum count lies in the region of pulse width 200 μs, which corresponds to a scatterer size of 100 nm. For this plot, minimum and maximum values of T were 20 μs and 400 μs, respectively, and pulses having a difference of less than 10% between their positive and negative peaks were considered as approximately symmetric.

were calculated from the data obtained while scanning the sample at low speed because the sampling rate of 1 MHz was not sufficient to sample the pulses at high web speed without distortion. The symmetric pulses generally constitute a very small fraction of the total number of pulses and a special algorithm was needed to separate symmetric pulses from all the other pulses. To do this, we convert the obtained pulses into square shaped pulses by using a threshold voltage, depending on the detector noise level. This implies the central part of a symmetric pulse will be below this threshold voltage and will be consequently approximated erroneously to zero. This error in approximating the square shaped pulses from the real experimental pulses is shown in Fig. 7.2 as T. The time error T is the key parameter to check to find out whether a pulse is indeed symmetric, or it is just two different asymmetric pulses of opposite polarity in succession (i.e., coming from two different scatterers in opposite sides of the spot). For the former case, T is much smaller.

The size distribution after analyzing the symmetric pulses is shown in Fig. 7.4, counting symmetric pulses up to 4 ms in time, corresponding to a particle size of about 500 nm. There are several interesting observations that can be made from this distribution. Firstly, the maximum number of pulses have a width of about 200 μs, which corresponds to the correct size of the contaminating scatterer of 100 nm. Secondly, there are also scatterers of sizes above 100 nm, which is due to clusters of 100 nm scatterers. We are unable to differentiate those clusters from single scatterers from present measurements. Thirdly, there are also some pulses of smaller width than 200 μs, which at first, seems to be an error. However, it can be explained considering two unwanted contamination sources: scatterers from air and the droplets of solvent liquid, both of which can be smaller than the contaminating scatterer size.

7.3.3. Comparison Measurements

The aim of the comparison experiment was to verify the reliability of the CFS bright field scanner by comparing the number of scatterers it detects inside a specific area of the sample with that of a benchmark dark field scanner, in this case, the Rapid Nano developed by TNO [2]. It can detect particles down to 42 nm in size on flat surfaces [6]. The detection is based on a step-and-repeat principle: multiple images of approximately 1 sq. mm are stitched together to create an overview image of an entire sample. The measurement time for each individual image is 50 ms. During this time laser light with a wavelength of 532 nm was used to illuminate the sample. Different incident power levels, ranging from 0.01 to 4.00 W can be used; higher powers are typically needed for detection of smaller particles.

In the part A of Fig. 7.5, one can see the result from Rapid Nano. The illumination time was 50 ms at a power level of 0.10W. The beam spot size of the laser on the substrate is approximately 2 mm. This gives an average intensity of 0.03W/mm^2, so the sample was exposed to a total light dose of 1.5 mJ/mm^2. The scatterer size of 100 nm is significantly above the detection limit of Rapid Nano, and all the 6 scatterers inside the square area are clearly visible. In the right side of the image, the result from the CFS particle detector is shown. The size of the marker was bigger than the full range of the X-Y stage, which was used for this off-line experiment, and

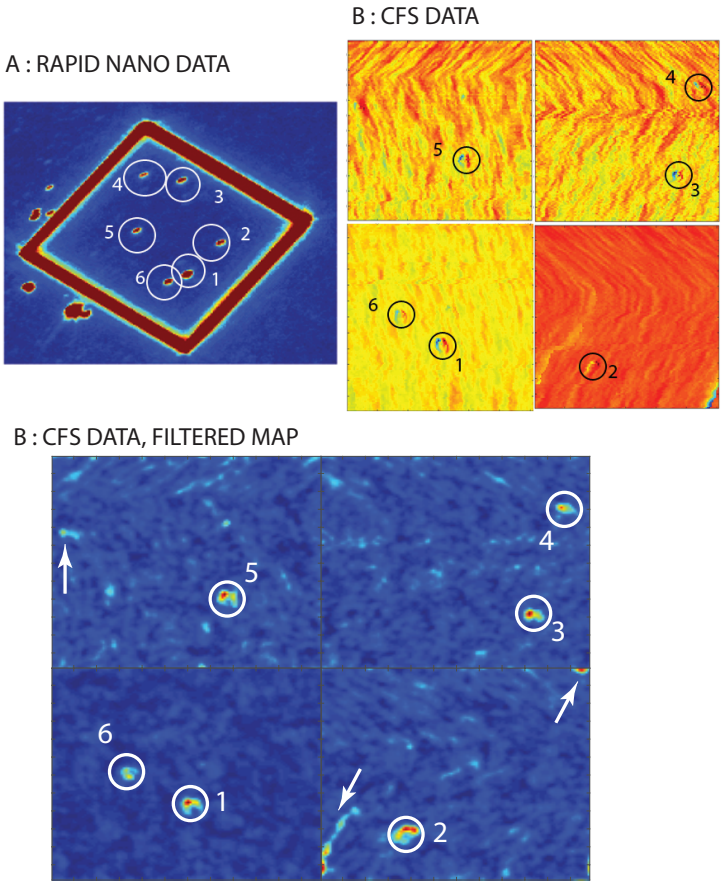

Figure 7.5: Result of the comparison experiment. The image on the left (A) was generated by the dark field scanner Rapid Nano. The image on the right side (B) is the same area scanned by the experimental bright field scanner. The power for the data in (B) was 60 μW. In (C), we have performed a Gaussian noise removing filtering on the raw experimental data from the CFS particle detector (as shown in (B)) with the noises that could not be removed, shown by arrows.

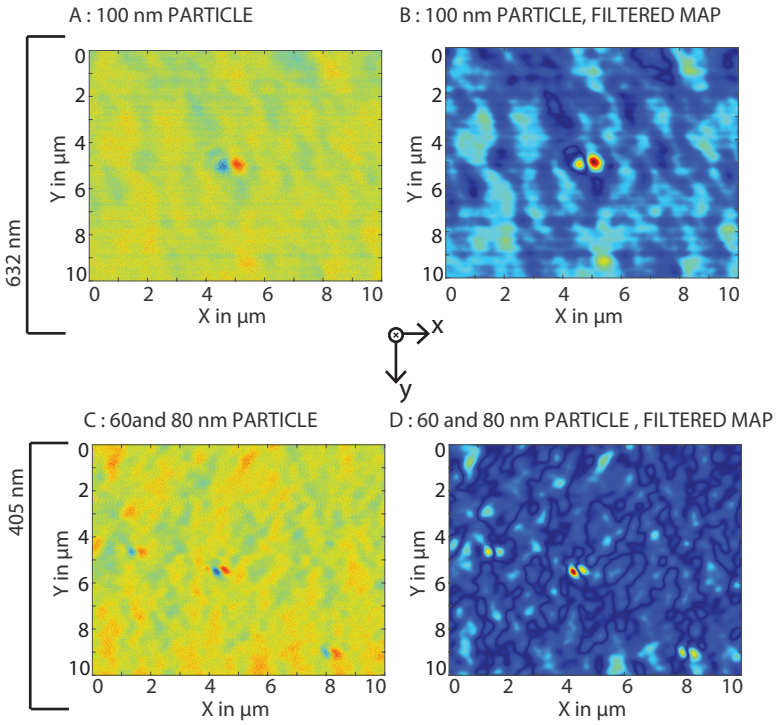

Figure 7.6: Result of the $\lambda/6$ particle detection experiment. The far field LR-maps on the top row, unfiltered (A) and filtered (B) data, were obtained with 632 nm illumination for 100 nm particles. The lower column also shows the same map, unfiltered (C) and filtered (D) data, for the sample containing 60 and 80 nm particles, scanned with 405 nm illumination. The scanned area is 10×10 μm^2.

so only an area of 72×72 sq. μm could be scanned. Fortunately, this area contained all the scatterers. This area was further divided into four adjacent squares of 36×36 sq. μm each to accommodate to the maximum scanning area of the X-Y stage. As can be seen from part B of Fig. 7.5, all six scatterers were detected, albeit with different SNR and slightly different average power levels in each quadrant. This is because of improper synchronization of the X-Y stage with the detection system and some interfacing problem between the detector and the computer. This issue, and most of the noise contribution from the data can be eliminated in the same way as was done for Fig. 5.3 in chapter 5 by using a Gaussian low-pass filter. The filtered map is shown in part C of Fig. 7.5, which clearly shows the particles, and also shows some part of noises which could not be removed (shown by arrows). The noise filtered maps from the CFS system has a SNR of about 8.

7.4. Below 100 nm particle detection

In chapter 1.4, we mentioned that the project *Clean4Yield* set the required smallest particle detection sensitivity to 100 nm. After this goal was achieved, it may

be intuitive to check the possible sensitivity limit that can be reached with the CFS particle detection system in its present status. The answer to this question is not straightforward, as the final detection sensitivity depends mainly on the noise, which is situation specific. Noise is generally much smaller in a confined laboratory environment because of its better temperature and vibration control compared to production environment such as a roll to roll line. In addition to that, the inability to use certain precision components which cannot be used under production environment, such as piezo-electric scanner which has to be replaced by the air bearings, will increase the noise components to degrade the performance of the system. However, this also implies that a successful detection of 100 nm particle under production environment may indicate that a possible sensitivity even lower than 100 nm can be reached under stable laboratory environment.

With this motivation, the CFS particle detection system was put to test to detect $\lambda/6$ particles, i.e., 100 nm particles with 632 nm illumination ($\lambda/6.32$) and 60 nm particles with 405 nm illumination ($\lambda/6.75$). For the second case, a new sample was made with 60 nm and 80 nm PSL particles on a silicon substrate. The results are shown in Fig. 7.6. In (A) and (B) of the figure, one can see the far field LR data maps for unfiltered and filtered data, respectively. Exactly the same type of filtering as done for Fig. 5.3 and Fig. 7.5 has also been used here. For the top row, the illumination wavelength is 632 nm and the particle size is 100 nm. The particle is clearly detected. More interestingly, in the bottom row, a sample containing 60 nm and 80 nm particles were scanned. Both the unfiltered (C) and the filtered LR maps (D) show multiple particle detection. In the filtered one, we can spot clearly three detected particles, which possibly consists of a larger (80 nm) and two smaller (60 nm) particles.

Although the lowest possible detection limit of the CFS particle scanner has not yet been clearly determined by us, it is possible to anticipate from these maps that it might be in the range of 50-60 nm on silicon surface. To be noted, these maps are still obtained from the basic CFS version, and after application of the different techniques we have discussed in last three chapters, we might be able to detect particles smaller than that limit.

7.5. Discussion

In this chapter, we presented the performance of CFS prototype for particle detection down to 100 nm in a roll-to-roll line production environment. It has a different way of delivering power from the source to the scatterer-substrate system than conventional dark field scanner, and can operate using sources with much less power output. The technique is suitable for utilization on most substrates including those which can be damaged under high power illumination. Moreover, it has been shown that the technique is simple, robust and fast enough to work in an industrial environment without slowing down the speed of production. The approximate size distribution of the scatterer is also possible to be retrieved with simple algorithms. We also present a comparison experiment of a CFS scanner with a standard dark field scanner and have shown that CFS was able to detect all the scatterers as was detected by the dark field scanner. Finally we presented the detection capability of

CFS particle detector to successfully detect sub 100 nm particles.

For this chapter we have used the most simple version of CFS, and except the 'detection by asymmetry' principle, we did not use any procedures to enhance the SNR as we have discussed in last three chapters. Nonetheless, we would like to point out that the test of CFS prototype met the specifications set by the Clean4Yield project, i.e., to detect particles down to 100 nm. Moreover, all these techniques can be implemented independently of each other, as well as combined, to achieve an even higher sensitivity of detection. It is important to note that all these aforementioned techniques like inner pupil blocking (Chapter 4), radially polarized light (Chapter 5) or layered substrate (Chapter 6) are implemented by physical elements and require no additional data processing, which implies incorporating all of them should not lead to any reduction in the speed of particle detection.

7.6. Acknowledgments

The author greatly acknowledges Xukang Wei, Lei Wei, Roland Horsten and Thim Zuidwijk for the work presented in this chapter.

References

[1] S. Roy, M. Bouwens, L. Wei, S. F. Pereira, H. P. Urbach, and P. van der Walle, *High speed low power optical detection of sub-wavelength scatterer,* Review of Scientific Instruments **86** (2015).

[2] J. van der Donck, R. Snel, J. Stortelder, A. Abutan, S. Oostrom, S. van Reek, B. van der Zwan, and P. van der Walle, *Particle detection on flat surfaces,* Proc. SPIE **7969**, 79691S (2011).

[3] P. van der Walle, P. Kumar, D. Ityaksov, R. Versulis, D. J. Maas, O. Kievit, J. Janssen, and J. C. J. van der Donck, *Nanoparticle detection limits of tno's rapid nano: modeling and experimental results,* Proc. SPIE **8522**, 85222Q (2012).

[4] R. R. Søndergaard, M. Hösel, and F. C. Krebs, *Roll-to-roll fabrication of large area functional organic materials,* Journal of Polymer Science Part B: Polymer Physics **51**, 16 (2013).

[5] F. Krebs, T. Tromholt, and M. Jorgensen, *Upscaling of polymer solar cell fabrication using full roll-to-roll processing,* Nanoscale **2**, 873 (2010).

[6] P. van der Walle, S. Hannemann, D. van Eijk, W. Mulckhuyse, and J. C. J. van der Donck, *Implementation of background scattering variance reduction on the Rapid Nano particle scanner,* Proc. SPIE **9050**, 905033 (2014).

8

Outlook and Conclusion

We started the research related to optical scatterometry back in 2011, with the motivation to improve the existing CD metrology principle with a better alternative. Then it was proposed to investigate performance of CFS for isolated objects, with the final objective of a fast and low-power particle detector on a flat substrate. After four years of research, CFS has been able to achieve most of its goals. In this thesis, we have covered only the theoretical analysis for CD metrology CFS as the experimental realization of it was beyond the scope, but the interested readers are encouraged again to read the article regarding its experimental implementation in Ref. [1, 2]. The other role of CFS as a particle detector was more studied with experimental verifications, with the chapter 7 outlining the implementation of the prototype particle detector. In this chapter we present the outlooks - some ideas that could not be addressed completely at the time of drafting this thesis.

8.1. Outlook 1 : Experimental implementation of ICFS - calculating the far-field scattering matrix

In chapter 3 we introduced the concept of Interferometric Coherent Fourier Scatterometry. We recall that it was introduced as an improvement over standard CFS, where only the phase information between two overlapping orders was implicitly encoded in the far-field intensity pattern. In ICFS, we have used the concept of phase-shifting-interferometry with scatterometry by assuming coherent superposition of a separate reference wave with the scattered wave. There were mainly two advantages. Firstly, ICFS was more sensitive than CFS. Secondly, it was possible to utilize the benefits of coherence theoretically to any value of the pitch, thereby removing the constraint of large gratings that were necessary for CFS. These benefits came at the price of increase in the amount of data that are needed to be processed. However, so far all the analysis about ICFS has been done with numerical simulations and physical reasoning. It is necessary to verify all the concepts developed in chapter 3 with experiments. These experimental results has been submitted very recently [3].

A possible configuration for experimental realization of this concept is shown in Fig. 8.1, by adding an interferometric arm to the original CFS configuration as was introduced in Fig. 1.1. This is also the procedure that has been used in our recent submission [3]. Here the beamsplitter BS2 devides the reference beam from the incident beam and mirror M1 directs it to a retro-reflector on a moving piezo-stage. The outgoing and phase shifted reference beam is superposed with the scattered beam by beamsplitter BS3. The grating scanning together with the reference phase-shifting will generate the ICFS superframe for a fixed polarization combination of P1-P2. The process is repeated for all possible P1-P2 combinations.

The apertures A1 and A2 can be adjusted to select any part of the pupil in the incident wave or the scattered wave, converting it to a sectioned ICFS. A general version of the aperture can be a Spatial Light Modulator (similar to Fig. 5.2), however, for sections with simple geometries as we have used in section 3.4, a slit can be used.[1] The final results in the general case will depend on whether the aperture

[1]However, the diffraction from the edge of the aperture might be an issue.

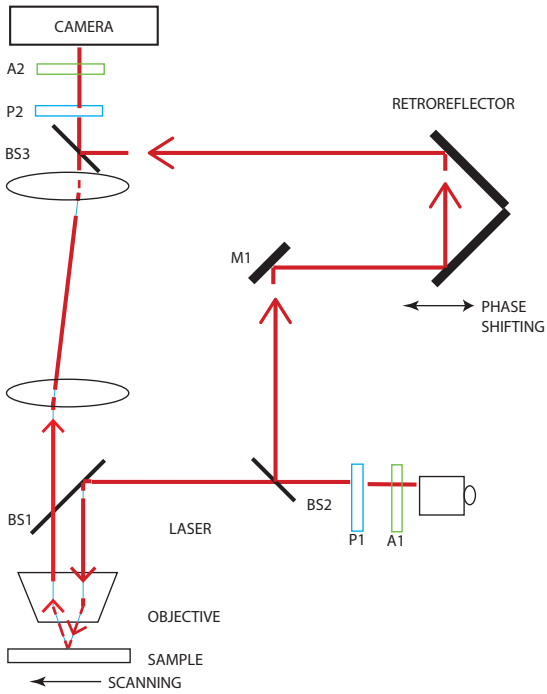

Figure 8.1: A Possible ICFS configuration. The incident-outgoing polarization combination is chosen by the polarizer pair P1-P2. In general, the polarization of the incident wavefront and the reference wavefront may be different. An example is a circularly polarized incident wave and a reference wave which is linearly polarized in two orthogonal direction, x and y, so that one does not need a polarizer in the outgoing beam. However, the above scheme is more robust to the alignment errors between different polarizers.

is placed in the incident beam or in outgoing beam, except for the special case of planar section, which is independent of the aperture location.

8.2. Outlook 2 : Optimization of incident field - A recipe with Lagrange Multiplier method

In chapter 5 we have used radially polarized incident field for enhancing the interaction in the far-field between the scattered and reflected outgoing waves. This was mostly done keeping in mind that the polarization direction for each of them is parallel in the far-field in every point of the pupil when the center of the particle and the z-axis containing the central axis of the spot coincides. We also commented that the amplitude distribution of this incident field can be further optimized using the principle of Lagrange Multipliers [4]. Here, we briefly outline the procedure to do so.

We can start from Eq. 5.6, which gives the far-field already optimized based on our previous argument. Following the Lagrange Multiplier method, one way to formulate the optimization problem is as follows :

To find the incident field distribution that maximizes the sensitivity to the displacement in the x-direction of the nano-particle for a fixed power flow, or,

$$\begin{aligned} &\text{maximize } X = \int \frac{\partial}{\partial(\Delta x)} \boldsymbol{A}^o.(\boldsymbol{A}^o)^* dk_x dk_y \\ &\text{subject to } Y = \int \boldsymbol{A}^i.(\boldsymbol{A}^i)^* \frac{k_z}{k} dk_x dk_y = 1 \text{ (i.e. the incident power is normalized.)} \end{aligned} \tag{8.1}$$

where $\boldsymbol{A}^o$ ($\boldsymbol{A}^i$) is the total outgoing (incident) wave complex amplitude.

The problem is further simplified since we are interested in radially polarized incident field in here, and so, X can be simplified by considering only the p component.

$$\begin{aligned} X &= \int \frac{\partial}{\partial(\Delta x)} A_p^o.(A_p^o)^* dk_x dk_y \\ Y &= \int A_p^i.(A_p^i)^* \frac{k_z}{k} dk_x dk_y \end{aligned} \tag{8.2}$$

To reach an approximate solution, we can make some more simplifying assumptions. It is known that integral of a function is slowly varying than the function itself, implying that a variation of the scattered part of $\boldsymbol{A}_p^o$ w.r.t A^i in Eq. 5.6 (contributed by $\boldsymbol{E}_f$ through the integration, Eq. 5.4) will be smaller than the same variation of the specularly reflected part of $\boldsymbol{A}_p^o$. Under this approximation, we can arrive at the

following form Eq. 5.6 and Eq. 8.1

$$X(A_p^i + \delta A_p^i) - X(A_p^i) = \delta X$$
$$= \frac{\partial X}{\partial A_p^i}\delta A_p^i \approx \int 2ik_x[(1 + r_p)\delta A_p^i \gamma^*(-k_x^2 - k_y^2)(E_f)^* + \text{c.c}]dk_x dk_y \tag{8.3}$$

where $\gamma = \frac{\alpha}{2j\epsilon_0}\frac{k/k_z}{\sqrt{k_x^2+k_y^2}}$, and α is complex polarizability, which is the same quantity as in chapter 5. The variation of constraint Y with the incident field is

$$Y(A_p^i + \delta A_p^i) - Y(A_p^i) = \delta Y = \frac{\partial Y}{\partial A_p^i}\delta A_p^i = \int 2\frac{k_z}{k}[(A_p^i)^* \delta A_p^i + c.c]dk_x dk_y. \tag{8.4}$$

Lagrange multiplier method is applied by multiplying Eq. 8.4 by Λ_L and subtracting it from Eq. 8.3. This must be zero for an optimum (local) solution.

$$\delta X - \Lambda_L \delta Y = 0 \tag{8.5}$$

For that to be true, the integrand must be zero, which implies

$$ik_x r_p(\gamma)^*(-k_x^2 - k_y^2)(E_{fz})^* = \Lambda_L \frac{k_z}{k}(A_p^i)^* \tag{8.6}$$

From 8.6 and 8.1 we can find the optimum field amplitude distribution A_p^i for particle detection with a radially polarized incident field,

$$A_p^i = \frac{i(r_p)^* \gamma k k_x (k_x^2 + k_y^2)}{k_z(\Lambda)^*} E_f = \frac{(1 + r_p)^* \alpha k^2 k_x \sqrt{k_x^2 + k_y^2}}{k_z^2(\Lambda)^*} E_f$$
$$\text{where } \Lambda_L = \sqrt{\int \frac{\left|(1 + r_p)\right|^2 |\gamma|^2 k k_x^2 (k_x^2 + k_y^2)}{k_z} \left|E_f\right|^2 dk_x dk_y}$$
$$= \frac{|\alpha|}{2\epsilon_0}\sqrt{\int \frac{\left|(1 + r_p)\right|^2 k k_x^2 (k_x^2 + k_y^2)}{k_z} \left|E_f\right|^2 dk_x dk_y} \tag{8.7}$$

The interesting observation here is the fact that the E_f, being independent of k_x and k_y, is eliminated from final expression of A_p^i, which reduces the numerical complexity of the problem.

This formula can be further corrected. Firstly, we can consider the phase difference (see Fig. 5.1) between the directly scattered field (A_p^{dip}) and the scattered field reflected from the substrate ($A_p^{dip,r}$). Secondly, we can take into account the first order terms of variation of E_f with Δx,

$$\boldsymbol{E}_f^{\Delta x} \approx \boldsymbol{E}_f + \frac{\partial \boldsymbol{E}_f}{\partial x}\Delta x \tag{8.8}$$

which we have so far neglected.These considerations are ways to a more rigorous analysis of this problem.

We must emphasize that this is not the only way to set up this problem, in other words, there can be many other choices of X, which will determine the problem. In the author's experience, it is the most important consideration to choose the function to be optimized (X) properly, after which the determination of optimized parameters can be calculated following a standard recipe as was outlined here.

8.3. Outlook 3 : Large area particle detection - CFS with multiple scanning heads

At the time of writing this thesis, the prototype particle detection system is able to scan only a single line on the substrate in a roll-to-roll line. It is still valuable information about the contamination on the substrate since one is generally interested in the statistical distribution of the contaminations in the substrate for which scanning the whole of the web is not necessary. On the other hand, it is also necessary to have that same information from few other locations of the sample to have a good statistical estimation. This requires an up-gradation of the prototype by using multiple scanning heads to work in parallel and scan a wider area at once.

A possible way to extend the present CFS particle detector to achieve this is shown in Fig. 8.2. Multiple probing beam has been derived from a single laser source using a diffractive optical element (transmission grating) and a collector lens with large NA. The separation between two successive scanning heads does not have to be very close since scanning the whole width of the web is rarely needed, however, there should be sufficient number of them to allow required sampling to develop a reliable statistical model of contamination distribution. It is technically challenging to produce an array of lenses with large NA in small space such as shown here, however, recently many emerging techniques for making such lenslet array has been reported [5–7], which may be consulted for choosing a suitable fabrication procedure.

8.4. Conclusion : Final Comments

Our aim in this thesis was to show that Coherent Fourier Scatterometry can be a powerful alternative to presently available techniques that perform CD metrology and particle detection on flat substrate. To our knowledge, no present system can do both functions at once, while CFS, with small modifications, can be used in both cases. Practical benefits of CFS include robust epi-illumination configuration, simple optical design and small dimensions making it more integrable (the CFS prototype installed in production line is of dimension 40cm X 20cm X 20cm), but, the main advantages are its high sensitivity (for CD metrology) and low power-high speed operation (for particle detection).

While investigating the sensitivities of a CFS with respect to IFS, the effect of scanning in the far-field due to coherence was understood more clearly. We also showed that it is possible to extend the applicability of CFS by removing its con-

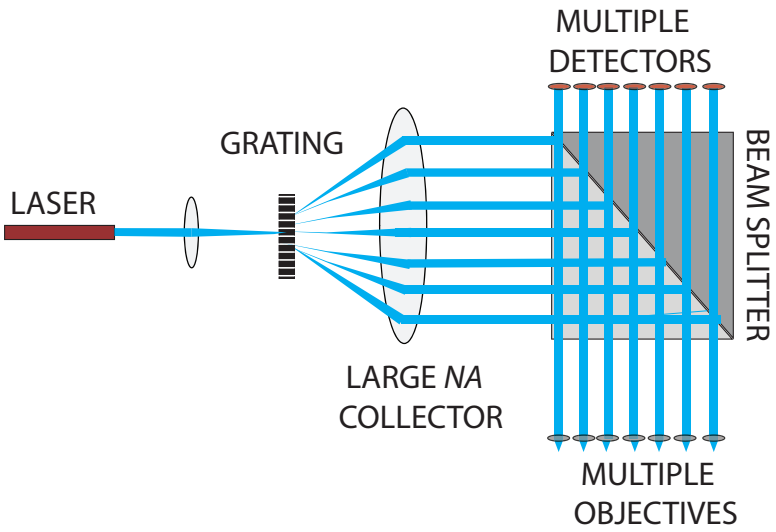

Figure 8.2: A possible configuration for CFS particle scanner with multiple heads. The generation of multiple beams is done by the transmission grating. The drawing is simplified for the sake of clarity, since to implement this properly one has to make sure that different paths do not overlap.

straint on the requirement of large pitch by merging it with interferometry, which resulted in ICFS. For the particle detection, we had to modify the then existing CFS system in several areas. The differential detection systems made CFS more sensitive and fast, while the sensitivity was further augmented by using radially polarized incident field. Another way to increase the sensitivity was also shown to be possible by modifying the substrate - the enhancement layer approach. The final implementation of the prototype led to a successful particle detection and size determination in the production environment, together with successful detection of sub 100 nm particles.

We believe that sharing the knowledge and experience that we gained through this work will be of interest for research community working in CD metrology or particle detection. We also believe that some of the concepts explained in this thesis can be of benefit to a broader group of the scientific community and can be applied in different technologies other than the ones mentioned before. Differential detection to determine the asymmetry in far-field is an useful procedure to eliminate noise and increase SNR a system in general, and scatterometry is one of the applications of it. The enhancing layer of chapter 6 can be used to increase resolution of photolithography techniques by enhancing certain evanescent wave band. Radially polarized light can be applied to detect orientation of molecules with permanent dipole moment, since only dipoles oriented along longitudinal axis (z-axis) with emit back radially polarized light when they are illuminated by focused radially polarized light, and as a result, those dipoles will produce maximum contrast when scanned.

To conclude, we sincerely hope that there will be further developments and

research on the ideas discussed in this thesis to make it more suitable for practical implementation, ultimately producing a positive impact in our society.

References

[1] N. Kumar, P. Petrik, G. K P Ramanandan, O. El Gawhary, S. Roy, S. F. Pereira, Wim M. J. Coene, and H. P. Urbach, *Reconstruction of sub-wavelength features and nano-positioning of gratings using coherent fourier scatterometry,* Opt. Express **22**, 24678 (2014).

[2] V. Paz, S. Peterhansel, K. Frenner, and W. Osten, *Solving the inverse grating problem by white light interference fourier scatterometry,* Light Sci Appl **1** (2012).

[3] N. Kumar, L. Cisotto, S. Roy, G. Ramanandan, S. F. Pereira, and H. P. Urbach, *Determination of the full scattering matrix using coherent fourier scatterometry,* (2016), submitted.

[4] H. P. Urbach and S. F. Pereira, *Field in focus with a maximum longitudinal electric component,* Phys. Rev. Lett. **100**, 123904 (2008).

[5] A. Tripathi, T. V. Chokshi, and N. Chronis, *A high numerical aperture, polymer-based, planar microlens array,* Opt. Express **17**, 19908 (2009).

[6] H. Jung and K. Jeong, *Monolithic polymer microlens arrays with high numerical aperture and high packing density,* ACS Applied Materials & Interfaces **7**, 2160 (2015).

[7] D. Wu, S. Wu, L. Niu, Q. Chen, R. Wang, J. Song, H. Fang, and H. Sun, *High numerical aperture microlens arrays of close packing,* Applied Physics Letters **97**, 031109 (2010).

Acknowledgements

Everybody helped ! Thanks to all !

A special acknowledgement goes to the CFS team in Optics Group. My sincere thanks to Dr. S.F. Pereira, the heart of the team, for her ideas, encouragement and above all, continuous support. Thanks to Prof. H.P. Urbach, for his inputs, reviews and guidance. Thanks to both of them for making it enjoyable, with both of your open door attitude and friendly and humorous company. Taking about humor, lets thank Alberto, Nitish and Roland, not for their non-existent sense of humor(!), but their contribution to this work. Equally important contribution to this project was made by Thim, Rob, Lei, Xukang, Kate, Quincy and Maryse. Thanks for your much needed help. I also thank Dr. A.J.H Wachters for his FEM software, Cyclops, which has been used extensively in this thesis. Thanks to Peter Somers for taking the trouble to translate the summary in Dutch and to Sander for doing the same with the propositions. Also, thanks to all the committee members for reviewing this thesis in a short time inside their busy schedule and providing feedback for making it better.

The *Clean4Yield* consortium involved several members, a heartiest thanks to all of them. I would like to mention the important contributions from Christiaan Hollemans of TNO, Delft, Hero H. Mannetje of Holst Center, Einhoven, Valentijn von Morgen of Dupont Teijin Films and Simone Dafinger of Dr. Schenk, Munich for this work. A special acknowledgement goes to them. Thanks to Dr. Juliane Tripathi and Dr. Michiel Coenen, who were the coordinator of the project, for their strict (very rightfully so) control. Heartiest congratulations to Juliane for her baby. Also, thanks to Harmen. I wish you a speedy recovery (unless you have recovered already). It was a big consortium, so I cannot mention all of them, but I thank everybody and wish them all the best.

Coming back to the group, I would like to thank Dr. Omar El Gawhary and Yvonne van Aalst, for two completely different reasons. I would not have worked in this project without Omar's motivation. Thanks for all the intriguing ideas, lucid explanations and overall, teaching to think scientifically. Also, I would not have worked in this project without Yvonne's help. A big thanks for taking care of all the administrative things and practical issues and for letting physicists try to be physicists. Thanks to Dr. Nandini Bhattacharya for all the practical helps I got from her. It was fun to speak Bengali 10,000 km away from home. A special acknowledgement for Dr. Peter Petrik here, for the scientific insights I obtained during his short stay in Delft.

In my five years in the Optics group, all of the colleagues have become friends. Andreas, Luca, Gopakumar, Gopika, Nishant, Hamed, Adonis and Edgar : lets keep the fun level up in the group or elsewhere you work now. Thanks for all the helps and also all the lively, and most of the times, not so useful, discussions. Again,

heartiest congratulations to (even!) Gopika for being a mother. Thanks to Prof. Joseph Braat and Dr. Jeff Meisner, for making the afternoon coffee breaks, group talks and agoras a learning opportunity. I also acknowledge Dr. Florian Bociort, Dr. Aurele Adam, Prof. Paul Planken and Chris Christie for their help. I thank Daniel (Asoubar), Marco, Pascal, Alessandro, Masha, Diego and Priya - with whom I shared the offices at some point of time for their kind co-operation (Priya, I still did not get the 10 Euro I won !). Thanks to Daniel, Ying, Xi, Matthias, Boling, Anna, Yifeng, Fellipe, Wouter, Zhe, Milena and all the others. You guys are great!

From outside of the Optics group, I would like to thank Gerward, Ann, Hozana and Dr. C.W. Hagen. Thanks to Minthe (not only for helping me with the exams :)), Jiazi, Michael, Minyi, Almaz, Cong and Mitradeep. Special thanks for Siqi, for being an awesome *classmate* for six years and on. Lets travel somewhere soon, shall we?

Finally, it is my family. My parents, literally the best in the world, uncle, aunty (ya, I am Indian) and my little sister. They have constantly supported me in all the things in life. Thank you very much. Also thanks to my friends back in home and in other parts of the world who were not mentioned here. Sorry, you are more in number than the army of Costa Rica or an equivalently big country, and I don't dare to start mentioning your names. I thank all of you!

Curriculum Vitæ

Sarathi ROY

Education

2003–2009	B.Sc. & B. Tech in Physics & Optics Presidency College, Kolkata (2003–2006) University of Calcutta, Kolkata (2006–2009)
2009–2011	M.S. in Applied Physics Warsaw University of Technology, Warsaw, Poland (2009–2010) Delft University of Technology, Delft, The Netherlands (2010–2011)
2011–2012	Researcher in Applied Physics Optics Group, Delft University of Technology, Delft, The Netherlands and Philips Research, Eindhoven, The Netherlands
2012–	PhD student in coherent Fourier scatterometry Optics Group, Delft University of Technology, Delft
2015–	Design Engineer, ASML, Eindhoven, The Netherlands

Scholarships and Honors

2008	IET India Scholarship
2009	Erasmus Mundus Masters Scholarship
2011	Graduated with Honors: TU Delft
2013	Featured Article : Journal of Optics
2014	Best Poster Prize : Imaging Physics Group, Delft University of Technology
2015	Editor's Choice and Featured in Physics Article : Physical Review Letter

List of Publications

Published :

9. **S. Roy**, **M. Bouwens**, **L. Wei**, **S. F. Pereira**, **H. P. Urbach**, *High speed low power optical detection of sub-wavelength scatterer*, Review of Scientific Instruments **86**, 12 (2015).

8. **S. Roy**, **K. Ushakova**, **Q. van den Berg**, **S. F. Pereira**, **H. P. Urbach**, *Radially Polarized Light for Detection and Nanolocalization of Dielectric Particles on a Planar Substrate*, Physical Review Letters **114**, 103903 (2015).

7. **S. Roy**, **A. C. Assafrão**, **S. F. Pereira**, **H. P. Urbach**, *Coherent Fourier scatterometry for Detection of Nanometer-sized Particles on a Planar Substrate Surface*, Optics Express **22**, 11 (2014).

6. **S. Roy**, **N. Kumar**, **S. F. Pereira**, **H. P. Urbach**, *Interferometric Coherent Fourier Scatterometry: a Method for Obtaining High Sensitivity in the Optical Inverse-Grating Problem*, Journal of Optics **15**, 7 (2013).

5. **S. Roy**, **O. El Gawhary**, **N. Kumar**, **S. F. Pereira**, **H. P. Urbach**, *Scanning Effects in Coherent Fourier Scatterometry*, Journal of the European Optical Society-Rapid publications **7**, 12031 (2012).

4. **S. Roy**, **O. El Gawhary**, **N. Kumar**, **S. F. Pereira**, **H. P. Urbach**, *Lowering the Cross Correlation between Different Shape Parameters of the Inverse Grating Problem in Coherent Fourier Scatterometry*, Fringe , 43–48 (2013).

3. **N. Kumar**, **P. Petrik**, **G. Ramanandan**, **O. El Gawhary**, **S. Roy**, **S. F. Pereira**, **Wim M. J. Coene**, **H. P. Urbach**, *Reconstruction of sub-wavelength features and nano-positioning of gratings using coherent Fourier scatterometry*, Optics Express **22**, 10 (2014).

2. **N. Kumar**, **O. El Gawhary**, **S. Roy**, **S. F. Pereira**, **H. P. Urbach**, *Phase information in Coherent Fourier Scatterometry*, Proceedings of SPIE **8788**, 87881P (2013).

1. **N. Kumar**, **O. El Gawhary**, **S. Roy**, **S. F. Pereira**, **H. P. Urbach**, *Coherent Fourier scatterometry: Tool for Improved Sensitivity in Semiconductor Metrology*, Proceedings of SPIE **8324**, 83240Q (2012).

Submitted:

1. **N. Kumar**, **L. Cisotto**, **S. Roy**, **G. Ramanandan**, **S. F. Pereira**, **H. P. Urbach**, *Determination of the full scattering matrix using coherent Fourier scatterometry*

Manuscript in Preparation:

1. **S. Roy**, **O. El Gawhary**, **X. Wei**, **S. F. Pereira**, **H. P. Urbach**, *Enhancement of Evanescent Wave for Particle Detection*.